

# Three Problems Involving Compressible Flow with Large Bulk Viscosity and Non-Convex Equations of State

Fatemeh Bahmani

Dissertation submitted to the faculty of the  
Virginia Polytechnic Institute and State University  
in partial fulfillment of the requirements for the degree of

Doctor of Philosophy  
in  
Engineering Science and Mechanics

Mark Cramer, Chairman

Saad Ragab

Mark Paul

Sunny Jung

Shane Ross

July 5, 2013

Blacksburg, Virginia

Keywords: (Compressible flow, shock, boundary layer, WENO, CFD, bulk viscosity, BZT fluids)

Copyright 2013, Fatemeh Bahmani

# Three Problems Involving Compressible Flow with Large Bulk Viscosity and Non-Convex Equations of State

Fatemeh Bahmani

## Abstract

We have examined three problems involving steady flows of Navier-Stokes fluids. In each problem non-classical effects are considered. In the first two problems, we consider fluids which have bulk viscosities which are much larger than their shear viscosities. In the last problem, we examine steady supersonic flows of a Bethe-Zel'dovich-Thompson (BZT) fluid over a thin airfoil or turbine blade. BZT fluids are fluids in which the fundamental derivative of gasdynamics changes sign during an isentropic expansion or compression. In the first problem we consider the effects of large bulk viscosity on the structure of the inviscid approximation using the method of matched asymptotic expansions. When the ratio of bulk to shear viscosity is of the order of the square root of the Reynolds number we find that the bulk viscosity effects are important in the first corrections to the conventional boundary layer and outer inviscid flow. At first order the outer flow is found to be frictional, rotational, and non-isentropic for large bulk viscosity fluids. The pressure is found to have first order variations across the boundary layer and the temperature equation is seen to have two additional source terms at first order when the bulk viscosity is large. In the second problem, we consider the reflection of an oblique shock from a laminar flat plate boundary layer. The flow is taken to be two-dimensional, steady, and the gas model is taken to be a perfect gas with constant Prandtl number. The plate is taken to be adiabatic. The full Navier-Stokes equations are solved using a weighted essentially non-oscillatory (WENO) numerical scheme. We show that shock-induced separation can be suppressed once the bulk viscosity is large enough. In the third problem, we solve a quartic Burgers equation to describe the steady, two-dimensional, inviscid supersonic flow field generated by thin airfoils. The Burgers equation is solved using the WENO technique. Phenomena of interest include the partial and complete disintegration of compression

shocks, the formation of expansion shocks, and the collision of expansion and compression shocks.

This work received support from National Science Foundation Grant CBET-0625015.

# Acknowledgments

I wish to express my greatest appreciation first to my advisor Professor Mark Cramer for the continuous support and encouragement during my Ph.D. study, for his motivation, enthusiasm, and immense knowledge.

It is with deepest gratitude that I acknowledge the support and help of Professor Saad Ragab for all his helpful comments for the code development part of my research.

I would like to thank the rest of my thesis committee: Professor Sunny Jung, Professor Mark Paul and Professor Shane Ross for their insightful comments and suggestions.

I would like to thank the department of engineering science and mechanics computer system administrators for providing the computer cluster facility.

I thank my fellow labmates for the stimulating discussions, exchange of knowledge and for the good time we were working together. Also I thank the staff members and my friends in the engineering science and mechanics department and Virginia Tech for their help and support.

Last but not the least, I wish to express my gratitude to my family, my parents and my brothers for their endless love and support throughout my life.

# Contents

<b>List of Figures</b>	<b>viii</b>
<b>1 Introduction</b>	<b>1</b>
<b>2 Non-Classical Physics</b>	<b>4</b>
2.1 Introduction . . . . .	4
2.2 Bulk Viscosity for Ideal Gases . . . . .	5
2.3 Moderate Bulk Viscosity Fluids . . . . .	7
2.4 Large Bulk Viscosity Fluids . . . . .	7
2.5 BZT Fluids . . . . .	9
<b>3 Inviscid-Viscous Flows with Large Bulk Viscosity</b>	<b>11</b>
3.1 Introduction . . . . .	12
3.2 Formulation . . . . .	17
3.3 Outer Solution . . . . .	22
3.4 Inner Solution . . . . .	27

3.5	Matching . . . . .	31
3.6	Flat-Plate Boundary Layer . . . . .	33
3.7	Conclusion . . . . .	44
<b>4</b>	<b>Shock-Boundary Layer Interaction for Large Bulk Viscosity Fluids</b>	<b>46</b>
4.1	Introduction and Motivation . . . . .	46
4.2	Local Thermodynamic Equilibrium (LTE) . . . . .	49
4.3	Formulation . . . . .	50
4.3.1	Numerical Schemes . . . . .	58
4.3.2	Validations . . . . .	59
4.4	Results . . . . .	64
4.5	Summary . . . . .	68
<b>5</b>	<b>Fluids with Non-Convex Equations of State</b>	<b>69</b>
5.1	Introduction . . . . .	69
5.2	Review of Crickenberger's Theory . . . . .	72
5.3	Numerical Method . . . . .	81
5.4	Comparison to Exact Solution . . . . .	82
5.5	Numerical Results . . . . .	87
5.6	Summary . . . . .	91
<b>6</b>	<b>Conclusion</b>	<b>92</b>

<b>Appendices</b>	<b>94</b>
<b>A Navier-Stokes Equations</b>	<b>95</b>
<b>B Surface Oriented Coordinates</b>	<b>98</b>
<b>C WENO Scheme</b>	<b>103</b>
<b>Bibliography</b>	<b>108</b>

# List of Figures

2.1	Estimation of the ratio of bulk viscosity to shear viscosity as a function of temperature for some large bulk viscosity substances . . . . .	8
2.2	Comparison of the turbine cascade flow of a classical fluid and a BZT fluid. . . . .	10
3.1	Sketch of global coordinate system and body. The freestream speed is aligned with the positive $x$ -axis and has magnitude $U$ . The length scale measuring the size of the body is $L$ . . . . .	14
3.2	Scaled pressure vs. physical distance measured normal to the plate for different values of bulk viscosity to shear viscosity. . . . .	38
3.3	Scaled pressure vs. physical distance measured normal to the plate for different values of freestream Mach number for bulk viscosity to shear viscosity ratio = 500. . . . .	39
3.4	Scaled pressure vs. physical distance measured normal to the plate for heated and cooled plates for bulk to shear viscosity ratio=500. Here $\theta_w$ = wall temperature divided by the freestream temperature. . . . .	40
3.5	Variation of the bulk viscosity of methane with temperature. . . . .	41



3.6	Scaled pressure vs. physical distance measured normal to the plate for realistic and constant bulk to shear viscosity of methane. . . . .	42
4.1	Shock-boundary layer interaction. . . . .	47
4.2	Sketch of the computational domain. . . . .	51
4.3	Comparison of pressure profiles of the exact and numerical solutions for an oblique shock regular reflection. . . . .	60
4.4	Comparison of velocity profiles of the similarity and numerical solutions for flat plate boundary layer. . . . .	61
4.5	Comparison of temperature profiles of the similarity and numerical solutions for flat plate boundary layer. . . . .	62
4.6	Comparison of the results of the present scheme with previous computations. . . . .	63
4.7	Skin friction coefficients along the plate for large bulk viscosity fluids. . . . .	65
4.8	Contour of scaled pressure for classical fluids, $\mu_b/\mu = 0.7$ . . . . .	66
4.9	Contour of scaled pressure for large bulk viscosity fluids, $\mu_b/\mu = 800$ . . . . .	67
5.1	Example of flow patterns with a BZT fluid. . . . .	70
5.2	Variation of the scaled fundamental derivative vs. scaled density along the critical isotherm. The quantity $\rho_c$ denotes the density at the critical point for each fluid. . . . .	71
5.3	Sketch of the variation of $\tilde{\Gamma}$ on an isentrope. The solid line is the exact variation and the dashed line is the approximation (5.4). . . . .	73
5.4	Sketch of the flow and notation. . . . .	74

5.5	Sketch of $F$ vs $u$ curve and Raleigh lines. Proposed discontinuities 3-5 are inadmissible because the Rayleigh line 3-5 does not lie entirely above or below the $F$ curve. Arrows denote the direction of jumps for the admissible shocks 4-3, 4-5, 1-2.	80
5.6	$F$ vs $u$ curve for $\Gamma_\infty > 0$ and $\Lambda_\infty < 0$ .	83
5.7	Numerical and exact solutions of flow over wedge at a freestream Mach number of 2 and $\Gamma_\infty > 0$ and $\Lambda_\infty < 0$ . The quantity $\alpha$ is the (negative) scaled wedge angle. The horizontal axis is distance in the flow direction in a frame moving with the Mach lines of the undisturbed flow. The vertical axis is a scaled measure of the flow deflection angle as defined in (5.28).	84
5.8	The $F$ vs $u$ curve for $\Gamma_\infty > 0$ and $\Lambda_\infty > 0$ .	85
5.9	Numerical and exact solutions of flow over wedge at a freestream Mach number of 2 and $\Gamma_\infty > 0$ and $\Lambda_\infty > 0$ . The quantity $\alpha$ is the (negative) scaled wedge angle. The horizontal axis is distance in the flow direction in a frame moving with the Mach lines of the undisturbed flow. The vertical axis is a scaled measure of the flow deflection angle as defined in (5.28).	86
5.10	Contour plot for $A = -1.5$ , $B = 0.8$ , $\alpha = 4$ , and a parabolic arc airfoil. Each contour line represents a $\Delta u = 0.15$ from $u = -4$ to $u = 4$ . The airfoil is positioned between $X = 0$ and $X = L$ .	88
5.11	Plot of $u$ vs $\chi$ at $\hat{y} = 0.05$ for the same case as illustrated in Figure 5.10.	89
5.12	Plot of $u$ vs $\chi$ at values of $\hat{y} = 0.05, 0.1, 0.2,$ and $0.4$ . The wing shape and values of $A, B, \alpha$ are identical to those of Figures 5.10-5.11.	90

# Chapter 1

## Introduction

Most of our intuition and rules of thumb in gasdynamics are based on the theory of low pressure air and steam in spite of the fact that many modern industrial processes and power systems involve high pressure fluids which may or may not have molecular structures and dynamics similar to that of air and water. The best way to describe the present dissertation is that we are attempting to extend our knowledge of compressible flows to a wider range of substances than what are commonly discussed. In this thesis we will also consider the dynamics of fluids over a wider range of pressures and temperatures than those of the perfect gas theory. We consider only single-phase, non-reacting fluids governed by the Navier-Stokes equations. Thus, we are extending our knowledge of classical fluids, although we will see the behavior is far from being classical. The work found in Chapters 3 and 4 describes the dynamics of fluids having large bulk viscosity  $\mu_b$  defined by

$$\mu_b = \mu_b(p, T) = \lambda + 2/3\mu, \quad (1.1)$$

where  $p$ ,  $T$ ,  $\lambda = \lambda(p, T)$ ,  $\mu = \mu(p, T)$  are the pressure, absolute temperature, second viscosity, and shear viscosity of the fluid. A more complete discussion of bulk viscosity is found in Chapter 2. We also describe the dynamics of fluids of the Bethe-Zel'dovich-Thompson (BZT) type. The

latter fluids are typically heavy fluorocarbons, hydrocarbons, and methyl-siloxanes for which the fundamental derivative of gasdynamics ( $\Gamma$ ) becomes negative over a finite range of temperatures and pressures. Here, the dimensional form of the fundamental derivative is defined as

$$\Gamma = \Gamma(\rho, s) = \frac{a}{\rho} + \left. \frac{\partial a}{\partial \rho} \right|_s \quad (1.2)$$

where  $\rho$ ,  $s$ , and  $a = a(\rho, s)$  denote the fluid density, entropy, and thermodynamic sound speed. Because the pressures at which the value of the fundamental derivative becomes negative are large, the  $\Gamma < 0$  work considers the dynamics of high-pressure fluids rather than the ideal gas theory found in many discussions of compressible flows. A more complete discussion of BZT fluids is found in Chapter 5.

The motivation for this work is of obvious scientific interest. By considering the full range of values possible for (1.1)-(1.2), we seek to extend the knowledge and intuition base of classical, i.e., Navier-Stokes, fluids. Further motivation is provided by the societal, economic, and technological interest in increasing the efficiency of traditional power systems and the interest in developing non-fossil fuel energy sources. The latter include power systems based on geothermal, solar, waste heat, bio-mass, and nuclear energy sources. Such energy sources typically require non-aqueous working fluids and, as a result, will require additional research in order to understand any non-classical or non-intuitive dynamics. One of the results of the present dissertation is the demonstration that the natural gasdynamics of many fluids can be aerodynamically advantageous. We hope that the present research can stimulate further studies and, ultimately, a more secure and affordable energy future. The non-negligible bulk viscosity fluids and BZT fluids have some industrial applications. Among those is water vapor which is used as the working fluid in Rankine cycle power systems, and fluids which are used as the working fluid in non-aqueous power systems. The latter systems are used in small power plants to generate electricity from low and medium temperature, low grade and waste heat sources. The large bulk viscosity fluids  $N_2O$ , and  $CO_2$  have been proposed

as the working fluid in nuclear power plants. Examples are studies of [1], [2], [3], [4], [5], [6], [7] and [8] for organic Rankine cycles and also studies of [9], [10], [11], [12], [13] and [14], [15] on the use of  $N_2O$  and  $CO_2$  in nuclear power systems. Another application is the heavy gas wind tunnel similarity studies where more complex molecules like  $SF_6$  are used to get a better match for the Reynolds and Mach numbers between test and flight conditions; e.g. [16], [17], [18]. In pharmaceutical industry a solute is dissolved into a solvent e.g.  $CO_2$  as a non-toxic and non-flammable solvent in supercritical conditions, then expanded through a nozzle. The solute will precipitate into a uniform sized powder. Often pharmaceutical drugs are very sensitive to process conditions. Use of milling and grinding for particle size reduction might ruin the quality of substances. Rapid expansion of supercritical solutions (RESS) has been proved to be a more suitable process for this purpose when use of a low-critical temperature solvent allows the process at lower temperatures while maintaining the efficiency of desirably fine particle formation. See studies by [19], [20] and [21].

In Chapter 2 the large bulk viscosity fluids and BZT fluids are introduced. Estimation of bulk viscosity is provided and bulk viscosity of sample substances is given. In chapter 3 we have examined the effects of large bulk viscosity on 3-D steady flows over bodies at large Reynolds numbers. The method of matched asymptotic expansions was used to develop a first-order theory for both the outer and inner flows. In Chapter 4 we have examined the effect of large bulk viscosity on the classical problem of shock-boundary layer interaction. In this chapter we show the increases in the shock thickness due to increasing bulk viscosity can lead to a suppression of separation in high speed flows. In Chapter 5 the Burgers equation describing right running simple waves in steady two-dimensional inviscid flows of a BZT fluid over thin airfoils has been solved. The code appears to be capable of capturing shock waves and distinguishing them from smooth fans.

# Chapter 2

## Non-Classical Physics

### 2.1 Introduction

The bulk viscosity and dense gas effects have often been ignored and the Navier-Stokes equations are solved for zero bulk viscosity fluids and dilute gases. The main purpose of this research is to extend our knowledge of the Navier-Stokes equations to include a full range of fluids and also a wider range of pressures and temperatures. The focus of this thesis is to study the dynamics of large bulk viscosity fluids and the behavior of fluids in high pressure regimes.

Bulk viscosity is related to the time or number of collisions, required for the molecules to achieve internal, vibrational and rotational equilibrium. The values of  $\mu_b$ ,  $\lambda$  and  $\mu$  are dependent on the local thermodynamic state and must be obtained by measurements or molecular theory. For the Navier-Stokes fluids, the relation between the viscous part of the stress tensor and rate of strain tensor is given by a linear relation

$$\tau_{ij} = \beta_{ijrs} D_{rs} \quad (2.1)$$

where  $\tau_{ij}$  is the viscous stress tensor,  $D_{rs}$  is the rate of deformation or stretching tensor and  $\beta_{ijrs}$

is the (constant) viscosity coefficient. The symmetric property of the viscous stress tensor and the deformation tensor and the isotropic property of fluids reduce the number of viscosity coefficients from 81 down to 2 coefficients which are the second and shear viscosity coefficients. So the relation of viscous stress tensor and deformation tensor could be written as

$$\tau_{ij} = 2\mu(D_{ij} - \frac{1}{3}\delta_{ij}D_{rr}) + \mu_b\delta_{ij}D_{rr}. \quad (2.2)$$

which holds for Newtonian fluids.

For inviscid flows  $\mu_b, \mu, k \equiv 0$ , for incompressible fluids, the rate of volume dilatation is zero  $D_{rr} = \nabla \cdot \mathbf{v} = 0$  and for quasi-parallel flows,  $\mu_b \nabla \cdot \mathbf{v}$  is of higher order and therefore are not considered here. Effect of bulk viscosity are generally important in cases where full Navier-Stokes equations are required, e.g., viscous, compressible flows with complex geometries. Work of Chapter 3 will show how importance of bulk viscosity increases in boundary layer theory. Stokes' Hypothesis states that the bulk viscosity is zero even for compressible flows, [22]. However, this is expected to be true only for low pressure monatomic gases. Diatomic and polyatomic gases, even at low pressure, are expected to have non-zero values of the bulk viscosity, [23].

## 2.2 Bulk Viscosity for Ideal Gases

Although there are many studies and data available for the description of transport properties like shear viscosity and specific heat, there is not much data for the bulk viscosity. A few theoretical and experimental studies have been done. These studies are limited to some specific molecules and temperature ranges. The data available in the literature of bulk viscosity of ideal gases tells us that the bulk viscosity ratio  $\mu_b/\mu$  has a variation with temperature and usually has a local maximum. Tisza has provided a simple formulation for the estimation of bulk viscosity based on rotational

and vibrational relaxation times for ideal or low pressure gases

$$\mu_b = (\gamma - 1)^2 \sum_{i=1}^N \frac{c_{vi}}{R} p \tau_i \quad (2.3)$$

$$c_{vi} = c_{vi}(T) \equiv \frac{de_i}{dT}$$

In (2.3),  $\tau_i$  refers to the relaxation time for each of the  $N^{th}$  internal energy modes.  $c_{vi}$  is the constant volume specific heat,  $\mu_b = \mu_b(T)$  and  $p\tau_i = p\tau_i(T)$ . The ideal gas law is used here for the equation of state

$$p = \rho RT. \quad (2.4)$$

The combination of Tisza's formula with available rotational and vibrational relaxation times will give an estimation of bulk viscosity. In order for each internal mode to have contribution to bulk viscosity, the energy of collision must be higher than the lowest characteristic temperature associated with that mode. This effect will be accounted for by the specific heats which become nearly zero when the temperature is lower than the characteristic temperature of the mode. In the simplest model, the vibrational and rotational parts of the bulk viscosity are summed up to obtain a value for bulk viscosity

$$\mu_b = \mu_b|_r + \mu_b|_v$$

$$\mu_b|_r = (\gamma - 1)^2 \frac{f_r}{2} p \tau_r$$

$$\mu_b|_v = (\gamma - 1)^2 \frac{c_{v|v}}{R} p \tau_v \quad (2.5)$$

In the above equations  $\tau_r$  and  $\tau_v$  are the rotational and vibrational relaxation times respectively. The quantities  $\mu_b|_r$  and  $\mu_b|_v$  are the rotational and vibrational parts of bulk viscosity. In the second of (2.5),  $f_r$  which denotes the rotational degrees of freedom which has a value of 2 for linear molecules and 3 for other molecules. At sufficiently low temperatures, vibrational modes are



not active and rotational relaxation times make the only contribution to the bulk viscosity. Since rotational relaxation times are too small, only the vibrational part of the bulk viscosity is considered at high temperatures. The experimental studies to obtain a value for bulk viscosity is either direct method by acoustic measurement and shock thickness or indirect from measured relaxation times. Acoustic absorption is a practical tool to obtain values for bulk viscosity. This method is one of the few methods which provide estimation for the value of bulk viscosity. Further discussions of the bulk viscosity of ideal gases are found in [24], [25] and [23].

## 2.3 Moderate Bulk Viscosity Fluids

The vibrational and rotational energies of monatomic gases, e.g., argon, helium, xenon, are normally regarded as negligible. As a result, the value of  $c_{vi}$  in (2.3) is taken to be zero and the bulk viscosity is therefore zero for these gases. Air,  $N_2$ ,  $O_2$  and CO are found to have bulk viscosities of the same order of their shear viscosities at room temperature and pressure,  $\mu_b = O(\mu)$ , [23]. Water vapor is recently found to have  $\frac{\mu_b}{\mu} \leq 8$ . Dimethylpropane, n-pentane, iso-pentane, n-butane, iso-butane are also among the moderate bulk viscosity fluids.

## 2.4 Large Bulk Viscosity Fluids

For large bulk viscosity fluids, we first discuss the bulk viscosity of  $H_2$  which has a high vibrational characteristic temperature so that only the rotational mode is active at room temperature. However, the  $H_2$  molecule requires about 200 or more collisions to establish equilibrium. As a result  $H_2$  is unusual in that it has  $\mu_b = O(30 - 40\mu)$ . For methane ( $CH_4$ ), acetylene ( $C_2H_2$ ), ethylene ( $C_2H_4$ ) and cyclopropane (c- $C_3H_8$ ), the vibrational characteristic temperature is low enough that both the rotational and vibrational components of bulk viscosity are present. As shown by [23], the bulk

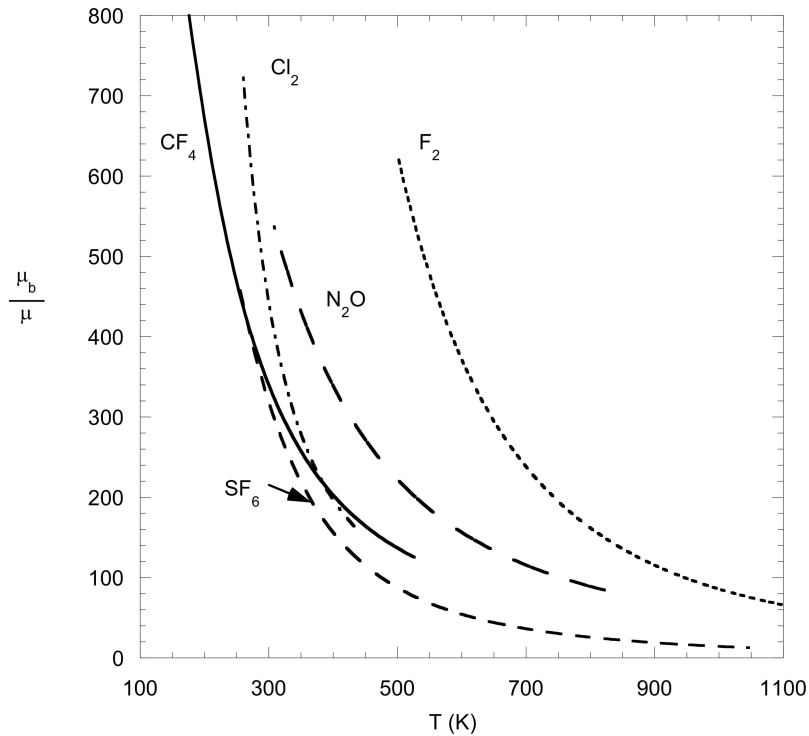


Figure 2.1: Estimation of the ratio of bulk viscosity to shear viscosity as a function of temperature for some large bulk viscosity substances

viscosities of these gases are hundreds of times the shear viscosity at room temperature. For many substances, at sufficiently low temperatures only the rotational component of bulk viscosity is active and it is increasing with temperature. At higher temperatures, also the vibrational relaxation becomes active and is decaying with temperature. Therefore a local maximum is expected in the bulk viscosity vs. temperature curve. Estimation of the ratio of bulk viscosity to shear viscosity as a function of temperature for some large bulk viscosity substances is shown in Figure 2.1. Inspection of (2.3) suggests that  $\tau_i \gg \tau_c$  whenever  $\mu_b \gg \mu$  and an important question that must be considered is whether the macroscopic or imposed time scales are much greater than the largest molecular scale. If the macroscopic scales are much larger than the molecular scales, then the fluid is said to be in local thermodynamic equilibrium (LTE) and the Navier-Stokes equations are expected to be valid; see, for example, [25]. If the macroscopic scales are on the order of the molecular scales,

then relaxation effects will be evident, we say that LTE is violated, and the Navier-Stokes equations are not formally valid. If  $t_g \equiv$  the macroscopic time scales, we must require

$$t_g \gg \max(\tau_c, \tau_i). \quad (2.6)$$

## 2.5 BZT Fluids

In Section 6 we also consider non-classical effects due to the nonlinear behavior of the fluid. The nonlinear behavior of any fluid is characterized by the fundamental derivative of gas dynamics (1.2). In the ideal gas theory, the fundamental derivative of gas dynamics is always positive and this is also the case for many fluids. Fluids with large specific heats might have regions of negative fundamental derivative of gas dynamics in the p-V diagrams. Regions of negative fundamental derivative of gas dynamics correspond to regions of downward curvature of the isentropes in p-V plane. These regions are those of interest in turbomachinery flows. In the design of aircraft and turbomachinery, shock waves play a critical role. In the standard gasdynamics theory, which assumes perfect gases, the only types of shock waves possible are compression shocks. If the fundamental derivative is less than zero, the standard thermodynamics inequalities are reversed. The phenomena associated with these fluids will result in disintegration of compression shocks and therefore reductions of adverse pressure gradient. The comparison of flow around turbine blades between classical and this type of fluids has been sketched in Figure 2.2. This figure shows the problem with shock waves in a turbine cascade. As these shocks collide with a second blade, they can cause the boundary layer to detach, causing a large increase in drag. In BZT fluids, compression fans replace compression shocks, spreading the pressure change over a large area and reducing drag. Fluids which exhibit this behavior are referred to as the Bethe-Zel'dovich-Thompson (BZT) fluids. For a more complete discussion of the fundamental behavior of BZT

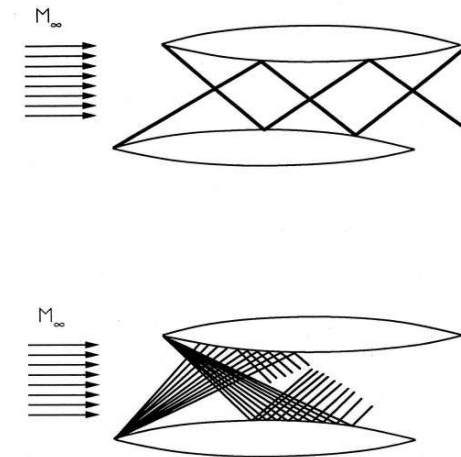


Figure 2.2: Comparison of the turbine cascade flow of a classical fluid and a BZT fluid.

fluids, we refer the reader to the articles by [26], [27] and [28].

Interest in BZT fluids is due to the possibility of reducing separation. Another important motivation comes from the possible applications of non-classical effects, especially in the area of turbine dynamics for Rankine cycle power systems where BZT fluids may be able to increase the efficiency and the life of turbines. In these turbines, a major cause of inefficiency is the very large pressure gradient caused by compression shocks striking adjacent blades and, in transonic flows, on the blade themselves. This strong adverse pressure gradient can separate the boundary layer leading to flow separation and its associated loss of efficiency and vibration.

In Chapter 5 we use the weak shock theory of Crickenberger [29] to illustrate how these non-classical physical effects can influence flows commonly encountered in practice.

## Chapter 3

# Inviscid-Viscous Flows with Large Bulk

## Viscosity

We examine the inviscid and boundary layer approximations in fluids having bulk viscosities which are large compared to their shear viscosities for three-dimensional steady flows over rigid bodies. We examine the first order corrections to the classical lowest order inviscid and boundary layer flows using the method of matched asymptotic expansions. It is shown that the effects of large bulk viscosity are non-negligible when the ratio of bulk to shear viscosity is on the order of the Reynolds number to the inverse one-half power. The first order outer flow is seen to be rotational, non-isentropic, and viscous but satisfies the slip condition at the inner boundary. First order corrections to the boundary layer flow include a variation of the thermodynamic pressure across the boundary layer and a term interpreted as a heat source in the energy equation. The latter results are a generalization and verification of the predictions of Emanuel [24].

### 3.1 Introduction

The inviscid approximation is the foundation of aerodynamics and modern fluid dynamics. In its simplest form it states that most of the flow can be regarded as frictionless and as having negligible heat conduction provided an appropriately defined Reynolds number is sufficiently large. The bulk of the flow is then determined by the Euler equations which are solved subject only to the no-penetration or kinematic boundary condition at material boundaries, e.g., at the surface of solid bodies. The resultant inviscid solutions are the basis of most textbook presentations of fluid mechanics and aerodynamics. In such large Reynolds number flows, the no-slip condition is satisfied once a viscous boundary layer forms in the neighborhood of the solid boundary. Such viscous boundary layers are the physical source of flow vorticity, the Kutta condition, separation, heat transfer, and drag. The deceleration of the flow in the boundary layer causes an outward displacement of the flow; this effective thickening of the body, wing, or turbine blade is called the displacement thickness and plays a key role in the study of viscous-inviscid interactions. The perturbations to the inviscid flow caused by this displacement thickness are of order  $Re^{-1/2}$ , where  $Re$  is the abovementioned Reynolds number, and are typically inviscid, irrotational, and isentropic. The perturbed inviscid flow can then be used to compute the next correction to the boundary layer, which can be used to compute further corrections to the inviscid flow. While the availability of high-speed computers may render such iterative schemes unnecessary for detailed flow computations, the conceptual structure is nevertheless essential for the interpretation of numerical and experimental studies.

The primary goal of the present study is to determine the effect of the bulk viscosity

$$\mu_b = \lambda + \frac{2}{3}\mu, \quad (3.1)$$

where  $\mu$ ,  $\lambda$  and  $\mu_b$  are the shear, second, and bulk viscosities of the fluid, on the structure of the

inviscid approximation. In particular, we delineate how the inviscid portion of the flow and the boundary layer must be modified when the bulk viscosity is large compared to the shear viscosity. An early study of the bulk viscosity in low pressure gases has been carried out by Tisza [30] who showed that the zero-frequency, near-equilibrium value of the bulk viscosity is given by

$$\mu_b = \mu_b(T) = (\gamma - 1)^2 \sum_{i=1}^N \frac{c_{v|i}}{R} p \tau_i, \quad (3.2)$$

where  $T$  is the absolute temperature,  $\gamma$  is the ratio of specific heats,  $c_{v|i}$  is the isochoric specific heat corresponding to the  $i^{th}$  internal energy storage mode, i.e., the rotational and vibrational modes,  $R$  is the gas constant,  $p$  is the thermodynamic pressure, and  $\tau_i$  is the relaxation time corresponding to  $i^{th}$  mode. The summation is over all the internal energy storage modes. One of the earliest numerical estimates for the bulk viscosity of an ideal gas was Tisza [30] who gave a value of  $\mu_b/\mu = O(10^3)$  for  $\text{CO}_2$  at room temperature and pressure. More recent studies have determined the bulk viscosity for a variety of fluids; see, e.g., Graves and Argrow [25] and Cramer [23]. In the latter study, a number of common fluids were found to have bulk viscosities which were hundreds to thousands of times larger than their shear viscosities. Examples of the temperature variation of the ratio of bulk to shear viscosity of selected fluids are provided in Figure 2.1. The details of the data used and estimation techniques are provided in Cramer [23]. As discussed by Cramer [23], fluids having large bulk viscosities include those used as working fluids in power systems having non-fossil fuel heat sources. It is therefore natural to ask whether the dynamics of fluids with relatively large bulk viscosity are qualitatively or quantitatively different than those where  $\mu_b = O(\mu)$ . In the present study we examine the inviscid flow and boundary layer associated with a steady flow around rigid three-dimensional bodies. A sketch of the configuration is provided in Figure 3.1. We include the possibility that the bulk viscosity is much larger than the shear viscosity and describe the corrections required when  $\mu_b \gg \mu$ . Because the bulk viscosity is proportional to the relaxation times for the internal modes the possibility that the flow will no longer be in

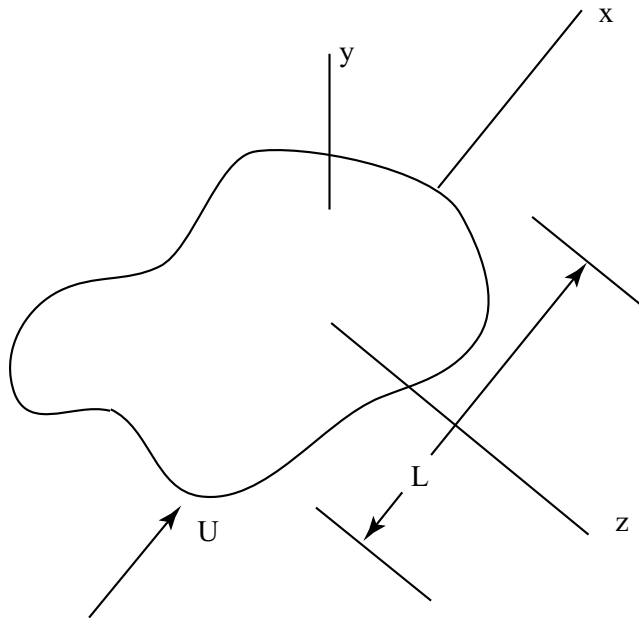


Figure 3.1: Sketch of global coordinate system and body. The freestream speed is aligned with the positive  $x$ -axis and has magnitude  $U$ . The length scale measuring the size of the body is  $L$ .

equilibrium must be considered. In order to ensure that the Navier-Stokes equations are valid we must require that the flow be in near equilibrium, i.e., that  $t_g \gg \tau_{max}$ , where  $t_g$  is the global time scale imposed by the boundary and the initial conditions and  $\tau_{max}$  is the largest relevant molecular time scale. Following Graves and Argrow [25], we refer to this near-equilibrium condition as local thermodynamic equilibrium (LTE). If we formally restrict attention to low pressure gases and denote the typical molecular collision time as  $\tau_c$ , the size of the shear viscosity is given by:

$$\mu = O(p\tau_c). \quad (3.3)$$

The Reynolds number associated with a body of size  $L$  and a freestream speed of  $U$  is  $Re = \frac{U\rho L}{\mu}$  where  $\rho$  is the fluid density. If we note that  $t_g = O(L/U)$  and use equation (3.3), we find that

$$Re = O(M_\infty^2 \frac{t_g}{\tau_c}), \quad (3.4)$$



where  $M_\infty \equiv$  the freestream Mach number. Thus, when the Mach number is moderate,  $t_g \gg \tau_c$  for all large Reynolds number flows. However, if we combine (3.2) with (3.3), we find that

$$\frac{\mu_b}{\mu} = O\left(\frac{\tau_i}{\tau_c}\right). \quad (3.5)$$

Thus, for  $\mu_b \gg \mu$ ,  $\tau_i \gg \tau_c$ , and we need to show that  $t_g \gg \tau_i \gg \tau_c$  in order that LTE be satisfied for the flows considered here. An estimate of the size of  $\mu_b/\mu$  needed in the present study can be obtained by recalling that the first correction to classical large Reynolds number, i.e., inviscid, flow is due the displacement thickness effects generated by the boundary layer. As pointed out above, these displacement thickness effects are of order

$$\delta \equiv Re^{-1/2} \ll 1. \quad (3.6)$$

In particular, the perturbations to the thermodynamic pressure due to the displacement thickness are of order  $\rho U^2 \delta$ . The size of the normal component of the viscous stress tensor is of order  $\mu_b \nabla \cdot \mathbf{v}$ , where  $\mathbf{v}$  is the velocity vector. If we note that  $\nabla \cdot \mathbf{v} = O(U/L)$ , we find that the ratio of (normal) viscous stress to the pressure perturbations associated with displacement thickness is

$$O\left(\mu_b \frac{U}{L} \frac{1}{\rho \delta U^2}\right) = O\left(\frac{\mu_b}{\mu} \frac{1}{\delta Re}\right) = O\left(\frac{\mu_b}{\mu} \frac{1}{Re^{1/2}}\right). \quad (3.7)$$

Thus, the viscous effects associated with the bulk viscosity are on the same order as the correction due to the displacement thickness when

$$\frac{\mu_b}{\mu} = O(Re^{1/2}) = O(\delta^{-1}) \gg 1, \quad (3.8)$$

where (3.6) has been used. If  $\mu_b = O(\mu)$ , then (3.8) cannot be satisfied and we recover the conclusion of the classical inviscid theory that viscous effects are always much smaller than displacement

thickness effects. In all that follows, we employ (3.8) for the sake of convenience. However, we have also derived (3.8) by a detailed asymptotic analysis of the full Navier-Stokes equations. If we now substitute (3.4)-(3.5) in (3.8) and multiply (3.8) by  $\tau_c/t_g$ , we find that

$$\frac{t_i}{t_g} = O\left(\left(\frac{t_c}{t_g}\right)^{1/2}\right) \ll 1, \quad (3.9)$$

where (3.4) and (3.6) have been used. Thus, for the problems considered here,  $t_g \gg \tau_i \gg \tau_c$  and LTE is satisfied.

In all that follows, we therefore take the flows to be governed by the Navier-Stokes equations. The equations, boundary conditions, and flow parameters are provided in Section 3.2. In Section 3.3, we develop the outer approximation to the exact equations to first order in  $Re^{-1/2}$ . In Section 3.3 we also describe the vorticity and entropy generated by the non-negligible bulk viscosity. A modified Bernoulli equation, valid to first order, is also provided. In Section 3.4, we find the first order boundary layer approximation for general three-dimensional bodies and flows through use of the curvilinear coordinate system described in Appendix B. In Section 3.5, we match the two first order approximations using the method of matched asymptotic expansions. Although viscous effects are non-negligible at  $O(\delta)$  in the outer flow, the result of the matching is that the first order outer flow is seen to slip freely at the solid boundary. The outer flow is therefore seen to be inviscid and classical at lowest (zeroth) order and slips even up to first order. At first order, the outer flow is affected by both bulk viscosity effects and the classical displacement thickness effects. In Section 3.6, we specialize to the case of a flat plate in order to provide explicit illustrations of the effects of relatively large bulk viscosity on the boundary layer. We verify Emanuel's result [24] that the pressure is not constant across the boundary layer at first order, but has a  $Re^{-1/2}$  variation.

## 3.2 Formulation

The flow is taken to be steady and such that the body force and volumetric energy supply is negligible. As pointed out in the previous section, the single-phase, non-reacting fluid is taken to be an arbitrary Navier-Stokes fluid. The resultant mass, linear momentum, and energy equations can therefore be written

$$\nabla \cdot (\mathbf{v}\rho) = 0, \quad (3.10)$$

$$\rho\mathbf{v} \cdot \nabla\mathbf{v} + \nabla p = \nabla \cdot \underline{\underline{T}}, \quad (3.11)$$

$$\rho T\mathbf{v} \cdot \nabla s = \Phi - \nabla \cdot \mathbf{q}, \quad (3.12)$$

where  $\mathbf{v} = \mathbf{v}(\mathbf{x})$ ,  $\rho = \rho(\mathbf{x})$ , and  $s = s(\mathbf{x})$  are the fluid velocity, density, and entropy, and  $\mathbf{x}$  represents the spatial coordinates. The scalar  $\Phi$  is the viscous dissipation given by

$$\Phi \equiv \text{tr} \left( \underline{\underline{T}} (\nabla\mathbf{v})^T \right), \quad (3.13)$$

where the superscript  $T$  denotes the transpose of the indicated quantity and  $\text{tr}$  denotes the trace. The heat flux vector ( $\mathbf{q}$ ) and the viscous part of the stress ( $\underline{\underline{T}}$ ) are given by

$$\mathbf{q} \equiv -k\nabla T, \quad (3.14)$$

$$\underline{\underline{T}} \equiv \lambda \nabla \cdot \mathbf{v} \underline{\underline{I}} + \mu \left[ \nabla\mathbf{v} + (\nabla\mathbf{v})^T \right], \quad (3.15)$$

where  $\underline{\underline{I}}$  is the identity matrix and  $k = k(\rho, T)$  is the thermal conductivity. The thermodynamic variables are related through Gibbs' relation

$$dh = Tds + \frac{1}{\rho}dp, \quad (3.16)$$

where

$$h \equiv e + \frac{p}{\rho} \quad (3.17)$$

is the fluid enthalpy and  $e = e(\rho, T)$  is the fluid energy per unit volume.

It can be shown that the above system is closed once we specify

$$p = p(\rho, T) \quad (3.18)$$

$$c_{v\infty} = c_{v\infty}(T) \quad (3.19)$$

and the dependencies of  $\mu$ ,  $\lambda$ ,  $k$  on either  $p$  and  $T$  or  $\rho$  and  $T$ . The relation (3.18) is recognized as the equation of state and  $c_{v\infty} = c_{v\infty}(T)$  is the ideal gas or zero-pressure isochoric specific heat.

The constraints on these constitutive properties are that

$$k, \mu, \mu_b \geq 0, \quad (3.20)$$

$$c_v = c_v(\rho, T) \equiv T \left. \frac{\partial s}{\partial T} \right|_{\rho} \geq 0, \quad (3.21)$$

$$\left. \frac{\partial p}{\partial \rho} \right|_T \geq 0. \quad (3.22)$$

The first set of inequalities are necessary and sufficient conditions for the Navier-Stokes equations to satisfy the second law of thermodynamics and (3.21)-(3.22) are required in order to ensure a stable thermodynamic equilibrium.

The body is stationary, rigid, and impenetrable, but otherwise arbitrary with a unit outward normal ( $\mathbf{n}$ ) as sketched in Figure 3.1. If the body surface is taken to be  $F(\mathbf{x}) = 0$ , the combination of no-slip and no-penetration condition at the body surface therefore is

$$\mathbf{v} \cdot \mathbf{n} = 0 \quad (3.23)$$

on  $F(\mathbf{x}) = 0$ . For either a constant temperature or an adiabatic boundary condition we will take

$$T = T_w = \text{constant} \quad (3.24)$$

or

$$\mathbf{n} \cdot \nabla T = 0 \quad (3.25)$$

on  $F(\mathbf{x}) = 0$ . Far from the body the flow is taken to be uniform and parallel to the positive  $x$ -axis, i.e.,

$$\mathbf{v} \rightarrow U\mathbf{i}; T, p, \rightarrow T_\infty, p_\infty, \quad (3.26)$$

as  $|\mathbf{x}| \rightarrow \infty$ , where  $U = \text{constant}$  and subscripts  $\infty$  will always refer to flow properties far from the body.

We now nondimensionalize the equations of motion as follows

$$\begin{aligned} \mathbf{v} &= U\bar{\mathbf{v}}, \\ \rho &= \rho_\infty\bar{\rho}, \\ p - p_\infty &= \rho_\infty U^2\bar{p}, \\ T &= T_\infty\bar{T}, \\ s - s_\infty &= c_{p\infty}\bar{s}, \\ \mathbf{x} &= L\bar{\mathbf{x}}, \quad \nabla = \frac{1}{L}\bar{\nabla}, \end{aligned} \quad (3.27)$$

where  $c_{p\infty} =$  the specific heat at constant pressure evaluated in the freestream. As a result, (3.10)-

(3.12) can be rewritten as

$$\bar{\nabla} \cdot (\bar{\mathbf{v}}\bar{\rho}) = 0 \quad (3.28)$$

$$\bar{\rho}\bar{\mathbf{v}} \cdot \bar{\nabla}\bar{\mathbf{v}} + \bar{\nabla} \left[ \bar{p} - \frac{\bar{\mu}_b}{Re} \nabla \cdot \bar{\mathbf{v}} \right] = \frac{1}{Re} \bar{\nabla} \cdot \bar{\underline{\underline{T}}}_0 \quad (3.29)$$

$$\bar{\rho}\bar{T}\bar{\mathbf{v}} \cdot \bar{\nabla}\bar{s} = \frac{1}{Re} \left[ E (\bar{\Phi}_0 + \bar{\mu}_b(\bar{\nabla} \cdot \bar{\mathbf{v}})^2) - \frac{1}{Pr} \bar{\nabla} \cdot \bar{\mathbf{q}} \right]. \quad (3.30)$$

The boundary conditions (3.23)-(3.26) can be written

$$\bar{\mathbf{v}} \cdot \mathbf{n} = 0 \quad (3.31)$$

$$\bar{T} = \bar{T}_w = \text{constant or } \mathbf{n} \cdot \bar{\nabla}\bar{T} = 0$$

on  $F(\bar{\mathbf{x}}) = 0$  and

$$\bar{\mathbf{v}} \rightarrow \mathbf{i} \quad (3.32)$$

$$\bar{\rho}, \bar{T} \rightarrow 1$$

$$\bar{p}, \bar{s} \rightarrow 0$$

as  $|\bar{\mathbf{x}}| \rightarrow \infty$ . Here  $Re \equiv U\rho_\infty L/\mu_\infty$ ,  $Pr = \mu_\infty c_{p\infty}/k_\infty$ ,  $E = U^2/T_\infty c_{p\infty}$  are the Reynolds number, Prandtl number, and Eckert number. The quantities  $\mu_\infty$  and  $k_\infty$  are the shear viscosity and thermal conductivity evaluated in the freestream. The quantities

$$\bar{\mathbf{q}} \equiv -\bar{k}\bar{\nabla}\bar{T} = \frac{L}{k_\infty T_\infty} \mathbf{q}, \quad (3.33)$$

$$\bar{\underline{\underline{T}}} = \bar{\underline{\underline{T}}}_0 + \bar{\mu}_b \bar{\nabla} \cdot \bar{\mathbf{v}} \underline{\underline{I}} \equiv \frac{L}{U\mu_\infty} \underline{\underline{T}}, \quad (3.34)$$

$$\bar{\Phi} = \bar{\Phi}_0 + \bar{\mu}_b(\bar{\nabla} \cdot \bar{\mathbf{v}})^2 = \frac{L^2}{\mu_\infty U^2} \Phi, \quad (3.35)$$

are the scaled versions of (3.14), (3.15), (3.13) respectively. The nondimensional quantities  $\bar{k} \equiv$

$k/k_\infty$ ,  $\bar{\mu} \equiv \mu/\mu_\infty$ , and  $\bar{\mu}_b \equiv \mu_b/\mu_\infty$ . In (3.33)-(3.35) we have split the shear stress and viscous dissipation into the  $\mu_b = 0$  contribution, i.e.,

$$\underline{\underline{\bar{T}}}_0 = \bar{\mu} \left[ \bar{\nabla} \bar{\mathbf{v}} + (\bar{\nabla} \bar{\mathbf{v}})^T - \frac{2}{3} \bar{\nabla} \cdot \bar{\mathbf{v}} \underline{\underline{I}} \right], \quad (3.36)$$

$$\bar{\Phi}_0 = \text{tr} \left[ \underline{\underline{\bar{T}}}_0 (\bar{\nabla} \bar{\mathbf{v}})^T \right], \quad (3.37)$$

and the  $\mu_b \neq 0$  contributions. Equation (3.36) can also be recognized as the nondimensionalized version of the deviatoric viscous stress tensor.

In all that follows we will take the Reynolds number to be large, the Prandtl and Eckert numbers to be of order-one, and  $\bar{\mu}_b = O(Re^{\frac{1}{2}}) \gg 1$ .

### 3.3 Outer Solution

We now seek approximations to (3.28)-(3.30) for the lowest-order outer flow as well as its first correction by expanding the dependent variables as follows:

$$\begin{aligned}
 \bar{\mathbf{v}} &= \mathbf{V}_0 + \delta \mathbf{V}_1 + O(\delta^2), \\
 \bar{p} &= P_0 + \delta P_1 + O(\delta^2), \\
 \bar{T} &= T_0 + \delta T_1 + O(\delta^2), \\
 \bar{\rho} &= R_0 + \delta R_1 + O(\delta^2), \\
 \bar{s} &= S_0 + \delta S_1 + O(\delta^2),
 \end{aligned} \tag{3.38}$$

where

$$\delta \equiv Re^{-\frac{1}{2}} \ll 1, \tag{3.39}$$

and as suggested in the introduction,  $\bar{\mu}_b = O(\delta^{-1})$ . Here each component of  $\bar{\mathbf{x}}$  will be scaled the same as the others and, in anticipation of the existence of the boundary layer, we ignore the boundary conditions at  $F(\bar{\mathbf{x}}) = 0$ . Substitution of (3.38) in (3.28)-(3.30) yields

$$\bar{\nabla} \cdot (\tilde{\rho} \tilde{\mathbf{v}}) = O(\delta^2), \tag{3.40}$$

$$\tilde{\rho} \tilde{\mathbf{v}} \cdot \bar{\nabla} \tilde{\mathbf{v}} + \bar{\nabla} [\tilde{p} - \bar{\mu}_b \delta^2 \bar{\nabla} \cdot \tilde{\mathbf{v}}] = O(\delta^2), \tag{3.41}$$

$$\tilde{\mathbf{v}} \cdot \bar{\nabla} \tilde{s} = E \frac{\bar{\mu}_b \delta^2}{\tilde{\rho} \tilde{T}} (\bar{\nabla} \cdot \tilde{\mathbf{v}})^2 + O(\delta^2), \tag{3.42}$$



where we have defined

$$\begin{aligned}
\tilde{\mathbf{v}} &\equiv \mathbf{V}_0 + \delta \mathbf{V}_1, \\
\tilde{p} &\equiv P_0 + \delta P_1, \\
\tilde{T} &\equiv T_0 + \delta T_1, \\
\tilde{\rho} &\equiv R_0 + \delta R_1, \\
\tilde{s} &\equiv S_0 + \delta S_1,
\end{aligned} \tag{3.43}$$

to simplify the appearance of (3.40)-(3.42). It should be noted that terms explicitly recorded in (3.40)-(3.42) will also contain terms which are of  $O(\delta^2)$  and such terms should be ignored when more detailed expansions are carried out. We also note that the lowest-order version of (3.40)-(3.42) can be written

$$\bar{\nabla} \cdot (R_0 \mathbf{V}_0) = 0, \tag{3.44}$$

$$R_0 \mathbf{V}_0 \cdot \bar{\nabla} \mathbf{V}_0 + \bar{\nabla} P_0 = \mathbf{0}, \tag{3.45}$$

$$\mathbf{V}_0 \cdot \bar{\nabla} S_0 = 0, \tag{3.46}$$

which are recognized as the classical equations governing inviscid isentropic flow. When  $\bar{\mu}_b = O(1)$ , (3.40)-(3.42) also reduce to the equations of inviscid, isentropic flow. Thus, in the classical  $\bar{\mu}_b = O(1)$  theory, the  $O(\delta)$  perturbations are caused only by the boundary layer displacement thickness. In the present case, we take  $\bar{\mu}_b = O(\delta^{-1})$  and the viscous terms proportional to  $\bar{\mu}_b$  are non-negligible at first-order. That is, first-order corrections to the outer flow are due to both classical displacement thickness effects and (bulk) viscous effects when  $\bar{\mu}_b = O(Re^{\frac{1}{2}}) = O(\delta^{-1})$ . The viscous effects are seen to be related to the compressibility of the lowest-order inviscid flow, i.e.,

$$\bar{\nabla} \cdot \tilde{\mathbf{v}} \approx \bar{\nabla} \cdot \mathbf{V}_0 \approx -\frac{1}{R_0} \mathbf{V}_0 \cdot \nabla R_0$$

and can be ignored if the lowest-order outer flow is incompressible.

The far-field boundary conditions (3.32) reduce to

$$\tilde{\mathbf{V}} \rightarrow \mathbf{i}, \quad \tilde{\rho} \rightarrow 1, \quad \tilde{T} \rightarrow 1, \quad \tilde{p} \rightarrow 0, \quad \tilde{s} \rightarrow 0 \quad (3.47)$$

as  $|\bar{\mathbf{x}}| \rightarrow \infty$ . By combining (3.46) and the last of (3.47), we can show that  $S_0 = 0$  for all  $\bar{\mathbf{x}}$  and that  $S_1$  is given by (3.42):

$$\mathbf{V}_0 \cdot \bar{\nabla} S_1 = E \frac{\bar{\mu}_b \delta}{R_0 T_0} (\bar{\nabla} \cdot \mathbf{V}_0)^2. \quad (3.48)$$

Thus, when  $\bar{\mu}_b = O(\delta^{-1})$ ,  $\bar{s} = O(\delta)$  in the outer flow and the perturbations caused by the displacement thickness are not only viscous but involve entropy gradients even in a shock-free flow.

The outer flow is also seen to be rotational at the order of the displacement thickness corrections. This fact can be seen by taking the curl of (3.41), by using well known vector identities and the thermodynamic identity

$$\left. \frac{\partial p}{\partial s} \right|_{\rho} = \rho T G, \quad (3.49)$$

where  $G \equiv \beta a^2 / c_p$  is the Grüneisen parameter and

$$\beta \equiv -\frac{1}{\rho} \left. \frac{\partial \rho}{\partial T} \right|_p \quad (3.50)$$

is the thermal expansivity, to yield a modified version of the vorticity transport equation. In terms of the dimensional variables this modified vorticity transport equation reads

$$\mathbf{v} \cdot \nabla \boldsymbol{\omega} \approx \boldsymbol{\omega} \cdot \nabla \mathbf{v} + \frac{1}{\rho^2} \nabla \rho \times [GT \nabla s - \nabla(\Delta)] \quad (3.51)$$

where  $\boldsymbol{\omega} \equiv \boldsymbol{\zeta}/\rho$ ,  $\boldsymbol{\zeta} \equiv \nabla \times \mathbf{v} = \text{vorticity}$ , and

$$\Delta \equiv \nu_b \nabla \cdot \mathbf{v}, \quad (3.52)$$

where  $\nu_b \equiv \mu_b/\rho$  is the kinematic bulk viscosity. The accuracy of (3.51) is identical to that of (3.40)-(3.42), i.e., the terms neglected in (3.51) are  $O(U^2\delta^2/L^2\rho_\infty)$ . The term on the left of (3.51) is the time variation of  $\boldsymbol{\omega}$  on a particle path, the first term on the right of (3.51) is the vortex stretching term and the term proportional to  $\nabla\rho \times \nabla s$  is the baroclinic vorticity generation term found in the classical inviscid version of the vorticity transport equation. The term proportional to  $\nabla\rho \times \nabla(\Delta)$  arises due to the first-order viscous term in (3.41). Because the dimensional entropy variations are of order  $\delta c_{p\infty}$ , the last two terms in (3.51) can be shown to be of first-order when  $\bar{\mu}_b = O(\delta^{-1})$ . Thus in the case considered here, i.e.,  $\bar{\mu}_b = O(\delta^{-1})$ , the last two terms on the right of (3.51) will be  $O(U^2\delta/L^2\rho_\infty)$  and the first-order outer flow will be rotational, i.e.,

$$\boldsymbol{\zeta} = O\left(\delta\frac{U}{L}\right).$$

The first-order vorticity is seen to be due to the entropy gradients caused by viscous dissipation term in (3.42) and the viscous term seen in the momentum equation (3.41).

A modified Bernoulli equation can be derived by dotting (3.41) with  $\tilde{\mathbf{v}}$  and by using standard vector identities, Gibbs' relation (3.16), and (3.42). In dimensional variables, this modified Bernoulli equation reads

$$h + \frac{|\mathbf{v}|^2}{2} - \Delta \approx \text{constant} \quad (3.53)$$

on particle paths, where  $\Delta$  is again given by (3.52). Here, the terms neglected in (3.53) are  $O(U^2\delta^2)$ . It can be shown that the shock jump conditions are the classical jump conditions with the pressure replaced by  $p - \mu_b \nabla \cdot \mathbf{v} = p - \rho\Delta$ , at least to first-order. As a result, (3.53) holds along all particle paths, including those which pass through shock waves. If we employ the boundary

conditions (3.32), we conclude that

$$H - H_\infty \approx \Delta \quad (3.54)$$

for all particle paths even when shock waves are present. Here  $H \equiv h + |\mathbf{v}|^2/2$  is the total enthalpy and  $H_\infty \equiv h_\infty + U^2/2$ . Thus, because  $\nu_b > 0$ ,

$$H \begin{cases} > \\ < \end{cases} H_\infty \text{ wherever } \nabla \cdot \mathbf{v} = -\frac{1}{\rho} \mathbf{v} \cdot \nabla \rho \begin{cases} > \\ < \end{cases} 0,$$

i.e., the total enthalpy exceeds the freestream total enthalpy in all regions where the density is decreasing along the streamline and is less than the freestream enthalpy in all regions where the density is increasing along the streamline. At stagnation points,  $\mathbf{v} = \mathbf{0}$  and the stagnation enthalpy is

$$h_s = H_\infty.$$

Because the entropy increases along every streamline due both to shock waves and the first-order energy equation (3.42), Gibbs' relation (3.16) can be used to show that the stagnation pressure, i.e., the pressure at stagnation point, will be less than the pressure obtained during an isentropic stagnation.

### 3.4 Inner Solution

We now analyze the boundary layer using the surface-oriented coordinate system defined in the appendix B. The curvilinear components of the velocities will be scaled as follows

$$v_1 = Uu, \quad v_2 = Uv, \quad v_3 = \delta Uw \quad (3.55)$$

and the spatial variables will be scaled

$$\xi_1 = L\bar{\xi}_1, \quad \xi_2 = L\bar{\xi}_2, \quad n = \delta L\hat{n}, \quad (3.56)$$

where  $u, v, w, \bar{\xi}_1, \bar{\xi}_2, \hat{n}$  will be taken to be  $O(1)$  in the boundary layer. The remaining dependent variables have the same scalings as in (3.27), i.e.,  $\rho = \rho_\infty \bar{\rho}$ ,  $p - p_\infty = \rho_\infty U^2 \bar{p}$ ,  $T = T_\infty \bar{T}$ ,  $s - s_\infty = c_{p\infty} \bar{s}$ . The mass, momentum, and energy equations (B.4)-(B.8) therefore read:

$$\frac{\partial(\bar{\rho}u)}{\partial\bar{\xi}_1} + \frac{\partial(\bar{\rho}v)}{\partial\bar{\xi}_2} + \frac{\partial(\bar{\rho}w)}{\partial\hat{n}} + \bar{\rho}u\bar{\alpha}_{21} + \bar{\rho}v\bar{\alpha}_{12} + \delta w\bar{\rho} \left( \frac{1}{\mathcal{R}_1} + \frac{1}{\mathcal{R}_2} \right) = O(\delta^2) \quad (3.57)$$

$$\begin{aligned} \bar{\rho} \left[ \widehat{\mathbf{v} \cdot \nabla} u + vu\bar{\alpha}_{12} - (v)^2\bar{\alpha}_{21} + \frac{\delta wu}{\mathcal{R}_1} \right] + \frac{\partial}{\partial\bar{\xi}_1} (\bar{p} - \delta\bar{\rho}\hat{\Delta}) \\ = \frac{\partial\hat{T}_{31}}{\partial\hat{n}} + \delta\hat{T}_{31} \left( \frac{2}{\mathcal{R}_1} + \frac{1}{\mathcal{R}_2} \right) + O(\delta^2) \end{aligned} \quad (3.58)$$

$$\begin{aligned} \bar{\rho} \left[ \widehat{\mathbf{v} \cdot \nabla} v + uv\bar{\alpha}_{21} - (u)^2\bar{\alpha}_{12} + \delta \frac{vw}{\mathcal{R}_2} \right] + \frac{\partial}{\partial\bar{\xi}_2} (\bar{p} - \delta\bar{\rho}\hat{\Delta}) \\ = \frac{\partial\hat{T}_{32}}{\partial\hat{n}} + \delta\hat{T}_{32} \left[ \frac{1}{\mathcal{R}_1} + \frac{2}{\mathcal{R}_2} \right] + O(\delta^2) \end{aligned} \quad (3.59)$$

$$\frac{\partial}{\partial\hat{n}} (\bar{p} - \delta\bar{\rho}\hat{\Delta}) = \delta\bar{\rho} \left[ \frac{(u)^2}{\mathcal{R}_1} + \frac{(v)^2}{\mathcal{R}_2} \right] + O(\delta^2), \quad (3.60)$$

$$\bar{\rho}\bar{T}\widehat{\mathbf{v} \cdot \nabla} \bar{s} = E \left[ \hat{\Phi}_0 + \delta\bar{\rho}\hat{\Delta}\widehat{\nabla \cdot \mathbf{v}} \right] - \frac{1}{Pr}\widehat{\nabla \cdot \mathbf{q}} + O(\delta^2), \quad (3.61)$$

where  $\bar{\mathcal{R}}_1 = \mathcal{R}_1/L = O(1)$ ,  $\bar{\mathcal{R}}_2 = \mathcal{R}_2/L = O(1)$ ,

$$\bar{\alpha}_{21} = L\alpha_{21} = \frac{L}{h_1 h_2} \frac{\partial h_2}{\partial \phi_1} = O(1) \quad (3.62)$$

$$\bar{\alpha}_{12} = L\alpha_{12} = \frac{L}{h_1 h_2} \frac{\partial h_1}{\partial \phi_2} = O(1). \quad (3.63)$$

The scaled version of (B.9) is

$$\widehat{\mathbf{v}} \cdot \widehat{\nabla} A \equiv \frac{L}{U} \mathbf{v} \cdot \nabla A = u \frac{\partial A}{\partial \bar{\xi}_1} + v \frac{\partial A}{\partial \bar{\xi}_2} + w \frac{\partial A}{\partial \hat{n}} \quad (3.64)$$

where  $A$  is any scalar and the scaled divergence of  $\mathbf{v}$  and  $\mathbf{q}$  are given by

$$\widehat{\nabla} \cdot \widehat{\mathbf{v}} = \frac{\partial u}{\partial \bar{\xi}_1} + \frac{\partial v}{\partial \bar{\xi}_2} + \frac{\partial w}{\partial \hat{n}} + v \bar{\alpha}_{12} + u \bar{\alpha}_{21} + \delta w \left( \frac{1}{\bar{\mathcal{R}}_1} + \frac{1}{\bar{\mathcal{R}}_2} \right) + O(\delta^2), \quad (3.65)$$

$$\widehat{\nabla} \cdot \widehat{\mathbf{q}} = - \left[ \frac{\partial}{\partial \hat{n}} \left( \bar{k} \frac{\partial \bar{T}}{\partial \hat{n}} \right) + \delta \bar{k} \left( \frac{1}{\bar{\mathcal{R}}_1} + \frac{1}{\bar{\mathcal{R}}_2} \right) \frac{\partial \bar{T}}{\partial \hat{n}} \right] + O(\delta^2). \quad (3.66)$$

The quantity  $\hat{\Delta}$  is the scaled version of (3.52), i.e.,

$$\hat{\Delta} = \frac{\rho_\infty L}{\mu_\infty U} \delta \Delta = \delta \frac{\bar{\mu}_b}{\bar{\rho}} \widehat{\nabla} \cdot \widehat{\mathbf{v}} = O(1). \quad (3.67)$$

The scaled components of the stress tensor are given by

$$\hat{T}_{31} = 2\bar{\mu} \hat{D}_{31}, \quad \hat{T}_{32} = 2\bar{\mu} \hat{D}_{32} \quad (3.68)$$

and the scaled components of the stretching tensor are

$$\begin{aligned} \hat{D}_{31} &= \frac{1}{2} \left( \frac{\partial u}{\partial \hat{n}} - \frac{\delta u}{\bar{\mathcal{R}}_1} \right) + O(\delta^2) \\ \hat{D}_{32} &= \frac{1}{2} \left( \frac{\partial v}{\partial \hat{n}} - \frac{\delta v}{\bar{\mathcal{R}}_2} \right) + O(\delta^2). \end{aligned} \quad (3.69)$$

The rescaled version of (3.37) is

$$\hat{\Phi}_0 = 4\bar{\mu} \left[ (\hat{D}_{31})^2 + (\hat{D}_{32})^2 \right] + O(\delta^2). \quad (3.70)$$

The scaled versions of the boundary conditions at the body surface are

$$u = v = w = 0 \quad (3.71)$$

and either

$$\bar{T} = \bar{T}_w = T_w/T_\infty = \text{constant for an isothermal body}$$

or

$$\frac{\partial \bar{T}}{\partial \hat{n}} = 0 \text{ for an adiabatic body} \quad (3.72)$$

on  $\hat{n} = 0$ .

Inspection of the mass, momentum and energy equations (3.57) - (3.61) reveals that the primary change to the  $\mu_b = O(\mu)$  first-order boundary layer equations is the replacement of the negative pressure by the normal stresses by  $T_{11}$ ,  $T_{22}$ , or  $T_{33}$  which are  $\approx -p + \mu_b(\nabla \cdot \mathbf{v})$  when  $\mu_b = O(\mu/\delta) = O(\mu \text{Re}^{\frac{1}{2}})$ . Similar conclusions can be made for the first-order outer flow.

The energy equation (3.61) can be recast as an equation for the temperature through use of the  $Tds$  equation

$$Tds = c_p dT - \frac{\beta T}{\rho} dp,$$

and the mass equation (3.57) to yield:

$$\bar{\rho} \bar{c}_p \widehat{\mathbf{v}} \cdot \widehat{\nabla} \bar{T} = E \hat{\Phi}_0 + ET \beta \widehat{\mathbf{v}} \cdot \widehat{\nabla} (\bar{p} - \delta \bar{\rho} \hat{\Delta}) + \delta E \left[ (\beta T - 1) \widehat{\mathbf{v}} \cdot \widehat{\nabla} (\bar{\rho} \hat{\Delta}) + \widehat{\nabla} \cdot (\mathbf{v} \bar{\rho} \hat{\Delta}) \right] - \frac{1}{Pr} \widehat{\nabla} \cdot \mathbf{q} + O(\delta^2), \quad (3.73)$$

where

$$\widehat{\nabla \cdot (\mathbf{v} \bar{\rho} \hat{\Delta})} = \frac{\partial(u \bar{\rho} \hat{\Delta})}{\partial \bar{\xi}_1} + \frac{\partial(v \bar{\rho} \hat{\Delta})}{\partial \bar{\xi}_2} + \frac{\partial(w \bar{\rho} \hat{\Delta})}{\partial \hat{n}} + u \bar{\alpha}_{21} + v \bar{\alpha}_{12} + O(\delta). \quad (3.74)$$

The quantity (3.74) is just a scaled version of  $\nabla \cdot (\mathbf{v} \rho \Delta)$  and is the scaled, steady state version of Emanuel's function  $F$  [24]. As in equations (3.58)-(3.60), the pressure appears only as the normal stress  $-\bar{p} + \delta \bar{\rho} \hat{\Delta}$ . Except for this modified pressure, the only contribution of the large bulk viscosity are the third and fourth terms on the right hand side of (3.73). The third term will affect the flow if and only if the fluid is a non-ideal, i.e., pressurized, gas. The fourth term will always contribute when the lowest-order boundary layer flow is compressible and can be regarded as a heat source for the first-order problem.

Ordinarily, we would further expand the dependent variables as follows

$$\begin{aligned} u &= u_0(\bar{\xi}_1, \bar{\xi}_2, \hat{n}) + \delta u_1(\bar{\xi}_1, \bar{\xi}_2, \hat{n}) + O(\delta^2) \\ v &= v_0(\bar{\xi}_1, \bar{\xi}_2, \hat{n}) + \delta v_1(\bar{\xi}_1, \bar{\xi}_2, \hat{n}) + O(\delta^2), \\ w &= w_0(\bar{\xi}_1, \bar{\xi}_2, \hat{n}) + \delta w_1(\bar{\xi}_1, \bar{\xi}_2, \hat{n}) + O(\delta^2), \\ \bar{\rho} &= \rho_0(\bar{\xi}_1, \bar{\xi}_2, \hat{n}) + \delta \rho_1(\bar{\xi}_1, \bar{\xi}_2, \hat{n}) + O(\delta^2), \\ \bar{p} &= p_0(\bar{\xi}_1, \bar{\xi}_2, \hat{n}) + \delta p_1(\bar{\xi}_1, \bar{\xi}_2, \hat{n}) + O(\delta^2), \\ \bar{T} &= \theta_0(\bar{\xi}_1, \bar{\xi}_2, \hat{n}) + \delta \theta_1(\bar{\xi}_1, \bar{\xi}_2, \hat{n}) + O(\delta^2). \end{aligned} \quad (3.75)$$

Although we will use the explicit expansions (3.38) and (3.75) in the next section, here we will simply regard the variables seen in (3.57)-(3.61) and associated equations as representing the first two terms of the expansions (3.75). A similar grouping of terms was convenient in the examination of the outer flow in Section 3.3.



### 3.5 Matching

We now establish the boundary conditions for the outer flow at the inner boundary, i.e., the body surface, and the boundary conditions satisfied by the boundary layer variables as the outer flow is approached using the method of matched asymptotic expansions by Van Dyke [31]. The matching will be carried out in the curvilinear coordinate system described in the Appendix B. The independent variables in the outer region of Section 3.3 will be taken to be  $\bar{\xi}_1, \bar{\xi}_2, \bar{n} \equiv n/L = \delta \hat{n}$  and the dependent variables in the boundary layer will be taken to be  $\bar{\xi}_1, \bar{\xi}_2, \hat{n} \equiv \bar{n}/\delta$ . The velocity components in the outer region will be written

$$\begin{aligned}
 \bar{v}_1 &= U_0(\bar{\xi}_1, \bar{\xi}_2, \bar{n}) + \delta U_1(\bar{\xi}_1, \bar{\xi}_2, \bar{n}) + O(\delta^2) \\
 \bar{v}_2 &= V_0(\bar{\xi}_1, \bar{\xi}_2, \bar{n}) + \delta V_1(\bar{\xi}_1, \bar{\xi}_2, \bar{n}) + O(\delta^2) \\
 \bar{v}_3 &= W_0(\bar{\xi}_1, \bar{\xi}_2, \bar{n}) + \delta W_1(\bar{\xi}_1, \bar{\xi}_2, \bar{n}) + O(\delta^2)
 \end{aligned} \tag{3.76}$$

and the remaining dependent variables will be given by the forms seen in (3.38) with independent variables taken to be  $\bar{\xi}_1, \bar{\xi}_2, \bar{n}$ .

Here we will simply summarize the results of the formal matching of the first-order outer solution to the first-order boundary layer solution. The details of the matching of the 1, 2 components of the velocity and the pressure, density and temperature are essentially the same and result in constraints on the boundary layer solution only. These constraints can be written

$$\begin{aligned}
 u_0(\bar{s}_1, \bar{s}_2, \hat{n}) &\sim U_0(\bar{\xi}_1, \bar{\xi}_2, 0) + o(1), \\
 v_0(\bar{s}_1, \bar{s}_2, \hat{n}) &\sim V_0(\bar{\xi}_1, \bar{\xi}_2, 0) + o(1), \\
 \rho_0(\bar{s}_1, \bar{s}_2, \hat{n}) &\sim R_0(\bar{\xi}_1, \bar{\xi}_2, 0) + o(1), \\
 \theta_0(\bar{s}_1, \bar{s}_2, \hat{n}) &\sim T_0(\bar{\xi}_1, \bar{\xi}_2, 0) + o(1), \\
 p_0(\bar{s}_1, \bar{s}_2, \hat{n}) &\sim P_0(\bar{\xi}_1, \bar{\xi}_2, 0) + o(1),
 \end{aligned} \tag{3.77}$$

$$\begin{aligned}
u_1(\bar{\xi}_1, \bar{\xi}_2, \hat{n}) &\sim \hat{n} \frac{\partial U_0}{\partial \bar{n}}(\bar{\xi}_1, \bar{\xi}_2, 0) + U_1(\bar{\xi}_1, \bar{\xi}_2, 0) + o(1), \\
v_1(\bar{\xi}_1, \bar{\xi}_2, \hat{n}) &\sim \hat{n} \frac{\partial V_0}{\partial \bar{n}}(\bar{\xi}_1, \bar{\xi}_2, 0) + V_1(\bar{\xi}_1, \bar{\xi}_2, 0) + o(1), \\
\rho_1(\bar{\xi}_1, \bar{\xi}_2, \hat{n}) &\sim \hat{n} \frac{\partial R_0}{\partial \bar{n}}(\bar{\xi}_1, \bar{\xi}_2, 0) + R_1(\bar{\xi}_1, \bar{\xi}_2, 0) + o(1), \\
\theta_1(\bar{\xi}_1, \bar{\xi}_2, \hat{n}) &\sim \hat{n} \frac{\partial T_0}{\partial \bar{n}}(\bar{\xi}_1, \bar{\xi}_2, 0) + T_1(\bar{\xi}_1, \bar{\xi}_2, 0) + o(1), \\
p_1(\bar{\xi}_1, \bar{\xi}_2, \hat{n}) &\sim \hat{n} \frac{\partial P_0}{\partial \bar{n}}(\bar{\xi}_1, \bar{\xi}_2, 0) + P_1(\bar{\xi}_1, \bar{\xi}_2, 0) + o(1),
\end{aligned} \tag{3.78}$$

as  $\hat{n} \rightarrow \infty$ . Here the terms on the right-hand sides of (3.77)-(3.78) are computed from the lowest-order and first-order outer solutions. Because there are no constraints on the 1 and 2 components of velocity in the outer region, the outer flow will be free to slip at the body surface even though viscous effects are non-negligible at first-order when  $\bar{\mu}_b = 0(\delta^{-1})$ .

The matching of the normal component of velocity proceeds slightly differently and yields different results due to the fact that  $v_3 = O(U\delta)$  in the boundary layer and  $v_3 = O(U)$  in the outer flow.

The result of this matching yields

$$\begin{aligned}
W_0(\bar{\xi}_1, \bar{\xi}_2, 0) &= 0 \\
W_1(\bar{\xi}_1, \bar{\xi}_2, 0) &= \lim_{\hat{n} \rightarrow \infty} \left\{ w_0(\bar{\xi}_1, \bar{\xi}_2, \hat{n}) - \hat{n} \frac{\partial W_0}{\partial \bar{n}}(\bar{\xi}_1, \bar{\xi}_2, 0) \right\}.
\end{aligned} \tag{3.79}$$

The first of (3.79) requires that the lowest-order outer flow satisfies the no-penetration condition and the second condition of (3.79) provides the  $O(\delta)$  perturbation leading to boundary layer displacement thickness effects. If we compare the above conditions to those obtained in the classical, i.e.,  $\mu_b = O(\mu)$ , boundary layer theory, we see that the boundary conditions for the inner and outer flows are unchanged when  $\mu_b = O(\mu/\delta)$ . The primary difference, at least in the present context, is the addition of the normal stress  $\mu_b(\nabla \cdot \mathbf{v})$  to the equations of motion. Furthermore, the general procedure for the computation of the higher-order corrections to the inner and outer flows is

essentially unchanged.

### 3.6 Flat-Plate Boundary Layer

In this section we determine the simplification to the boundary layer equations (3.57)-(3.60) and (3.73) possible when we restrict the flow to be two-dimensional and over a flat plate. The condition of two-dimensional flow requires that all derivatives in the  $\phi_2$  direction are zero and that  $v = 0$ . In order that the surface be two-dimensional we take  $\mathbf{f} = y_1\mathbf{i} + y_2\mathbf{j}$  in (B.1), where  $\mathbf{i}, \mathbf{j}$  are the cartesian base vectors in the flow and transverse directions, respectively. As a result, we may take

$$a_1 = a_2 = 1 \text{ and } \mathcal{R}_1, \mathcal{R}_2 \rightarrow \infty,$$

from which we conclude that  $h_1 = h_2 = 1$  and  $\alpha_{12} = \alpha_{21} = 0$ . Thus (3.60) can be integrated to yield

$$\bar{p} - \delta\bar{\rho}\hat{\Delta} = \text{function of } \bar{\xi} \text{ only,} \quad (3.80)$$

where we have written  $\bar{\xi} = \bar{\xi}_1$ . For a two-dimensional flow over a flat plate, the lowest-order outer flow solution can be written

$$P_0, S_0 = 0, R_0 = T_0 = 1, \mathbf{V}_0 = \mathbf{i}. \quad (3.81)$$

The matching condition on the pressure (3.77)-(3.78) yields

$$\bar{p} \sim \delta P_1(\bar{\xi}, 0) \text{ as } \hat{n} \rightarrow \infty. \quad (3.82)$$

The matching conditions on velocity and density along with the mass equation (3.57) yields

$$\hat{\Delta} \rightarrow 0 \text{ as } \hat{n} \rightarrow \infty. \quad (3.83)$$

Thus, by combining (3.80), (3.82)-(3.83) we find that

$$\bar{p} = \delta[P_1(\bar{\xi}, 0) + \bar{\rho}\hat{\Delta}] + O(\delta^2) \quad (3.84)$$

for all  $\bar{\xi}, \hat{n}$ . Thus, the pressure in the boundary layer is given by the classical perturbation in the outer solution due to the displacement thickness and the normal stress associated with the bulk viscosity; the latter is represented by the second term in (3.84). The perturbation in  $\bar{p}$  due to the bulk viscosity can be written

$$\bar{\rho}\hat{\Delta} \approx \delta\bar{\mu}_b(\rho_0, \theta_0) \left( \frac{\partial u_0}{\partial \bar{\xi}} + \frac{\partial w_0}{\partial \hat{n}} \right) \quad (3.85)$$

and will vary with both  $\bar{\xi}$  and  $\hat{n}$ . Thus, when  $\mu_b = O(\mu/\delta) = O(\mu\text{Re}^{1/2})$ , the first-order pressure is no longer constant across the flat plate boundary layer. The mass equation and plate conditions (3.71) can be used to show that  $\hat{\Delta} = 0$  at  $\hat{n} = 0$ . As a result, there is at least one local maximum or minimum in the  $\bar{\rho}\hat{\Delta}$  vs  $\hat{n}$  curve.

By substitution of (3.84) in (3.57), (3.58), and (3.73) we obtain the following reduced forms of the

first-order boundary layer equations:

$$\frac{\partial(\bar{\rho}u)}{\partial\bar{\xi}} + \frac{\partial(\bar{\rho}w)}{\partial\hat{n}} = O(\delta^2), \quad (3.86)$$

$$\bar{\rho} \left[ u \frac{\partial u}{\partial\bar{\xi}} + w \frac{\partial u}{\partial\hat{n}} \right] + \delta \frac{dP_1}{d\bar{\xi}} = \frac{\partial}{\partial\hat{n}} \left( \bar{\mu} \frac{\partial u}{\partial\hat{n}} \right) + O(\delta^2), \quad (3.87)$$

$$\begin{aligned} \bar{\rho} \bar{c}_p \left[ u \frac{\partial \bar{T}}{\partial\bar{\xi}} + w \frac{\partial \bar{T}}{\partial\hat{n}} \right] &= E \bar{\mu} \left( \frac{\partial u}{\partial\hat{n}} \right)^2 + \frac{1}{Pr} \frac{\partial}{\partial\hat{n}} \left( \bar{k} \frac{\partial \bar{T}}{\partial\hat{n}} \right) \\ &+ E \delta \beta T u \frac{dP_1}{d\bar{\xi}} + E \delta \left[ (\beta T - 1) \widehat{\mathbf{v}} \cdot \widehat{\nabla} (\bar{\rho} \hat{\Delta}) + \widehat{\nabla} \cdot (\mathbf{v} \bar{\rho} \hat{\Delta}) \right] + O(\delta^2), \end{aligned} \quad (3.88)$$

where the transverse component of the momentum equation (3.59) is satisfied automatically. The boundary conditions corresponding to (3.86)-(3.88) are the  $v = 0$  versions of (3.71)-(3.72) and

$$\begin{aligned} u &\sim 1 + \delta U_1(\bar{\xi}, 0) \\ \bar{\rho} &\sim 1 + \delta R_1(\bar{\xi}, 0) \\ \bar{T} &\sim 1 + \delta T_1(\bar{\xi}, 0) \end{aligned} \quad (3.89)$$

as  $\hat{n} \rightarrow \infty$ .

Because the outer flow is a uniform flow, it can be shown that mass and momentum equations, (3.86)-(3.87), are of exactly the same form as those of the classical  $\mu_b = O(\mu)$  first-order theory. The energy equation (3.88) differs from the classical first-order flat plate equation only through the last two terms of (3.88).

We conclude this section by computing the pressure variation (3.84). The detailed calculation of each term in (3.84) requires a detailed solution of the lowest-order version of the boundary layer equations (3.86)-(3.89) which is recognized as the classical lowest-order boundary layer solution for a flat plate. As a result, we employ a conventional Levy-Lees similarity transform to the lowest-

order versions of (3.84)-(3.89). The second term in (3.84) may then be written

$$\bar{\rho}\hat{\Delta} = -\delta\bar{\mu}_b \frac{\beta T}{2\bar{\xi}} F \frac{\theta'_0}{\theta_0}, \quad (3.90)$$

where  $\theta'_0 \equiv d\theta_0/d\eta$ ,  $\eta$  is the Levy-Lees similarity variable

$$\eta \equiv \frac{1}{\sqrt{2\bar{\xi}}} \int_0^{\hat{n}} \rho_0 d\hat{n} \quad (3.91)$$

and  $F = F(\eta)$  is the nondimensional version of the stream function

$$\psi \equiv (2\rho_\infty\mu_\infty U\xi)^{\frac{1}{2}} F(\eta). \quad (3.92)$$

Relation (3.90) holds for arbitrary fluids. If the fluid is an ideal gas  $\beta T = 1$  and (3.90) simplifies slightly.

We denote the dimensional form of the boundary layer and displacement thicknesses by  $\delta Ld(\bar{\xi})$  and  $\delta Ld^*(\bar{\xi})$ , respectively. The scaled boundary layer thickness  $d(\bar{\xi})$  is then given by inverting (3.91) to yield

$$d(\bar{\xi}) \equiv \sqrt{2\bar{\xi}} \int_0^{\eta_e} \frac{1}{\rho_0} d\eta, \quad (3.93)$$

where  $\eta_e$  is the value of the similarity variable at the edge of the boundary layer. In terms of the Levy-Lees similarity variable, the scaled version of the displacement thickness is given by

$$d^*(\bar{\xi}) \equiv \sqrt{2\bar{\xi}} \int_0^\infty \left( \frac{1}{\rho_0} - F' \right) d\eta. \quad (3.94)$$

If we approximate the integral in (3.94) by

$$\int_0^\infty \left( \frac{1}{\rho_0} - F' \right) d\eta \approx \int_0^{\eta_e} \left( \frac{1}{\rho_0} - F' \right) d\eta,$$

we have

$$d^* \simeq d - \sqrt{2\bar{\xi}}F(\eta_e). \quad (3.95)$$

Once the  $d^* = d^*(\bar{\xi})$  is determined we may compute the pressure perturbation in the outer flow due to the displacement thickness. Because the lowest-order outer flow is a uniform flow,  $W_0(\bar{\xi}, 0) = 0$  and it can be shown that  $P_1(\bar{\xi})$  is determined by solving the thin airfoil equation subject to the boundary condition

$$W_1(\bar{\xi}, 0) = \frac{d(d^*)}{d\bar{\xi}} = \frac{d^*}{2\bar{\xi}}.$$

In the remainder of this section, we take the outer flow to be supersonic so that the pressure perturbation is given by

$$P_1(\bar{\xi}, 0) = \frac{1}{\sqrt{M_\infty^2 - 1}} \frac{dd^*}{d\bar{\xi}} \quad (3.96)$$

which yields the well known result that the first-order pressure perturbation decreases as  $\bar{\xi}^{-\frac{1}{2}}$  in a supersonic outer flow.

We now solve the Levy-Lees similarity equations to determine  $F(\eta)$ ,  $F'(\eta)$ ,  $F''(\eta)$ ,  $\theta_0(\eta)$ ,  $\theta'_0(\eta)$ , etc [32]. for the special case of a perfect gas, i.e., an ideal gas with constant specific heats, a Prandtl number = 0.7 = constant, a shear viscosity which is linear in absolute temperature, and a freestream Mach number of  $M_\infty = 2$ . The value of  $\eta_e$  is determined by the condition  $F'(\eta_e) \approx 0.99$ . At a given  $\bar{\xi}$ , the value of  $P_1$  is determined from (3.93)-(3.96). The variation of  $\bar{p}\hat{\Delta}$  at a given  $\bar{\xi}$  is then given by (3.90) once the Reynolds number and the value and variation of  $\bar{\mu}_b$  is chosen. In the following examples, we use a Reynolds number of 30000 and  $\bar{\xi} = 5$ .

For our first example, we consider an adiabatic wall and have plotted  $\bar{p}/\delta P_1$ , vs  $\hat{n}/d$  in Figure 3.2. The quantity  $\bar{p}/\delta P_1$  is the pressure perturbation scaled with that due to the displacement thickness and is unity in the classical  $\bar{\mu}_b = O(1)$  first-order theory. The quantity  $\hat{n}/d$  is recognized as also equal to the dimensional  $n$ -coordinate divided by the dimensional boundary layer thickness. Each

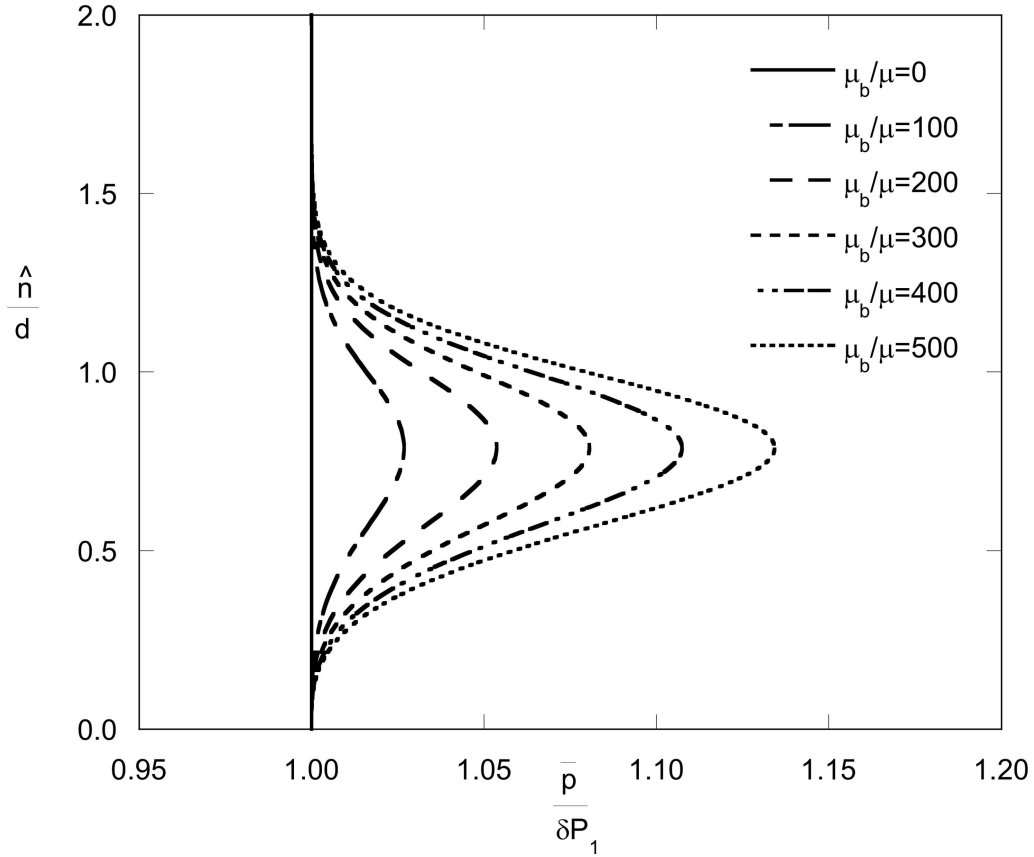


Figure 3.2: Scaled pressure vs. physical distance measured normal to the plate for different values of bulk viscosity to shear viscosity.

curve in Figure 3.2 corresponds to a constant value of  $\bar{\mu}_b$ . Values of  $\bar{\mu}_b$  were taken to be 0, 0.7, 100, 200, 300, 400, 500. Because  $\bar{\mu}_b$  is constant with  $\hat{n}$ , the variation in  $\bar{p}/\delta P_1$  reflects the variation in  $\widehat{\nabla \cdot \mathbf{v}}$ , i.e., the coefficient of  $\delta\bar{\mu}_b$  in (3.90). For the adiabatic plate, the temperature  $\theta_0 = \theta_0(\eta)$  decreases monotonically with increasing  $\eta$  or  $\hat{n}$  and  $\bar{p}/\delta P_1 - 1$  is always positive.

In the simple case of an adiabatic plate, perfect gas, constant Prandtl number, and Chapman-Rubensin parameter equal to unity,

$$F = F(\eta),$$

$$\theta_0 = \theta_0(\eta; Pr, E) = 1 + E\tilde{\theta}_0(\eta; Pr).$$



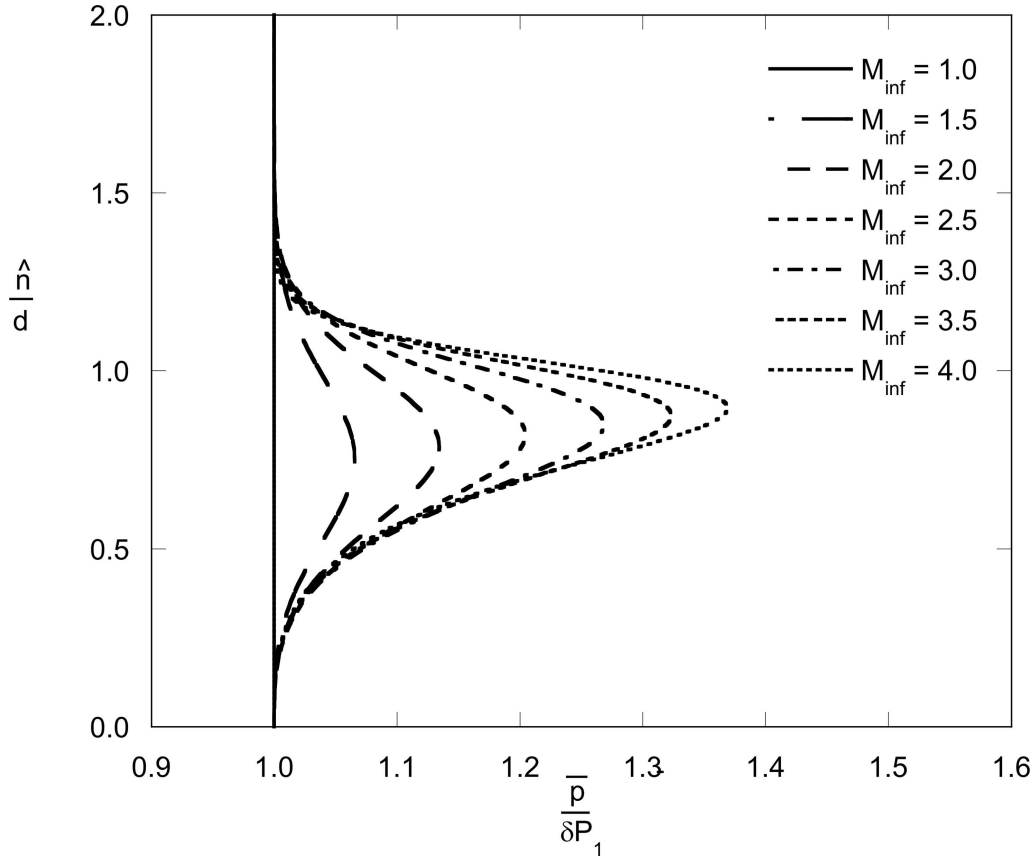


Figure 3.3: Scaled pressure vs. physical distance measured normal to the plate for different values of freestream Mach number for bulk viscosity to shear viscosity ratio = 500.

Thus, the Eckert number  $E = U^2/c_{p\infty}T_\infty = M_\infty^2(\gamma - 1)$  can be scaled out to yield a simplified version of (3.90):

$$\bar{\rho}\hat{\Delta} = -\frac{\delta\bar{\mu}_b}{2\xi}F\frac{E\tilde{\theta}'_0}{1 + E\tilde{\theta}_0}.$$

If we also take  $\bar{\mu}_b = \text{constant}$  the dependence of  $\bar{\rho}\hat{\Delta}$  on Mach number is therefore obtained explicitly. For this simple case,  $\bar{\rho}\hat{\Delta}$  grows roughly linearly with increasing  $M_\infty^2$ , particularly when  $\gamma \approx 1$ . Because  $d, d^*$  and  $P_1$  will vary with  $E$ , there will be a redistribution and further stretching of  $\bar{p}/\delta P_1$  with  $M_\infty^2$ .

For the case of  $\bar{\mu}_b = 500$  we have plotted the variation of  $\bar{p}/\delta P_1$  with  $\hat{n}/d$  for various values of  $M_\infty$  in Figure 3.3.

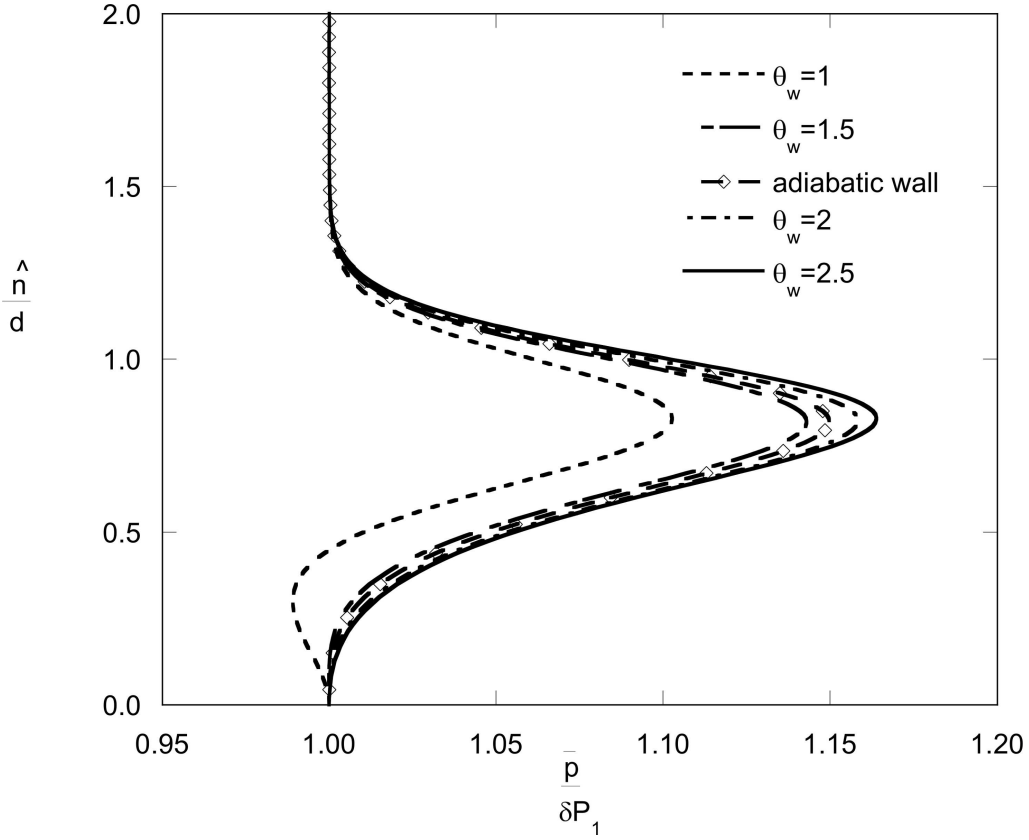


Figure 3.4: Scaled pressure vs. physical distance measured normal to the plate for heated and cooled plates for bulk to shear viscosity ratio=500. Here  $\theta_w$  = wall temperature divided by the freestream temperature.

In Figure 3.4, we have plotted the variation of  $\bar{p}/\delta P_1$  vs.  $\hat{n}/d$  for heated and cooled plates for  $\bar{\mu}_b = 500 = \text{constant}$ . As a reference, the case of an adiabatic plate is also included. In the case of heated walls, i.e., the cases of  $\theta_w = 1.0$  and  $1.5$ ,  $\theta_0$  has a local maximum which, from (3.90), requires that  $\bar{\rho}\hat{\Delta} = 0$  at the local maximum of  $\theta_0$ . Thus,  $\bar{p}/\delta P_1 - 1$  will change sign for heated walls.

As discussed by Cramer [23], the value of  $\mu_b$  can vary significantly with temperature. As a result, the variation of  $\bar{p}/\delta P_1$  will, in general, differ from that predicted by a calculation using constant  $\mu_b$ . To illustrate the differences possible, we consider the case of methane ( $\text{CH}_4$ ). Below 260 K, the primary contribution to the bulk viscosity of  $\text{CH}_4$  is the rotational mode resulting in  $\mu_b = O(\mu)$

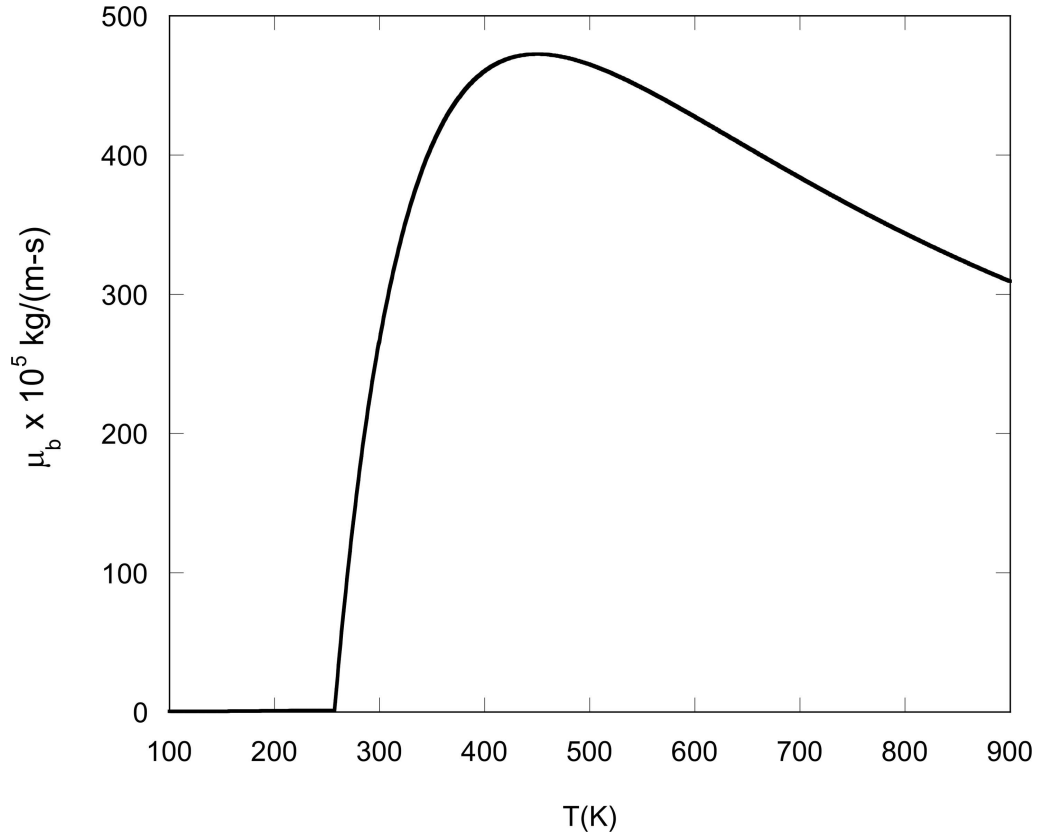


Figure 3.5: Variation of the bulk viscosity of methane with temperature.

and a weak increase in  $\mu_b$  with temperature [23].

At higher temperatures, the vibrational mode is dominant yielding bulk viscosities which are hundreds of times larger than the shear viscosity. The temperature variation of the dimensional bulk viscosity of  $\text{CH}_4$  has been plotted in Figure 3.5. From 100 K to 300 K, the power law fit given by Cramer [23] is used. The rotational contribution is set equal to zero for  $T > 300$  K. Below approximately 260 K, the vibrational mode is deactivated and the vibrational contribution is set equal to zero. Above 260 K the vibrational portion of the bulk viscosity is computed from the Landau-Teller fit given by Equation (30) of Cramer [23] and added to the rotational contribution. At 300 K, there will be a relatively small discontinuity in  $\mu_b$ . However, at 300 K the vibrational contribution is much larger than the rotational contribution and the discontinuity will have no significant impact

on the following plots or discussion. In Figure 3.6, we compare the scaled boundary layer pressure using the variable  $\mu_b$  of Figure 3.5 to that computed with a constant  $\mu_b$ . As in the previous calculations we take the gas to be perfect with  $Pr = 0.7$ , a shear viscosity proportional to temperature and a freestream Mach number of 2. The plate is taken to be adiabatic. The freestream Reynolds number is 30000 and  $\bar{\xi} = 5$ . The ratio of specific heats is computed from the freestream temperature and the data and correlations of Reid, Prausnitz, and Poling (1987). In the cases computed using a constant  $\mu_b$ , the freestream bulk viscosity ( $\mu_{b\infty}$ ) is used. When  $T_\infty = 200$  K,  $\gamma_\infty \equiv 1.4$  and the vibrational mode is not activated in the freestream. As a result,  $\mu_b = O(\mu)$  in the freestream and  $\bar{p}/\delta P_1 \equiv 1$  when a constant  $\mu_b$  is used. However, the wall temperature is approximately 328 K resulting in a layer of large bulk viscosity fluid near the wall.

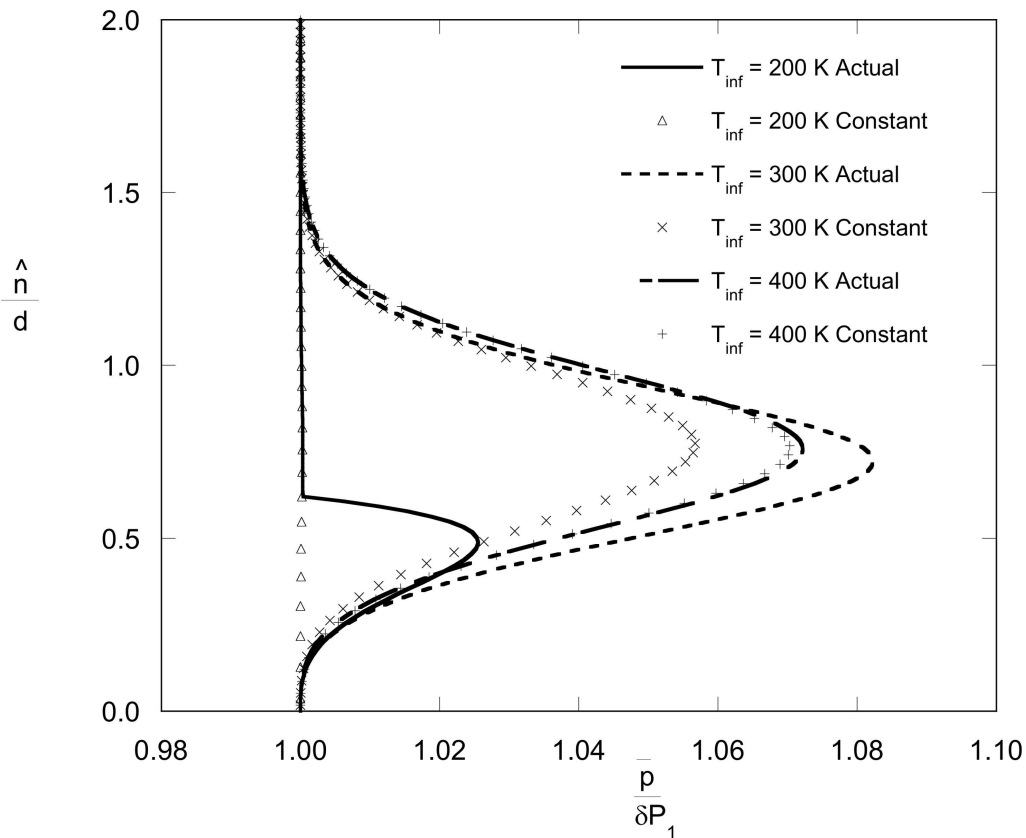


Figure 3.6: Scaled pressure vs. physical distance measured normal to the plate for realistic and constant bulk to shear viscosity of methane.

As seen in Figure 3.6 the computed pressure perturbation deviates significantly from that of the constant  $\mu_b$  case below  $\hat{n} = 0.6d$ . At freestream temperatures of 300 K and 400 K  $\mu_b \gg \mu$  throughout the boundary layer and  $\bar{p}/\delta P_1$  is of the same general size as seen in the previous calculations regardless of whether a variable or constant bulk viscosity is used. When  $T_\infty = 300$  K,  $\gamma_\infty \equiv 1.3$  and the wall temperature is 452 K which is in the neighborhood of the local maximum in  $\mu_b$  seen in Figure 3.5. Thus, the bulk viscosity is always larger than the freestream value and the pressures are noticeably larger than those computed with  $\mu_b = \mu_{b\infty}$ . When  $T_\infty = 400$  K,  $\gamma_\infty \equiv 1.25$  and the wall temperature is approximately 569 K. Inspection of Figure 3.5 reveals that the bulk viscosities in the boundary layer are always near the local maximum of  $\mu_b$ . As a result, there is little difference between the pressures based on constant  $\mu_b$  and those based on variable  $\mu_b$ . When the freestream temperature is larger than approximately 450 K, the bulk viscosity in the boundary layer will always be less than the freestream value. At these temperatures the pressure levels in an actual boundary layer will always be less than those computed with  $\mu_b = \mu_{b\infty}$ .

### 3.7 Conclusion

We have examined the simplest and most obvious effects of large bulk viscosity on three dimensional, steady flow over bodies at large Reynolds numbers. The ratio of bulk to shear viscosity was taken to be (3.8). The method of matched asymptotic expansions was used to develop a first order theory for both the outer and inner flows. With (3.8), the effects of large bulk viscosity on the outer flow are on the order of the perturbations due to the boundary layer displacement thickness. It may be of interest in future studies to examine the effects of large bulk viscosity on stronger, i.e., bilateral, inviscid-viscous coupling. An important result of the matching is that the outer flow still slips at the body surface in spite of the fact that the first order theory is frictional, rotational, and non-isentropic. When (3.8) is imposed the effects of the large bulk viscosity on the boundary layer are on the same order as the effects of three-dimensionality. However, the bulk viscosity effects remain even when the flow is two-dimensional and over a flat plate. The primary effect on the momentum balance is the replacement of the pressure by the pressure minus the viscous normal stress  $\mu_b \nabla \cdot \mathbf{v}$ . As a result the bulk viscosity causes first order variations in the pressure across the boundary layer even for flat plates. The first order energy equation is modified in a more significant way. For ideal gases, the correction to the temperature equation is related to a flux of  $\mu_b \nabla \cdot \mathbf{v}$ . In future studies it would be of interest to examine the effect of this source term on the skin friction when the Chapman-Rubesin parameter is not equal to 1 (resulting in coupling between the energy and momentum boundary layer equations) and the effects on heat transfer. Because we have presented a rigorous and systematic theory of the effects of large bulk viscosity on the classical inviscid approximation, the bulk viscosity effects are restricted to being small corrections on the lowest order classical theory. We nevertheless believe that our results are of value particularly in modern times when aerodynamic theory is mature, highly refined and is frequently concerned with small improvements. This work also provides engineers with guidance for the design of power systems and turbomachinery using fluids other than air and water. Our work and Emanuel's [24]

can also suggest further studies into the effect of large bulk viscosity on stronger inviscid-viscous interactions, e.g., separation, or hypersonic flows, e.g., the entropy and vorticity layers found in very high speed flows.

# Chapter 4

## Shock-Boundary Layer Interaction for Large Bulk Viscosity Fluids

### 4.1 Introduction and Motivation

Flow separation leads to loss and vibration in turbomachinery and causes increase in energy use and higher maintenance cost. The cause of separation is the adverse pressure gradients, i.e., pressure increase in flow separation. In turbomachinery and aeronautical applications shock waves are a source of indefinitely strong adverse pressure gradients. A diagram of shock boundary layer separation is sketched in Figure 4.1. The incoming shock imposes an adverse pressure gradient which generates a back flow in the near wall regions forming a vortex "bubble" as sketched in Figure 4.1. The separation and reattachment points are sketched in Figure 4.1. Because boundary layer thickness increases a weak compression shock is generated upstream of separation which is referred to as the separation shock. At the reattachment point, a reattachment shock forms as sketched in Figure 4.1. The incoming shock reflects as an expansion. Due to the fact that shocks are normally regarded as being infinitely thin, shock waves are a good model for the study of any abrupt



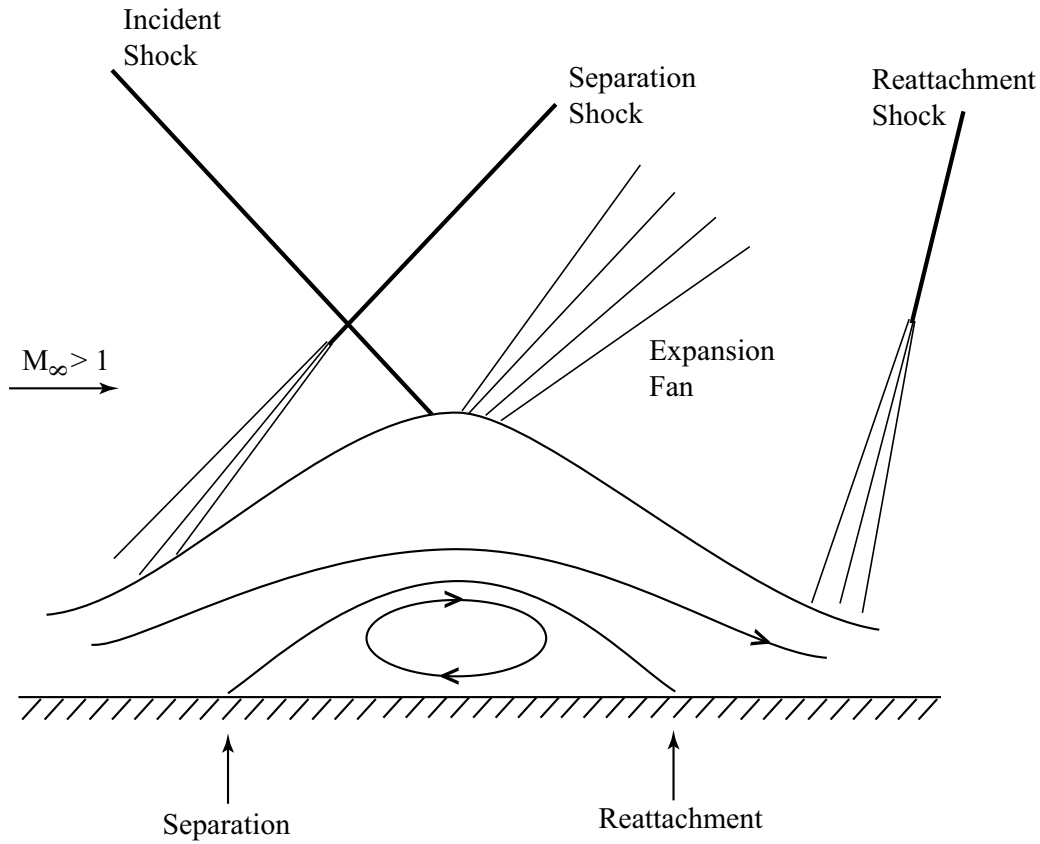


Figure 4.1: Shock-boundary layer interaction.

change imposed on boundary layers. The purpose of this part of thesis is to examine the effect of large bulk viscosity on shock-induced separation. Studies of shock boundary layer interaction have been carried out by experimental, numerical and analytical means. The best known theory for shock-induced separation is the triple deck theory where the viscous-inviscid interaction zone is found to be divided into three layers.

According to the results of Katzer [33] and Kluwick [34] the criterion for separation can be written as

$$\frac{c_{pT}(M_1^2 - 1)^{\frac{1}{4}}}{\sqrt{c_f|_s}} > K_s \quad (4.1)$$

where  $c_{pT}$ ,  $M_1$  and  $c_f|_s$  are the pressure coefficient for the total pressure rise, the flow Mach number and the skin friction coefficient before the interaction zone respectively and the value of

$K_s \approx 2.6$  from Katzer's calculations. According to other references  $K_s$  generally varies between 2 and 3. Thus, separation will depend on the upstream Mach number, the strength of the incoming shock (through  $c_{pT}$ ) and the  $Re$  at the shock impingement point. Here we consider the effect of large  $\mu_b/\mu$ . This is a fourth parameter which we can regard as an independent parameter. The thickness of the incoming shock is expected to be dependent on the bulk viscosity as follows

$$= O\left(\frac{\mu_b}{\mu} \frac{L}{Re} \frac{1}{\epsilon}\right); \quad (4.2)$$

see [22]. The quantity  $Re = \frac{U\rho_\infty L}{\mu} \gg 1$  is just the Reynolds number based on the freestream velocity  $U$ , the freestream density  $\rho_\infty$ , and  $L$  is a macroscopic length scale. As the bulk viscosity increases, the shock will thicken. According to the triple deck theory the length of the interaction zone is of order  $LRe^{-\frac{3}{8}}$ . Thus, the incoming shock will no longer appear as a discontinuity when the shock thickness is of the same size as the interaction zone, i.e., when

$$\frac{\mu_b}{\mu} \frac{1}{Re} \frac{1}{\epsilon} = O(Re^{-\frac{3}{8}}) \quad (4.3)$$

where  $\epsilon =$  a non-dimensional measure of the shock strength, e.g.,  $\frac{\Delta p}{p_\infty}$ , where  $\Delta p$  is the pressure jump across the shock and  $p_\infty$  is the freestream pressure. The triple deck theory also requires that the disturbance carried by the shock  $\epsilon = O(Re^{-\frac{1}{4}})$ . The shock will no longer appear to be thin relative to the interaction zone when

$$\frac{\mu_b}{\mu} = O(Re^{\frac{3}{8}}) \gg 1. \quad (4.4)$$

Thus, when (4.4) holds we expect that the results of Katzer [33] and Kluwick [34] will break down. Because the incoming shock is no longer thin compared to the length of the interaction zone it is reasonable to conjecture that the shock thickening will lead to a decrease and perhaps full suppression of separation. The main goal of this part of the thesis is to demonstrate that this is

the case.

In Section 4.2, we discuss the condition of local thermodynamic equilibrium (LTE). It is shown that in case of large bulk viscosity fluids, the fluid is in equilibrium throughout the interaction zone. The equations, boundary conditions, assumptions and flow parameters are provided in Section 4.3. In Section 4.3.1 we introduce the numerical scheme used to solve the equations and in Section 4.3.2 we discuss the validation of the code by comparison of the exact and numerical solutions of reflection of an oblique shock wave from a flat plate based on the inviscid theory. We also compare the boundary layer similarity and (Navier-Stokes) numerical solutions for a pure boundary layer flow. Finally, we compare our numerical solutions with previous studies of shock boundary layer interaction. In Section 4.4 the result of interest which is that separation can be reduced and suppressed when fluids with relatively large bulk viscosity are used.

## 4.2 Local Thermodynamic Equilibrium (LTE)

When working with large bulk viscosity fluids, it is always advisable to check whether the condition of local thermodynamic equilibrium (LTE) is satisfied; see, e.g., the discussion of Section 3.1. We begin by considering the expression for the thickness of a shock from (4.2) which can be simplified to

$$\frac{L}{Re} \frac{\mu_b}{\mu} \frac{1}{\epsilon} = O\left(\frac{\mu_b}{\epsilon U \rho_\infty}\right) \quad (4.5)$$

Here we take the shock strength to be small so that  $\epsilon \ll 1$ . If we recognize that  $\mu_b = O(p_\infty \tau_i)$  [30], [22] and [24], where  $\tau_i$  is the relaxation time for the internal energy modes; see, e.g., (2.3), then the time a fluid particle spends in the shock is

$$\frac{\mu_b}{U^2} \frac{1}{\epsilon \rho_\infty} = O\left(\frac{p_\infty}{\rho_\infty U^2} \frac{\tau_i}{\epsilon}\right) = O\left(\frac{\tau_i}{\epsilon}\right) \gg \tau_i, \quad (4.6)$$

where we have taken  $\frac{p_\infty}{\rho_\infty} = O(a_\infty^2)$  and the Mach number  $= \frac{U}{a_\infty} = O(1)$ . Here  $a_\infty$  is the sound speed evaluated in the freestream. Thus, the fluid will be in local equilibrium at every point in the shock, even if  $\mu_b \gg \mu \iff \tau_i \gg \tau_c \equiv$  the molecular collision time. As discussed in the introduction we will take the shock thickness to be the same order of magnitude as the shock-boundary layer interaction zone. Thus, the fluid will also be in equilibrium throughout the interaction zone and we conclude that LTE is satisfied in all that follows.

### 4.3 Formulation

In this part of the dissertation we take the flow to be steady two-dimensional and governed by the Navier-Stokes equation given in Appendix A. The flow will be supersonic and over a flat, adiabatic plate. We introduce an oblique shock wave at the inflow boundary condition. This shock strikes the plate at a point  $x = L_s$  from the leading edge of the plate. This impingement point is computed from conventional inviscid oblique shock theory. The configuration is sketched in Figure 4.2.

The fluid model is that of a perfect gas, i.e., the equation of state is taken to be

$$p = \rho RT, \quad (4.7)$$

and the specific heats are taken to be constants. Here  $R$  is the gas constant. The shear viscosity is taken to be proportional to the absolute temperature and the Prandtl number ( $Pr$ ) is taken to be a constant so that the thermal conductivity is given by

$$k = (\mu c_p)/Pr, \quad (4.8)$$

where  $c_p \equiv$  the specific heat at constant pressure. The ratio of bulk to shear viscosity is taken to be

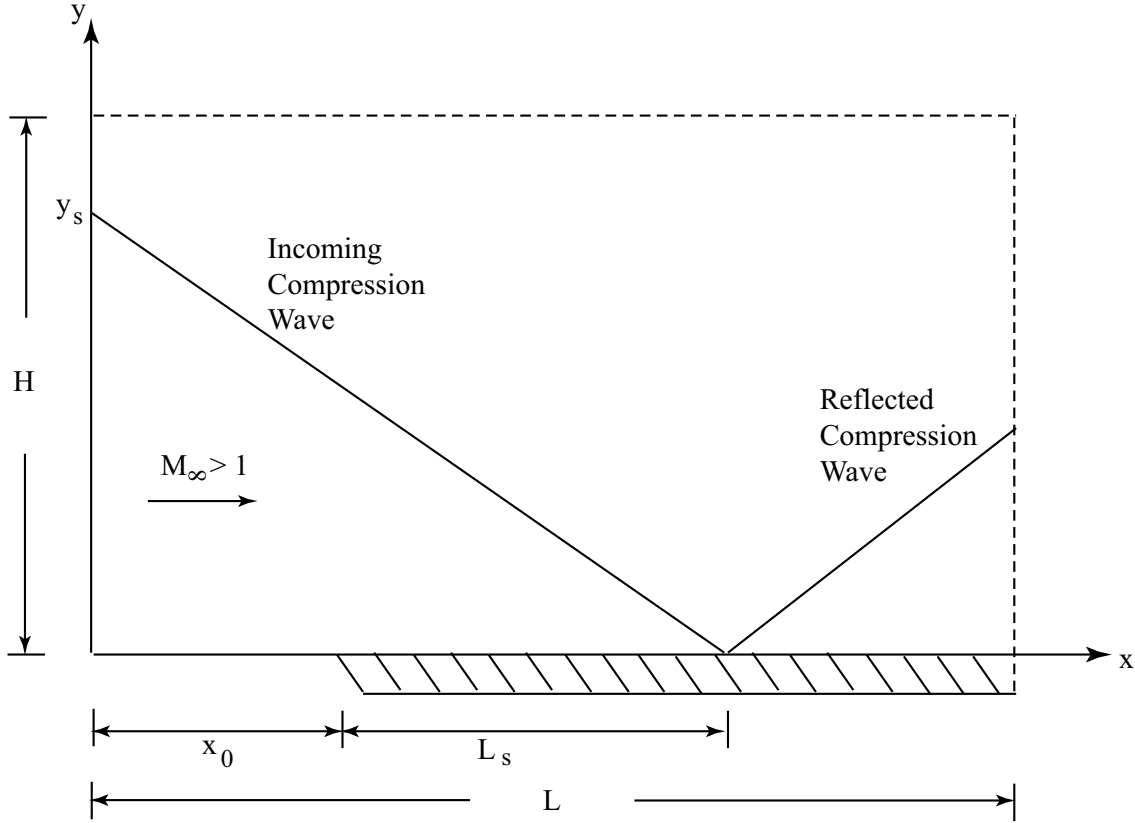


Figure 4.2: Sketch of the computational domain.

constant, i.e.,  $\mu_b/\mu = \text{constant}$  and the second viscosity is therefore given by

$$\frac{\lambda}{\mu} = \frac{\mu_b}{\mu} - \frac{2}{3} = \text{constant.} \quad (4.9)$$

The chosen values of  $\gamma = c_p/c_v$ ,  $\mu_b/\mu$ ,  $Pr$ , etc will be taken to be those of freestream. To solve the Navier-Stokes equation for the steady flow numerically we will solve the unsteady equations seeking the steady state asymptote. To resolve the details of the interaction zone we will employ a coordinate system which is stretched in the direction normal to the plate, i.e., the  $y$ -direction in Figure 4.2. The mapping used for the stretching is given by

$$\xi \equiv \frac{x}{L}, \quad \eta \equiv f\left(\frac{y}{H}; \beta\right) \equiv 1 - \ln\left(\frac{\beta + 1 - y/H}{\beta - 1 + y/H}\right) / \ln\left(\frac{\beta + 1}{\beta - 1}\right) \quad (4.10)$$

where  $H$  is the value of  $y$  at the upper computational boundary and  $\beta$  is the stretching parameter having values in the range  $1 < \beta < \infty$ . Mapping yields  $\eta = 1$  at  $y = H$  and  $\eta = 0$  at  $y = 0$ . As  $\beta \rightarrow \infty$  we obtain a uniform grid, i.e.,

$$\eta \rightarrow \frac{y}{H}.$$

It is easily verified that the metric of the  $z^i \equiv (\frac{x}{L}, \frac{y}{H}, z) \leftrightarrow x^i \equiv (\xi, \eta, z)$  mapping is

$$\begin{pmatrix} 1 & 0 & 0 \\ 0 & \dot{f}^{-2} & 0 \\ 0 & 0 & 1 \end{pmatrix} \quad (4.11)$$

where

$$\dot{f} \equiv \frac{df}{d(y/H)} \quad (4.12)$$

Thus, our coordinate transform is orthogonal and

$$\sqrt{g} \equiv \frac{1}{\dot{f}} \quad (4.13)$$

where  $g$  is the determinant of the metric (4.11). In many texts on computational fluid dynamics,  $\sqrt{g}$  is the inverse of the Jacobian. We now write the two-dimensional form of Navier-Stokes equations in a conservative form and transform these equations using (4.10) to obtain:

$$\frac{\partial \mathbf{Q}}{\partial t} + \frac{\partial \mathbf{F}}{\partial x} + \frac{\partial \mathbf{G}}{\partial y} = \frac{\partial \mathbf{F}^{(v)}}{\partial x} + \frac{\partial \mathbf{G}^{(v)}}{\partial y} \quad (4.14)$$

where

$$\mathbf{Q} = \left\{ \begin{array}{c} \sqrt{g}\bar{\rho} \\ \sqrt{g}\bar{\rho}\bar{u} \\ \sqrt{g}\bar{\rho}\bar{v} \\ \sqrt{g}\bar{\rho}(\bar{e} + \frac{\bar{u}^2 + \bar{v}^2}{2}) \end{array} \right\}, \quad (4.15)$$

$$\mathbf{F} = \left\{ \begin{array}{c} \sqrt{g}\bar{\rho}\bar{u} \\ \sqrt{g}(\bar{p} + \bar{\rho}\bar{u}^2) \\ \sqrt{g}\bar{\rho}\bar{u}\bar{v} \\ \sqrt{g}\bar{\rho}\bar{u}(\bar{e} + \frac{\bar{p}}{\bar{\rho}} + \frac{\bar{u}^2 + \bar{v}^2}{2}) \end{array} \right\}, \quad (4.16)$$

$$\mathbf{G} = \left\{ \begin{array}{c} \sqrt{g}\dot{f}\bar{\rho}\bar{v} \\ \sqrt{g}\dot{f}\bar{\rho}\bar{u}\bar{v} \\ \sqrt{g}\dot{f}(\bar{p} + \bar{\rho}\bar{v}^2) \\ \sqrt{g}\dot{f}\bar{\rho}\bar{v}(\bar{e} + \frac{\bar{p}}{\bar{\rho}} + \frac{\bar{u}^2 + \bar{v}^2}{2}) \end{array} \right\} \quad (4.17)$$

$$\mathbf{F}^{(v)} = \left\{ \begin{array}{c} 0 \\ \frac{\sqrt{g}}{Re_s}\bar{\tau}_{11} \\ \frac{\sqrt{g}}{Re_s}\bar{\tau}_{12} \\ \frac{\sqrt{g}}{Re_s}(\bar{W}_1 - q_1) \end{array} \right\}, \quad (4.18)$$

$$\mathbf{G}^{(v)} = \left\{ \begin{array}{c} 0 \\ \frac{\sqrt{g}}{Re_s}\bar{\tau}_{21} \\ \frac{\sqrt{g}}{Re_s}\bar{\tau}_{22} \\ \frac{\sqrt{g}}{Re_s}(\bar{W}_2 - q_2) \end{array} \right\} \quad (4.19)$$

where  $\mathbf{Q}$  represents the 4-vector density and  $\mathbf{F}$ ,  $\mathbf{G}$ ,  $\mathbf{F}^{(v)}$ ,  $\mathbf{G}^{(v)}$  are the 4-vectors representing the inviscid and viscous fluxes of the system. The overbars denote nondimensional quantities defined

by:

$$(\bar{x}, \bar{y}) \equiv (x, y)/L_s \quad (4.20)$$

$$\bar{t} \equiv t/(L_s/a_\infty) \quad (4.21)$$

$$\bar{\rho} \equiv \rho/\rho_\infty \quad (4.22)$$

$$\bar{p} \equiv p/\rho_\infty a_\infty^2 \quad (4.23)$$

$$\bar{e} \equiv e/a_\infty^2 \quad (4.24)$$

$$\bar{T} \equiv T/T_\infty \quad (4.25)$$

$$(\bar{u}, \bar{v}) \equiv (u, v)/a_\infty \quad (4.26)$$

$$\bar{\tau}_{ij} \equiv \frac{L_s}{\mu_\infty a_\infty} \tau_{ij} \quad (4.27)$$

The components of the nondimensional power of the viscous stresses  $\overline{W_i^*}$  are related to the dimensional quantities  $\overline{W_i^*} \equiv \tau_{ij} v_j$  by

$$\overline{W_i^*} \equiv \frac{L_s}{\mu_\infty a_\infty^2} W_i^* \quad (4.28)$$

and the components of the nondimensional heat flux vector  $(\bar{q}_i)$  are related to the dimensional quantities  $q_i$  by

$$\bar{q}_i \equiv \frac{L_s}{k_\infty T_\infty} q_i, \quad (4.29)$$

In (4.20)-(4.29), the subscripts  $\infty$  denote quantities evaluated at the freestream. The quantity

$$Re_\infty = \frac{a_\infty L_s \rho_\infty}{\mu_\infty} \quad (4.30)$$



is the Reynolds number based on  $L_s$  and the freestream sound speed. The quantities

$$\overline{W_i^* - q_i} \equiv \overline{W_i^*} - \frac{1}{PrEc} \bar{q}_i \quad (4.31)$$

where

$$Ec \equiv \frac{a_\infty^2}{c_p T_\infty} \quad (4.32)$$

which is recognized as an Eckert number based on the sound speed. The constitutive relations discussed in Appendix A can be used to show

$$\bar{q}_1 = -\bar{k} \frac{\partial \bar{T}}{\partial \xi}, \quad (4.33)$$

$$\bar{q}_2 = -\frac{\bar{k}}{\sqrt{g}} \frac{\partial \bar{T}}{\partial \eta}, \quad (4.34)$$

$$\bar{\tau}_{11} = (\bar{\lambda} + 2\bar{\mu}) \frac{\partial \bar{u}}{\partial \xi} + \frac{\bar{\lambda}}{\sqrt{g}} \frac{\partial \bar{v}}{\partial \eta}, \quad (4.35)$$

$$\bar{\tau}_{22} = \bar{\lambda} \frac{\partial \bar{u}}{\partial \xi} + \frac{(\bar{\lambda} + 2\bar{\mu})}{\sqrt{g}} \frac{\partial \bar{v}}{\partial \eta}, \quad (4.36)$$

$$\bar{\tau}_{12} = \bar{\tau}_{21} = \bar{\mu} \left( \frac{\partial \bar{v}}{\partial \xi} + \frac{1}{\sqrt{g}} \frac{\partial \bar{u}}{\partial \eta} \right), \quad (4.37)$$

where

$$\bar{\mu} = \frac{\mu}{\mu_\infty}, \quad (4.38)$$

$$\bar{\lambda} = \frac{\lambda}{\mu_\infty} = \frac{\mu_b}{\mu_\infty} - \frac{2}{3} \bar{\mu} = \bar{\mu} \left( \frac{\mu_b}{\mu} - \frac{2}{3} \right), \quad (4.39)$$

$$\bar{k} = \frac{k}{k_\infty}. \quad (4.40)$$

We note that (4.12) can be used to render (4.17) independent of  $\sqrt{g}$  and  $\dot{f}$ . The quantities  $\overline{W_1^*}$  now become

$$\overline{W_1^*} = \bar{\tau}_{11}\bar{u} + \bar{\tau}_{12}\bar{v} \quad (4.41)$$

$$\overline{W_2^*} = \bar{\tau}_{21}\bar{u} + \bar{\tau}_{22}\bar{v} \quad (4.42)$$

The plate is located at  $y = 0$  and the plate leading edge is located at  $x = x_0$ . The inflow condition is the free stream supersonic flow. The shock enters the domain through the left-most boundary. The flow variables ahead and behind the shock have been computed and imposed for the inflow condition. At the outflow and top boundaries, the zero gradient condition has been used for flow variables. The physical boundary conditions at the adiabatic plate are

$$\bar{u} = \bar{v} = 0, \quad \frac{\partial \bar{T}}{\partial \bar{\eta}} = 0 \quad (4.43)$$

at the plate. Here we follow conventional practice in computational fluid mechanics and take

$$\frac{\partial \bar{p}}{\partial \bar{\eta}} = 0 \quad (4.44)$$

at the plate. In order to impose the inflow boundary condition, the flow parameters behind the shock wave is set according to the free stream values. The quantities above the shock wave is set according to the post shock conditions, but at the shock, specific treatment is required to get a shock of uniform thickness entering the domain at the inflow. The incoming flow is taken to contain the oblique shock. Ordinarily, the shock is modeled as a discontinuity. The shock then smears due to fluid viscosity and heat conduction. In the case of moderate or zero bulk viscosity, the final

thickness is attained in a relatively short distance. However, when a large bulk viscosity fluid is used, the thickness of the shock is considerably larger than that of a shock in a moderate or small bulk viscosity fluid; see, e.g., Section (4.2). The distance required to attain the final thickness can also be relatively larger for fluids with large bulk viscosity. The required computational domain to attain a mature shock wave can be quite large and can result in prohibitively large computational times. We therefore introduce the oblique shock by using a smooth transition corresponding to the Taylor shock structure. In terms of nondimensional variables, the resultant Taylor structure is found to be

$$\bar{p} = \bar{p}_1 + \frac{\bar{p}_2 - \bar{p}_1}{2} \left[ 1 + \tanh\left(\frac{2(\bar{\eta} + \bar{\eta}_0)}{\Delta\bar{y}}\right) \right] \quad (4.45)$$

$$\bar{\rho} = 1 + \frac{\bar{\rho}_2 - 1}{2} \left[ 1 + \tanh\left(\frac{2(\bar{\eta} + \bar{\eta}_0)}{\Delta\bar{y}}\right) \right] \quad (4.46)$$

$$\bar{u} = M_\infty + \frac{\bar{u}_2 - M_\infty}{2} \left[ 1 + \tanh\left(\frac{2(\bar{\eta} + \bar{\eta}_0)}{\Delta\bar{y}}\right) \right] \quad (4.47)$$

$$\bar{v} = \frac{\bar{v}_2}{2} \left[ 1 + \tanh\left(\frac{2(\bar{\eta} + \bar{\eta}_0)}{\Delta\bar{y}}\right) \right] \quad (4.48)$$

$$\Delta\bar{y} = \frac{4}{Re} \frac{\delta}{\hat{\Gamma}_\infty} \frac{1}{|\theta_2|} \quad (4.49)$$

where  $\hat{\Gamma}_\infty = 1 + \frac{\rho_\infty}{a_\infty} \frac{\partial a}{\partial \rho} \Big|_s$  is the fundamental derivative of gas dynamics which is equal to  $\frac{\gamma_\infty + 1}{2}$  for perfect gases. The quantity

$$\delta \equiv \frac{\mu_b}{\mu} \Big|_\infty + \frac{4}{3} + \frac{\gamma_\infty - 1}{Pr_\infty} \quad (4.50)$$

where  $Pr_\infty$  is the free stream Prandtl number and

$$\bar{\eta} + \bar{\eta}_0 \equiv \bar{y} + [\tan|\sigma_i|](\bar{x} - \bar{x}_s) \quad (4.51)$$

with  $|\sigma_i| \equiv$  the exact shock angle for incident shock from the oblique shock tables and  $\bar{x}_s$  is the position where shock hits the plate.

### 4.3.1 Numerical Schemes

In this section we describe the numerical scheme to be employed and the implementation of the numerical boundary conditions.

For the inflow boundary condition other than the shock location where the Taylor shock structure is used, the boundary conditions for the points behind and ahead of the shock are computed from the oblique shock tables and imposed for  $u$  and  $v$  components of velocity, pressure and density. At the outflow and top boundaries zero gradient for velocity components, pressure and density is imposed. Upstream of the plate the symmetry boundary conditions are imposed for  $u$ ,  $p$  and  $\rho$  and the anti-symmetry is imposed for  $v$ . At the plate in order to impose the no slip boundary condition anti-symmetry is imposed for  $u$  and  $v$ . The spatial discretization is done by a fifth order weighted essentially non-oscillatory (WENO) scheme and the temporal discretization is done using third order Runge Kutta scheme. The WENO scheme avoids spurious oscillations near shocks, the so called Gibbs phenomena. This scheme is uniformly high order accurate and resolves the non-linear shocks with sharp but monotone transitions. This scheme is non-smearing near discontinuities, suitable for our purpose to eliminate the numerical smearing to be able to study the pure effect of bulk viscosity on shock thickening. WENO scheme is an improvement to the essentially non-oscillatory scheme (ENO) which was first introduced by Harten et al. [35], Shu and Osher [36], [37]. The finite volume form of ENO was developed by Harten which was the generalization of total variation diminishing (TVD) schemes. Then Shu and osher built the finite difference form of ENO which was easier and more efficient to implement. The first WENO scheme was suggested by Liu et al [38] and further improved by Jiang and Shu [39]. The ENO is a high order accurate scheme which approximates the fluxes at cell boundaries by choosing the smoothest stencil from all the possible candidates and avoids the spurious oscillations near shocks and discontinuities. For problems involving shock waves, second order schemes work well, however when both shock waves and fine structures are involved, like shock entropy wave interaction, application of WENO

scheme helps to save the computational cost, (CPU time and memory usage). WENO scheme uses a convex combination of all possible stencils assigning a weight to each stencil to determine the contribution of each stencil. The weights are chosen based on the relative smoothness of the stencil compared to other stencils. The WENO scheme uses ENO near discontinuities and high order centered schemes in smooth regions, [39], [40]. In order to implement WENO scheme, local characteristic decomposition of waves must be carried out. First the fluxes are separated into characteristic wave families, then split using flux splitting schemes and then the fluxes at cell boundaries are computed using WENO scheme.

### 4.3.2 Validations

The inviscid part of the code has been validated by comparison of the exact and numerical solutions for the reflection of an oblique shock from a flat plate. The freestream Mach number is taken to be 2 and the incident shock angle is equal to  $32.6^\circ$ . A grid of  $240 \times 240$  points is used for a domain of size 12 by 12. The pressure profiles of the exact and numerical solutions have been plotted in Figure 4.3 at a distance half way between the flat plate and the shock entrance into the domain. The agreement between the exact oblique theory and our numerical scheme is seen to be excellent. The viscous numerical solver has been validated by comparing the result of a boundary layer similarity solution to our shock-free numerical solution. The local Reynolds number is assumed to be  $1.5 \times 10^5$  the Mach number is assumed to be 2 and the Prandtl number is 0.7. A grid of  $480 \times 320$  points is used for a domain of size 12 by 8. The u-velocity and temperature profiles from exact and numerical solutions are plotted in Figures 4.4 and 4.5 and are seen to be in very good agreement. There are about 30 points in the boundary layer which matches previous studies of pure boundary layer numerical solutions.

The numerical solver has also been validated by comparison with previous studies which used the

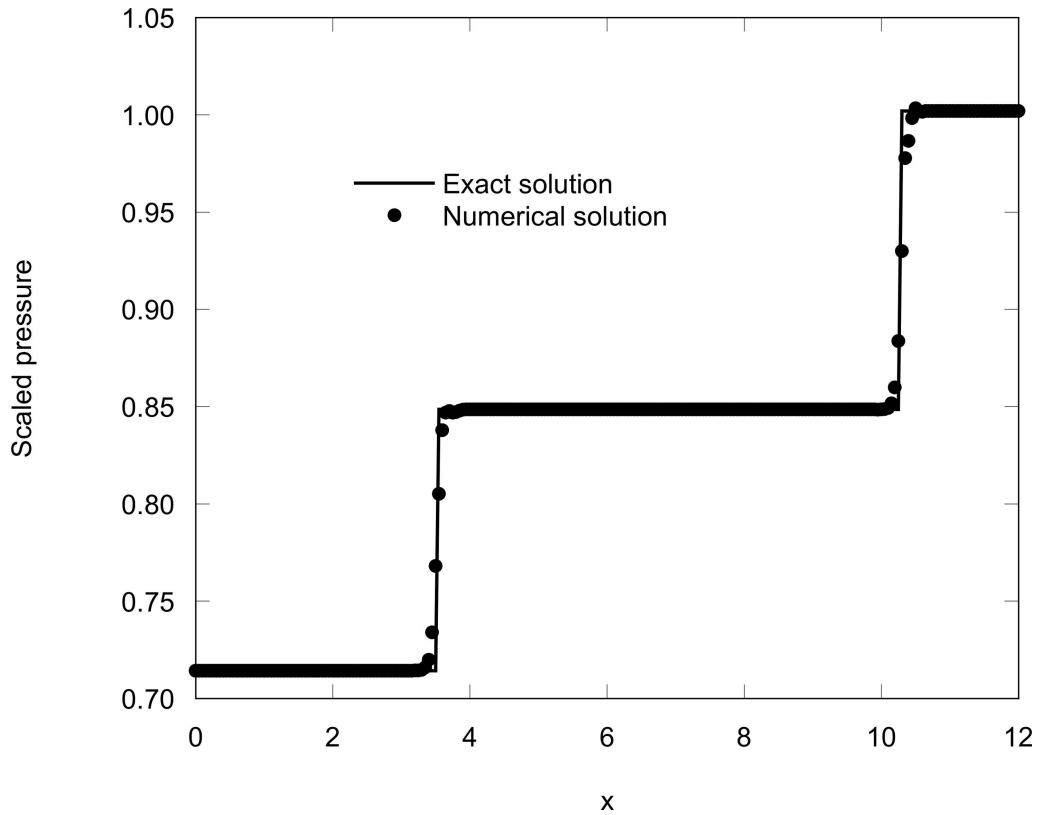


Figure 4.3: Comparison of pressure profiles of the exact and numerical solutions for an oblique shock regular reflection.

Navier-Stokes equations to compute the shock boundary layer interaction. The Reynolds number for this comparison is taken to be  $2.96 \times 10^5$ , Mach number is taken to be 2, the Prandtl number is 0.7, the ratio of bulk to shear viscosity  $\mu_b/\mu$  is equal to 0.7 and the ratio of specific heats  $\gamma$  is equal to 1.4. The incident shock angle is equal to  $32.6^\circ$ . A grid of  $480 \times 320$  points is used for a domain of size 12 by 8. Our computations have been compared to the results from MacCormack [41], Zhong [42], Walters [43], Park [43] and the experimental results from Hakkinen [44]. As shown in Figure 4.6 the result of the present study is in very good agreement with previous studies and is well within the scatter of the different calculations. With this and our unreported comparisons to pure boundary layers and the inviscid oblique shock solutions, we believe that the numerical code is validated.

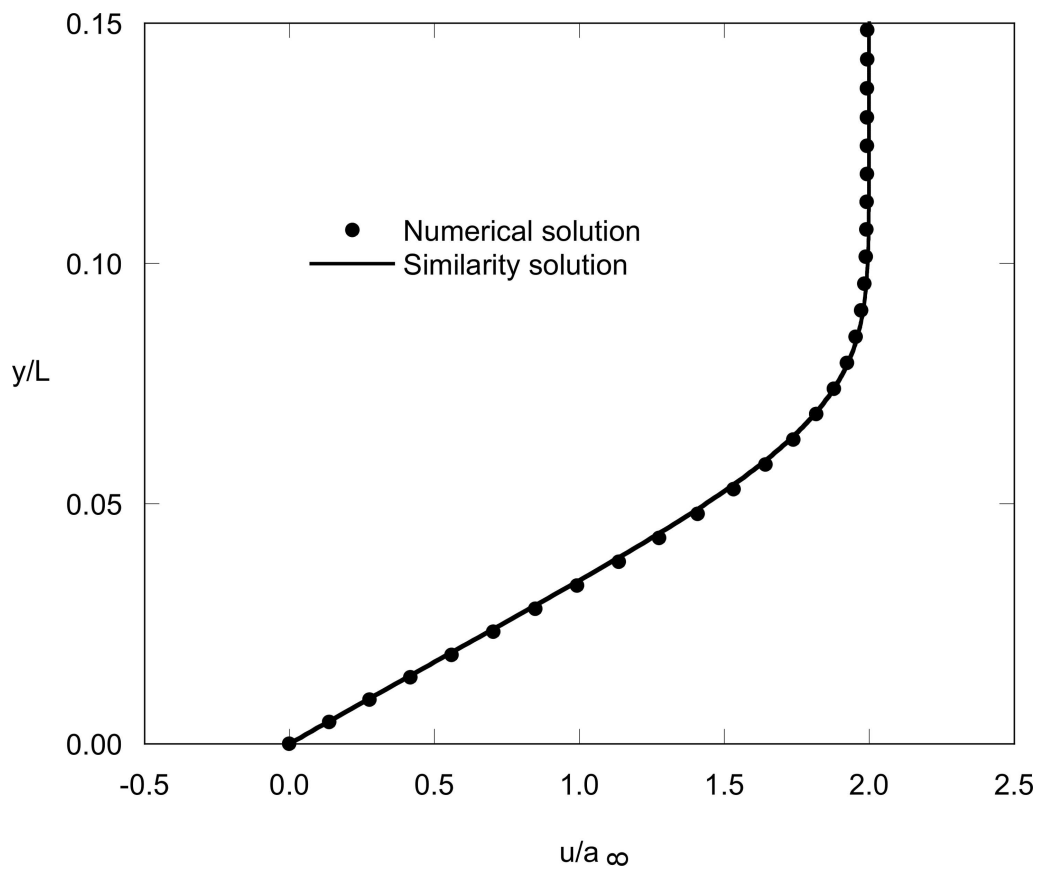


Figure 4.4: Comparison of velocity profiles of the similarity and numerical solutions for flat plate boundary layer.

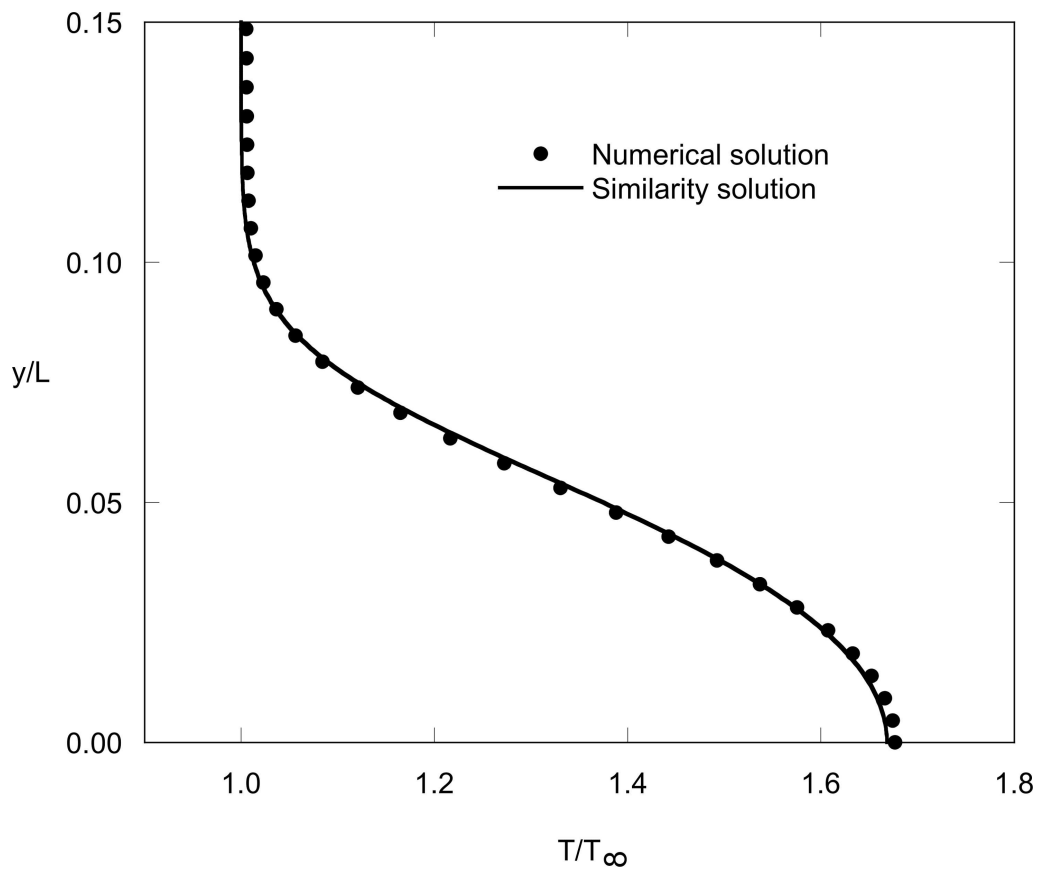


Figure 4.5: Comparison of temperature profiles of the similarity and numerical solutions for flat plate boundary layer.



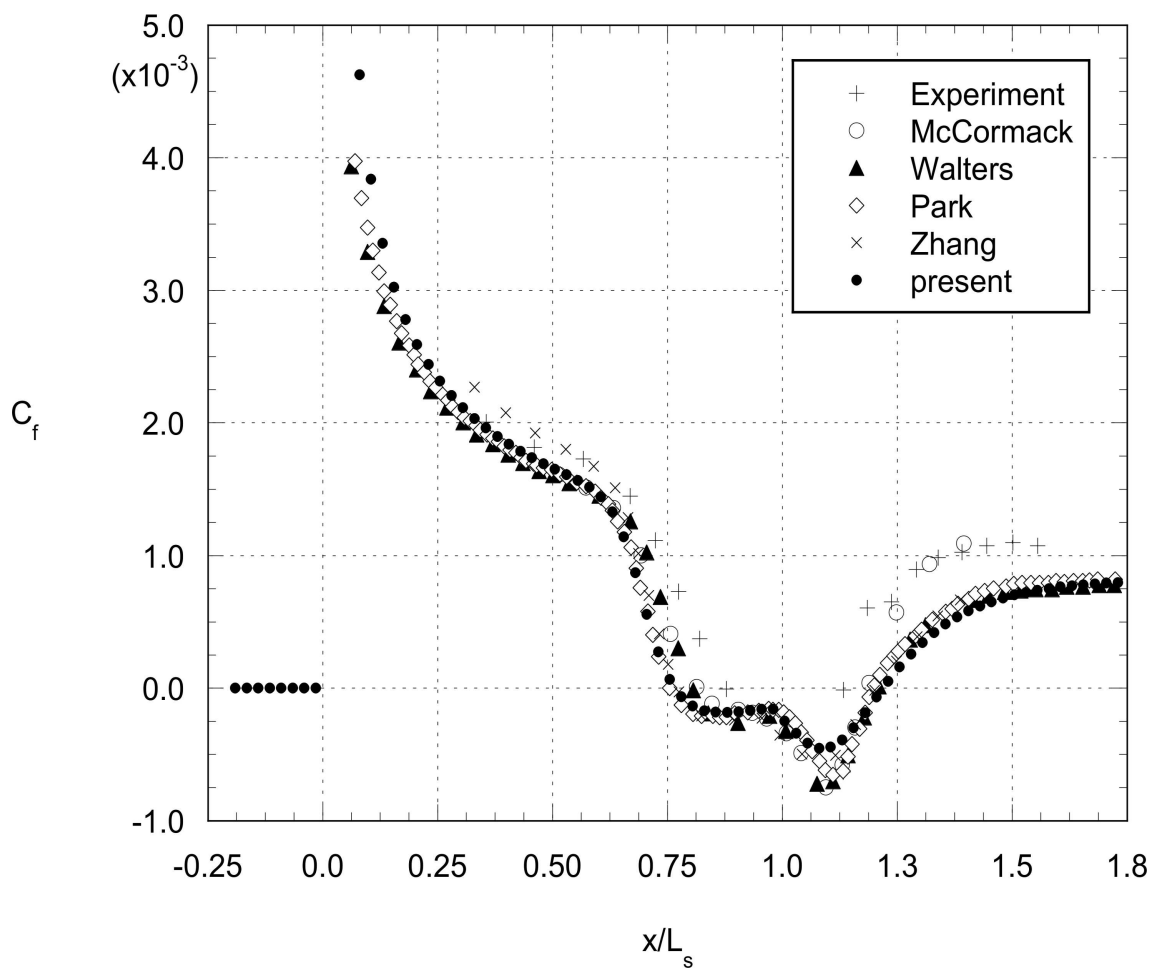


Figure 4.6: Comparison of the results of the present scheme with previous computations.

## 4.4 Results

In the following we take the Reynolds number to be  $2.96 \times 10^5$ , the Mach number to be 2 and the Prandtl number to be 0.7. The fluid is a perfect gas with a ratio of specific heats equal to 1.4. The flow deflection angle of the incident shock wave is taken to be  $2.5^\circ$ . A grid of  $480 \times 320$  points is used for a domain of size 12 by 8. The ratio of bulk viscosity to shear viscosity have the values  $\mu_b/\mu = 0.7, 200, 400, 600, 800$ . The value of  $\mu_b = 0.7\mu$  corresponds to the bulk viscosity of air at  $300^\circ K$ . The skin friction coefficient

$$c_f = \frac{\tau_w}{\frac{1}{2}\rho_\infty U^2} \quad (4.52)$$

where  $\tau_w \equiv$  the shear stress at the wall, has been plotted as a function of  $\bar{x}$  in Figure 4.7. Flow separation, i.e., flow reversal, is indicated by negative values of the skin friction. When the bulk viscosity is 0.7, the flow is clearly separated with finite length separation zone. As the bulk viscosity is increased the separation zone decreases and the minimum value of the skin friction increases. Between  $\mu_b/\mu = 400$  and 600, the separation zone vanishes and the minimum value of the skin friction becomes positive. Thus, we conclude that separation can be suppressed once the bulk viscosity is large enough. The contours of scaled pressure for classical and large bulk viscosity fluids are plotted in Figures 4.8 and 4.9. The value of  $\mu_b/\mu =$  is equal to 0.7 and 800 respectively. As seen from Figure 4.9 shock thickness increases and the adverse pressure gradient reduces for large bulk viscosity case which ultimately will result in the suppression of separation.

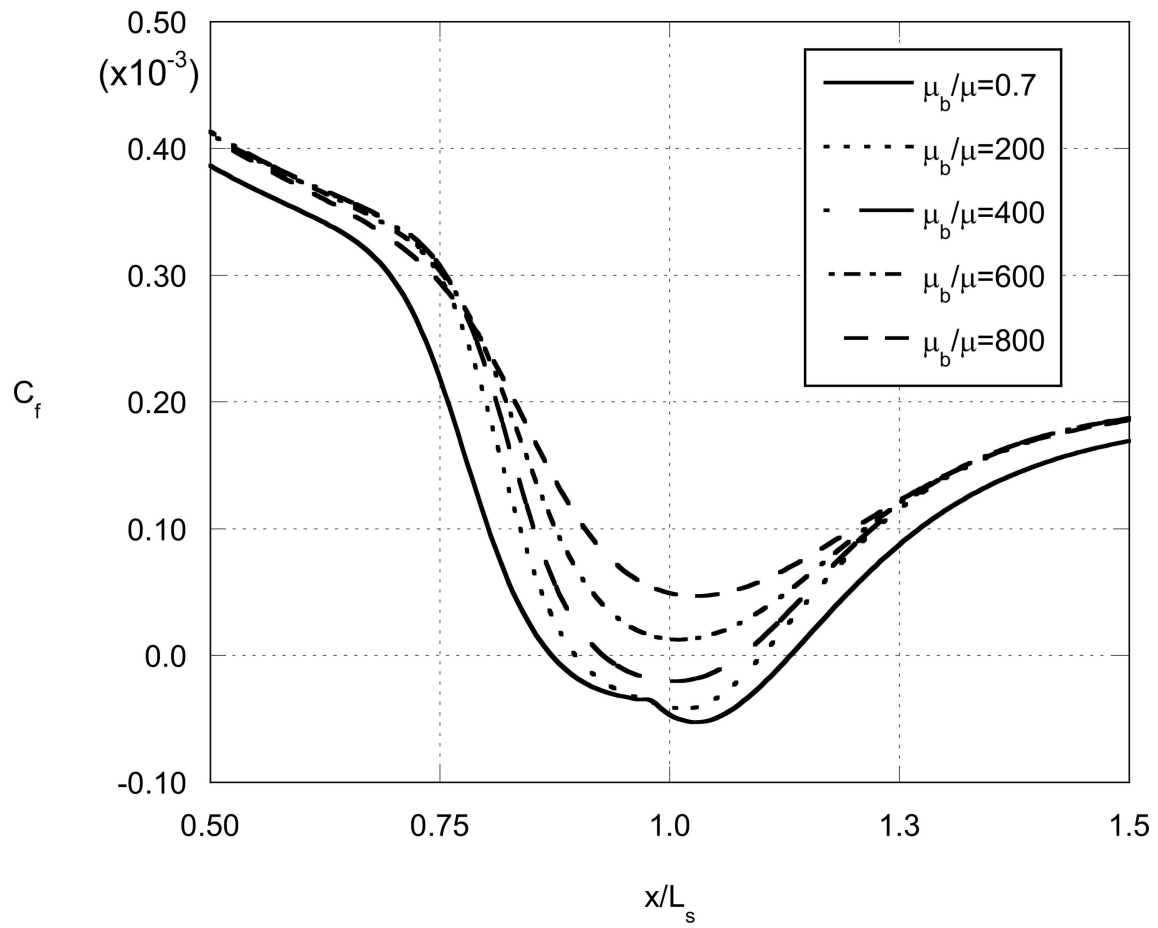


Figure 4.7: Skin friction coefficients along the plate for large bulk viscosity fluids.

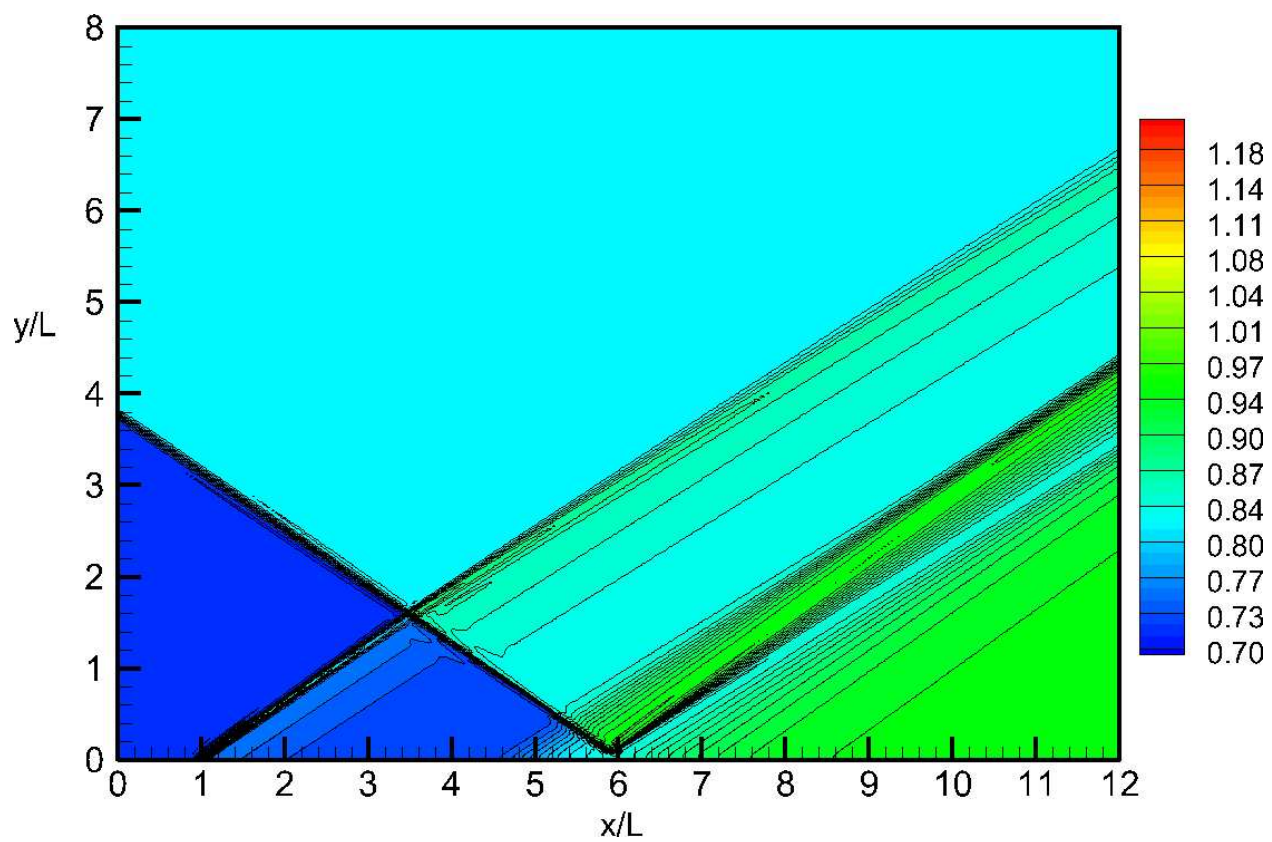


Figure 4.8: Contour of scaled pressure for classical fluids,  $\mu_b/\mu = 0.7$ .

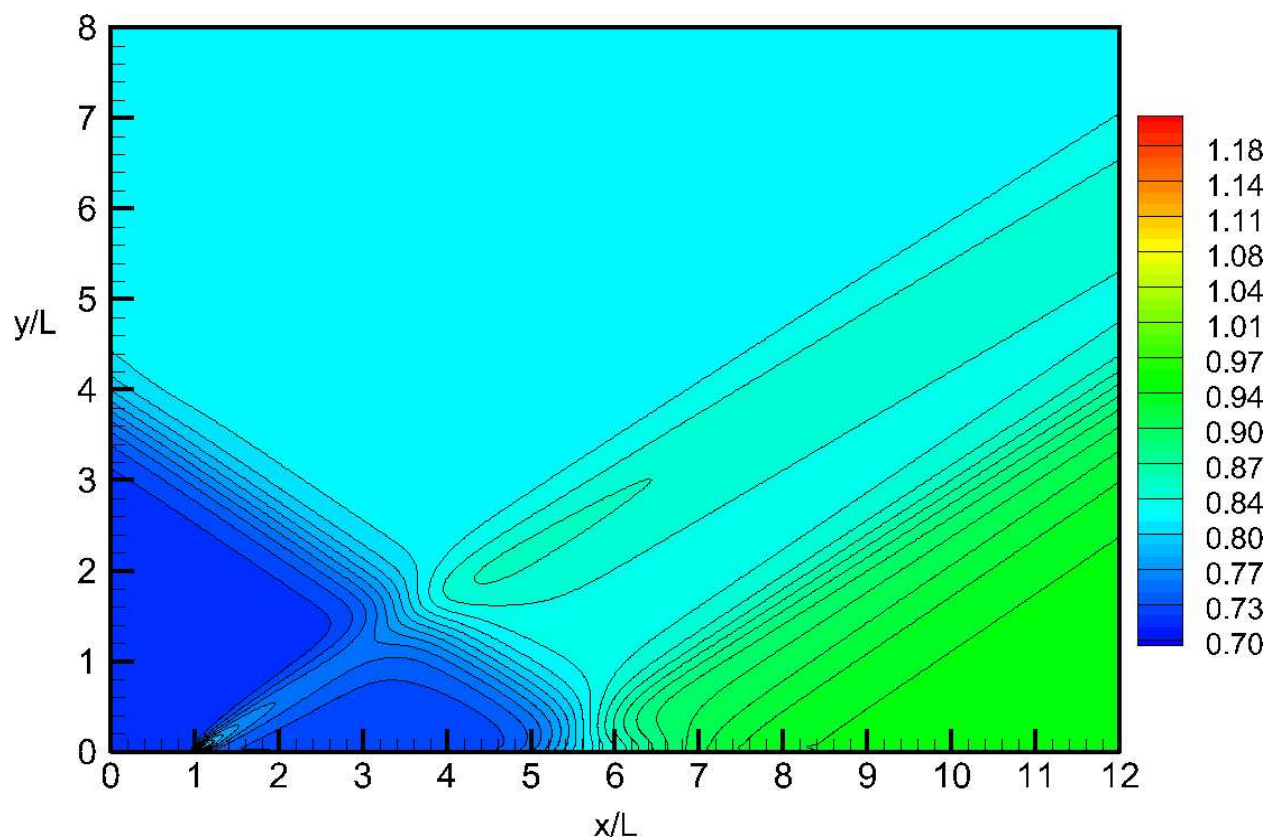


Figure 4.9: Contour of scaled pressure for large bulk viscosity fluids,  $\mu_b/\mu = 800$ .

## 4.5 Summary

We have used the WENO numerical scheme to compute the interaction of an oblique shock with a laminar boundary layer on a flat adiabatic plate. The fluid was taken to be perfect gas with a constant Prandtl number and a shear viscosity which is proportional to the absolute temperature. The main result is the demonstration that the thickening of the shock wave due to large bulk viscosities is sufficient to suppress boundary layer separation. The physical mechanism, i.e., the reduction of adverse pressure gradients, is expected to occur in many other flows. In particular, we expect the use of large bulk viscosity fluids, e.g.,  $\text{CO}_2$ ,  $\text{N}_2\text{O}$ ,  $\text{SF}_6$ , etc., can lead to reductions in separation in problems involving turbulent boundary layers, transonic flows or those in which the adverse pressure gradients are generated at trailing edges by rivets, cooling or heating.

# Chapter 5

## Fluids with Non-Convex Equations of State

### 5.1 Introduction

The last problem to be examined is the two-dimensional steady supersonic flow of a Bethe-Zel'dovich-Thompson (BZT) fluid over a thin airfoil or turbine blade. A motivation for this problem is to illustrate the complex flow patterns possible for simple airfoil shapes. The freestream state will be chosen so that the fundamental derivative (1.2) is negative for part or even all of the flow. As a result, compression shocks will disintegrate into compression fans or shock-fan combinations. This disintegration is illustrated in Figure 5.1. As suggested by the sketch of Figure 5.1, the adverse pressure gradient carried by the resultant pressure waves ought to be significantly reduced when they strike a neighboring turbine blade. The calculations presented here are for inviscid flows, but we expect that future computations will show that the reduction of the adverse pressure gradient will reduce the occurrence of shock-induced separation in power systems. Support for this expectation comes from the work of Cramer and Park [43] who showed that boundary layer separation can be suppressed when a pure compression fan strikes a laminar flat plate boundary layer.

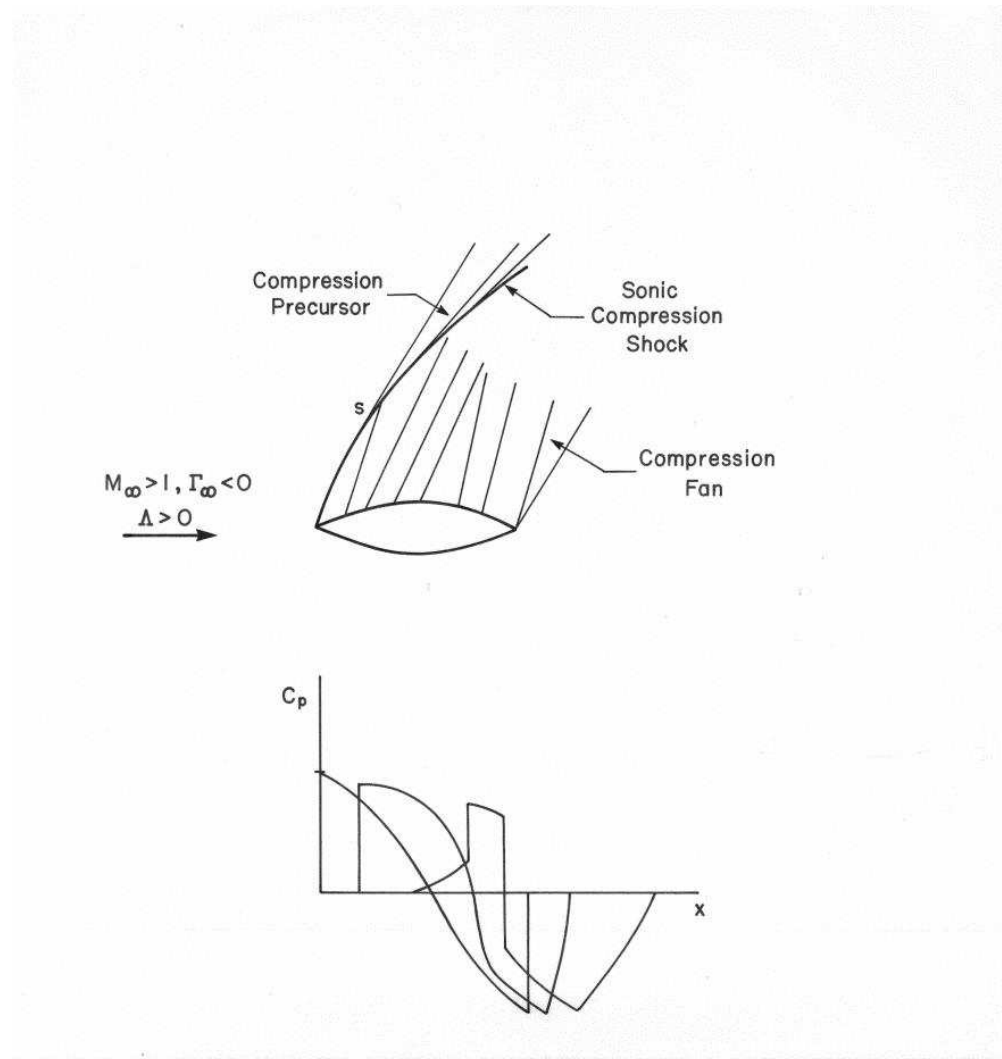


Figure 5.1: Example of flow patterns with a BZT fluid.

As an example, the variation of the fundamental derivative of a selection of familiar fluids and the heat transfer fluids FC-43, PP10, PP-11, FC-71 is plotted in Figure 5.2. Because  $\Gamma < 0$  for a range of temperatures and pressures each of the latter are regarded as BZT fluids; a description of the modeling and computations leading to the variation seen in Figure 5.2 can be found in Thompson and Lambrakis [26] and Cramer [45]. Use of the parabolic approximation for the local value of the fundamental derivative is capable of capturing the two zeros of  $\Gamma$  and its local minimum seen in Figure 5.2.



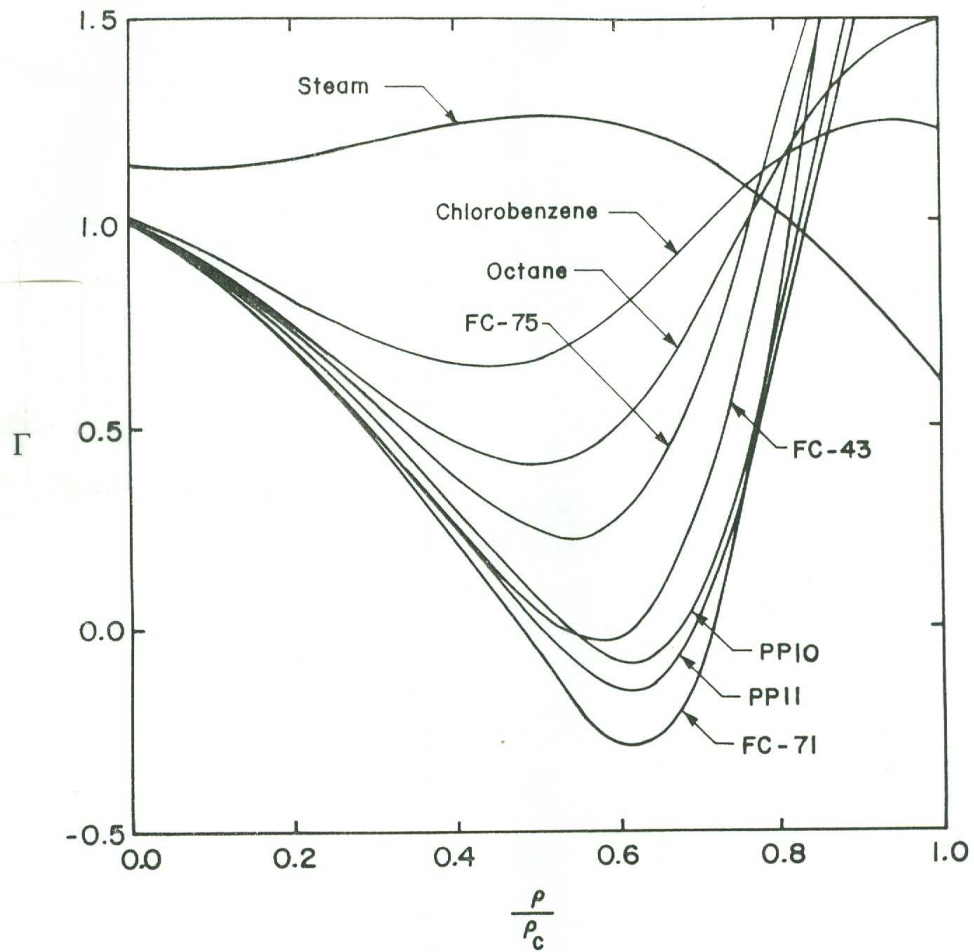


Figure 5.2: Variation of the scaled fundamental derivative vs. scaled density along the critical isotherm. The quantity  $\rho_c$  denotes the density at the critical point for each fluid.

A second motivation for this work is the demonstration that the WENO technique, discussed in Section 4.5, is well-suited to the study of BZT fluids. The partial disintegration of shocks into shock-fan combinations results in the need to capture discontinuities embedded in smooth transitions in a very precise way. The ability of the WENO technique to generate very thin shocks without oscillation makes this technique a valuable tool in the study of BZT fluids.

## 5.2 Review of Crickenberger's Theory

The weak shock theory for BZT fluids was originally developed by Crickenberger [29]. As in the classical weak shock theory, the Euler equations and oblique shock relations for steady flow are perturbed for small disturbances, e.g., for thin wings. In the classical weak shock theory, the fundamental derivative (1.2) is taken to be  $O(1)$ . However, in order to capture the full range of qualitative behaviors of BZT fluids, Crickenberger [29] took

$$\tilde{\Gamma}_\infty = O\left(\frac{\rho - \rho_\infty}{\rho_\infty}\right)^2 = o(1), \quad (5.1)$$

$$\Lambda_\infty = \frac{\rho_\infty^2}{a_\infty} \frac{\partial \Gamma}{\partial \rho} \Big|_s (\rho_\infty, s_\infty) = o(1), \quad (5.2)$$

$$\Xi_\infty = \frac{\rho_\infty^3}{a_\infty} \frac{\partial^2 \Gamma}{\partial \rho^2} \Big|_s (\rho_\infty, s_\infty) = O(1). \quad (5.3)$$

where  $\rho_\infty, s_\infty$  are the values of density and entropy in the freestream. In all the following  $\Xi_\infty$  will be taken to be  $> 0$ . As a result, the Taylor series for (1.2) for  $\rho \approx \rho_\infty$  and  $s = s_\infty$  can be written

$$\tilde{\Gamma}_l = \tilde{\Gamma}_\infty + \Lambda_\infty \frac{\rho - \rho_\infty}{\rho_\infty} + \frac{\Xi_\infty}{2} \left(\frac{\rho - \rho_\infty}{\rho_\infty}\right)^2 + O\left(\frac{\rho - \rho_\infty}{\rho_\infty}\right)^3 \quad (5.4)$$

where  $\tilde{\Gamma}_l$  is the local value of  $\tilde{\Gamma}$ . Thus, each term shown in (5.4) will be  $O\left(\frac{\rho - \rho_\infty}{\rho_\infty}\right)^2$ , the local value of  $\tilde{\Gamma}$  will be  $O\left(\frac{\rho - \rho_\infty}{\rho_\infty}\right)^2$  and  $\tilde{\Gamma}$  vs  $\rho$  will be a parabola. A comparison of the approximation (5.4) to the exact variation of  $\tilde{\Gamma}$  is provided in Figure 5.3.

An important consequence of the approximations (5.1)-(5.3) can be seen by inspection of the Bethe-Duhem relation for the jump in entropy across a weak shock wave, i.e.,

$$[[s]] = \tilde{\Gamma}_\infty \frac{a_\infty^2}{6T_\infty} \left(\frac{[[p]]}{\rho_1 a_1^2}\right)^3, \quad (5.5)$$

where  $\llbracket A \rrbracket \equiv A_2 - A_1 = \text{jump in the } A \text{ across a shock}$  and the subscript 1 denotes the state before the shock. If we combine (5.5) with (5.1)-(5.3), it is clear that the entropy change across a weak shock is

$$\frac{\llbracket s \rrbracket}{R} = O\left(\frac{\llbracket \rho \rrbracket}{\rho_\infty}\right)^5. \quad (5.6)$$

Thus (5.4) is also accurate even where shocks are present. Crickenberger [29] has used (5.6) to show that the weak shock theory of BZT fluids can be regarded as isentropic to the needed approximation. The second issue considered by Crickenberger [29] was the size of reflected waves. The technical issue was to determine whether the change in the Riemann invariant associated with upstream or left-running Mach waves is negligible. When the size of the entropy jumps and fundamental derivative were taken into account and both the invariant and Rankine-Hugoniot shock jump conditions were approximated, it was shown that

$$\llbracket R^- \rrbracket = O\left(\frac{\rho - \rho_\infty}{\rho_\infty}\right)^4, \quad (5.7)$$

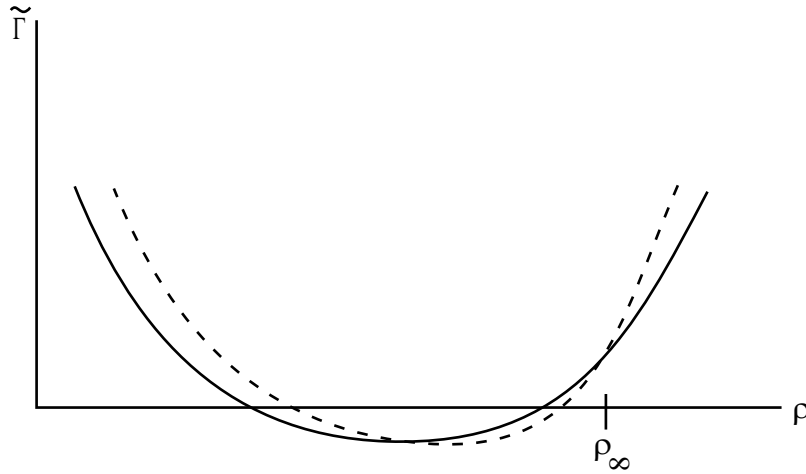


Figure 5.3: Sketch of the variation of  $\tilde{\Gamma}$  on an isentrope. The solid line is the exact variation and the dashed line is the approximation (5.4).

where

$$R^- \equiv \theta - \nu, \quad (5.8)$$

is the Riemann invariant associated with upstream or left-running Mach lines. Here  $\theta$  is the flow deflection angle and  $\nu$  is the Prandtl-Meyer function. We take the flow to be that sketched in Figure 5.4. The flow far upstream is parallel to the positive  $x$ -axis so that  $\theta = 0$  in the freestream.

The angle between the freestream and a right-running Mach wave is  $\psi = \theta + \mu$ , where

$$\mu \equiv \sin^{-1} \left( \frac{1}{M} \right) \quad (5.9)$$

is the local Mach angle. Here  $M$  = local Mach number. Thus, for a simple right-running (down-

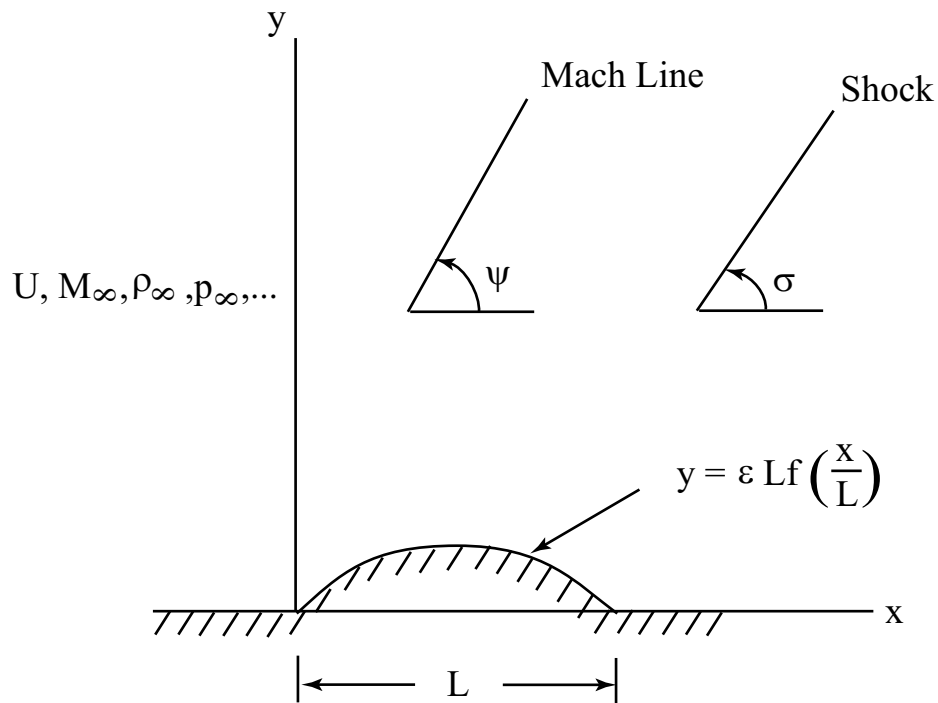


Figure 5.4: Sketch of the flow and notation.

stream pointing) Mach wave, we have

$$\rho, p, T, M, \text{ etc.} = \text{constant}, \quad \theta \approx \nu - \nu_\infty = \text{constant} \quad (5.10)$$

on

$$\frac{dy}{dx} = \tan\psi \quad (5.11)$$

where the fact that (5.8) can be taken to be nearly constant has been used. The variation of  $\psi$  can also be shown to satisfy

$$\frac{d\psi}{d\theta} = \tilde{\Gamma} \frac{M^2}{M^2 - 1} \quad (5.12)$$

in a simple right-running wave (Thompson [22], Crickenberger [29]). From the simple wave condition (5.10), we may also show

$$d\theta = d\nu = \frac{\sqrt{M^2 - 1}}{M^2} \frac{d\rho}{\rho}, \quad (5.13)$$

and therefore that (5.12) can be rewritten as

$$\frac{d\psi}{d\rho} = \frac{1}{\rho} \frac{\tilde{\Gamma}}{\sqrt{M^2 - 1}}. \quad (5.14)$$

If we now use the small disturbance approximation combined with (5.4), we find that (5.14) can be integrated to yield

$$\psi \approx \mu_\infty + \frac{1}{\sqrt{M^2 - 1}} \left[ \tilde{\Gamma}_\infty \bar{\rho} + \frac{\Lambda_\infty}{2} \bar{\rho}^2 + \frac{\Xi_\infty}{6} \bar{\rho}^3 + O(\bar{\rho}^4) \right], \quad (5.15)$$

where

$$\bar{\rho} \equiv \frac{\rho - \rho_\infty}{\rho_\infty}. \quad (5.16)$$

If we combine (5.15) with (5.11), we find that

$$\begin{aligned} \frac{dy}{dx} &\approx \tan\mu_\infty + \frac{1}{\cos^2\mu_\infty}(\psi - \mu_\infty) + o(\bar{\rho}^3) \\ &\approx \frac{1}{\sqrt{M^2 - 1}} + \frac{M_\infty^2}{(M_\infty^2 - 1)^{\frac{3}{2}}} \left( \tilde{\Gamma}_\infty \bar{\rho} + \frac{\Lambda_\infty}{2} \bar{\rho}^2 + \frac{\Xi_\infty}{6} \bar{\rho}^3 \right) + O(\bar{\rho}^4) \end{aligned} \quad (5.17)$$

is the lowest order slope of the Mach lines. We now define

$$F \equiv -(u^4 + 4Au^3 + 12Bu^2), \quad (5.18)$$

where

$$u \equiv \epsilon \bar{\rho} = O(1) \quad (5.19)$$

$$A \equiv \frac{\Lambda_\infty}{\Xi_\infty \epsilon} = O(1) \quad (5.20)$$

$$B \equiv \frac{\tilde{\Gamma}_\infty}{\Xi_\infty \epsilon^2} = O(1) \quad (5.21)$$

and  $\epsilon \ll 1$  is the small disturbance parameter seen in Figure 5.4. The Mach angle and slope of the Mach lines become

$$\psi - \mu_\infty = -\frac{\epsilon^3 \Xi_\infty}{24} \frac{1}{\sqrt{M_\infty^2 - 1}} F' + O(\epsilon^4) \quad (5.22)$$

$$\frac{dy}{dx} = \frac{1}{\sqrt{M_\infty^2 - 1}} \left( 1 - \epsilon^3 \frac{M_\infty^2}{\sqrt{M_\infty^2 - 1}} \frac{\Xi_\infty}{24} F' \right) + O(\epsilon^4) \quad (5.23)$$

where the prime denotes differentiation with respect to  $u$ . If we combine (5.10)-(5.11) with (5.19) and (5.23), we have

$$du = 0$$

on

$$\frac{dy}{dx} = 2\sqrt{M_\infty^2 - 1} \left( 1 + \epsilon^3 \frac{M_\infty^2}{M_\infty^2 - 1} \frac{\Xi_\infty}{24} F' \right) + O(\epsilon^4)$$

or

$$\left. \frac{du}{dy} \right|_X + \epsilon^3 \frac{\Xi_\infty}{24} \frac{M_\infty^2}{\sqrt{M_\infty^2 - 1}} F' \left. \frac{du}{dX} \right|_y = 0 \quad (5.24)$$

where  $u$  is now regarded as a function of  $X \equiv x - \sqrt{M_\infty^2 - 1} y$  and  $y$ . Equation (5.24) is recognized as an inviscid Burgers equation corresponding to the quartic flux function (5.18). In fact, we can simplify (5.24) further by nondimensionalizing  $y$  and  $X$  as follows

$$\begin{aligned} \hat{y} &\equiv \frac{y}{L} \epsilon^3 \frac{\Xi_\infty}{24} \frac{M_\infty^2}{\sqrt{M_\infty^2 - 1}}, \\ \chi &\equiv \frac{X}{L}, \end{aligned} \quad (5.25)$$

yielding

$$\left. \frac{\partial u}{\partial \hat{y}} \right|_\chi + F' \left. \frac{\partial u}{\partial \chi} \right|_{\hat{y}} = 0 \quad (5.26)$$

or, in conservative form,

$$\left. \frac{\partial u}{\partial \hat{y}} \right|_\chi + \left. \frac{\partial F}{\partial \chi} \right|_{\hat{y}} = 0 \quad (5.27)$$

Once (5.26) or (5.27) is solved for  $u = u(\chi, \hat{y})$  the flow deflection angle  $\theta$  can be found by the lowest order form of the simple wave condition (5.13) and the definition (5.19) to yield

$$\theta \approx \frac{\sqrt{M_\infty^2 - 1}}{M_\infty^2} \epsilon u. \quad (5.28)$$

Furthermore, the pressure variations can be determined by expanding  $p = p(\rho, s)$  in a Taylor series about  $\rho_\infty$  and  $s_\infty$  to obtain

$$\frac{p - p_\infty}{\rho_\infty a_\infty^2} \approx \epsilon u. \quad (5.29)$$

The boundary condition corresponding to the airfoil or turbine blade sketched in Figure 5.4 by

imposing the no-penetration condition at the wing or airfoil surface to yield:

$$\theta \approx \epsilon \dot{f}(\chi) \text{ on } \hat{y} \approx 0, \quad (5.30)$$

where the small disturbance approximation has been used and

$$\dot{(\ )} \equiv \frac{d(\ )}{d(X/L)} = \frac{d(\ )}{d\chi}. \quad (5.31)$$

If we combine (5.30) with (5.28) we have

$$u = \frac{M_\infty^2}{\sqrt{M_\infty^2 - 1}} \dot{f}(\chi) \text{ on } \hat{y} = 0 \quad (5.32)$$

as the boundary condition on  $u = u(\chi, \hat{y})$  corresponding to the Burgers equation (5.26) or (5.27). The function  $F = F(u)$  will be referred to as the flux function. Crickenberger [29] has shown that  $F$  is directly related to the shape of the isentropes or, because the shocks are essentially isentropic, the shock adiabats in a pressure-volume diagram. A few typical  $F$  vs  $u$  curves have been plotted in Figure 5.5. It is easily shown that (5.4) can be rewritten.

$$\tilde{\Gamma}_l = -\epsilon^3 \frac{\Xi_\infty}{24} F''' + O(\epsilon^3). \quad (5.33)$$

Thus, regions of  $F'' > 0$  (concave up) correspond to regions of  $\tilde{\Gamma}_l < 0$  and regions where of  $F'' < 0$  (concave down) correspond to  $\tilde{\Gamma}_l > 0$ . When the local value of  $\tilde{\Gamma}$  changes sign the  $F$  vs  $u$  curve will have an inflection point. When an isentrope passes through a region of  $\tilde{\Gamma} < 0$ , the  $F$  curve and shock adiabat will generally have two inflection points. When this is the case we refer to the fluid as having a non-convex shock adiabat or flux function  $F$ .

We now consider the possibility of shock waves in the present theory. Crickenberger [29] has given the detailed oblique shock relations corresponding to (5.26) or (5.27). We can also derive



the shock existence conditions by requiring that the present inviscid theory be consistent with a dissipative theory; i.e., we can require that all admissible shocks have a physically realizable dissipative structure. Regardless of which approach is used we find that the scaled shock slope is

$$\left. \frac{d\chi}{d\hat{y}} \right|_s = S = \frac{[[F]]}{[[u]]}. \quad (5.34)$$

If we transform back to physical variables, we have

$$\left. \frac{dx}{dy} \right|_s = \frac{1}{\tan\sigma} = \sqrt{M_\infty^2 - 1} + \epsilon^3 S \frac{\Xi_\infty}{24} \frac{M_\infty^2}{\sqrt{M_\infty^2 - 1}} + O(\epsilon^4) \quad (5.35)$$

where  $\sigma$  is the shock angle relative to the incoming flow as depicted in Figure 5.4. Alternatively, we could expand  $\tan\sigma$  for small disturbances to obtain:

$$\sigma \approx \mu_\infty - \epsilon^3 \frac{\Xi_\infty}{24} \frac{S}{\sqrt{M_\infty^2 - 1}} + O(\epsilon^4) \quad (5.36)$$

or, using (5.22),

$$\sigma - \psi_i \approx \frac{\epsilon^3}{\sqrt{M_\infty^2 - 1}} \frac{\Xi_\infty}{24} (F'_i - S) + O(\epsilon^4) \quad (5.37)$$

where the subscript  $i = 1$  or  $2$  corresponds to conditions on either side of the shock. It can also be shown that the normal component of the Mach number  $M_{ni}$  on either side of the shock is given by

$$M_{ni}^2 - 1 = \epsilon^3 \frac{\Xi_\infty}{12} (F'_i - S) + O(\epsilon^4) \quad (5.38)$$

and is therefore directly related to the slopes of the  $F$  curve and the difference between the shock and Mach angles, i.e.,  $\sigma - \psi_i$ , i.e.,

$$\sigma - \psi_i \approx \frac{1}{2} \frac{1}{\sqrt{M_\infty^2 - 1}} (M_{ni}^2 - 1) \quad (5.39)$$

In order to state the existence condition for weak oblique shocks, we must first define

$$F = F_R(u) = F_1 + S(u - u_1), \quad (5.40)$$

which, by (5.34), is a straight line connecting any two points on the  $F$  vs  $u$  curve. The straight line corresponds to a Rayleigh line in the pressure volume diagram and we will henceforth refer to (5.40) as a Rayleigh line. Following Crickenberger [29], we take the fundamental existence condition to be as follows:

*A proposed discontinuity having  $[[u]] > 0$  ( $< 0$ ) is admissible iff  $F > F_R$  ( $< F_R$ ) at every  $u \in (u_1, u_2)$ .*

Here the subscripts 1 and 2 refer to conditions before and after the shock. Thus the Rayleigh line for every physically admissible shock must either lie entirely above or below the  $F$  curve between  $u_1$  and  $u_2$ . The direction of the jump of the physically admissible shock will depend on whether  $F > F_R$  or  $F < F_R$ . Thus, the type of shocks which can occur depend on the shape of the  $F$  vs  $u$  curve in a fundamental way. Rayleigh lines corresponding to admissible shocks are sketched in Figure 5.5.

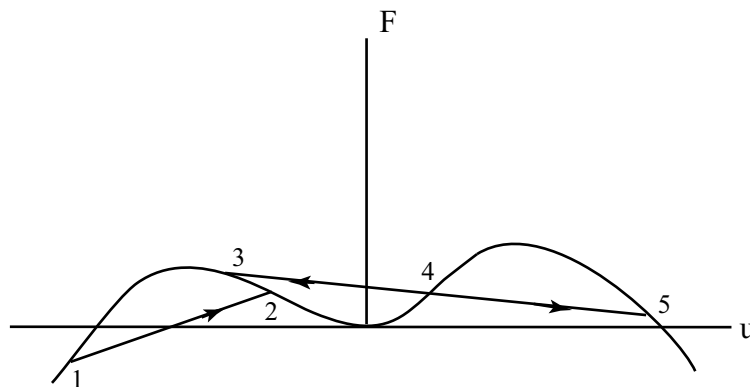


Figure 5.5: Sketch of  $F$  vs  $u$  curve and Rayleigh lines. Proposed discontinuities 3-5 are inadmissible because the Rayleigh line 3-5 does not lie entirely above or below the  $F$  curve. Arrows denote the direction of jumps for the admissible shocks 4-3, 4-5, 1-2.

The above admissibility condition is based on the existence of a physically realizable dissipative structure; See, e.g., Menikoff and Plohr [27] and Cramer [28].

Examination of the relative slopes of the Rayleigh lines and the  $F$  vs  $u$  curve reveals that

$$F'_1 \geq S \geq F'_2$$

for all admissible shocks, where subscripts 1 and 2 again refer to the conditions before and after the shock. From (5.38), we see that

$$M_{n1} \geq 1 \geq M_{n2}$$

for all admissible shocks. Thus, all admissible shocks will correspond to a supersonic-subsonic transition in the normal direction. From (5.37) we can also conclude that the Mach lines will always intersect the shock.

A feature not seen when the  $F$  curve is convex is that the Rayleigh lines could be tangent to the  $F$  curve at either points 1 or 2 or both. An inspection of results (5.37)-(5.38) reveal that the normal component of the Mach number is  $= 1$  and the Mach line is tangent to the shock at such points. We refer to these tangent points as sonic shocks following Cramer and Kluwick [46].

### 5.3 Numerical Method

The spatial discretization is done by fifth order weighted essentially non-oscillatory (WENO) scheme and the temporal discretization is done using third order Runge Kutta scheme. The WENO scheme avoids spurious oscillations near shocks, the so called Gibbs phenomena. This scheme is uniformly high order accurate and resolves the non-linear shocks with sharp but monotone transitions. Previous studies related to this work are due to Monaco, Cramer, and Watson (1997) who applied a finite difference scheme to the Euler equations in a cascade configuration. The primary

focus was on the search for shock-free flows within the cascade passage and a study of the flow details was not carried out. A second related study is due to Liu, et. al. [38] who applied the WENO technique to a Burgers equation corresponding to a Buckley-Leverett equation. Because the flux function was also of the non-convex type, the authors were able to illustrate the use of the WENO technique to shock-fan combinations. The code has been written, debugged and tested and the results have been compared with the exact solution. Inspection of the results shows excellent agreement between the exact solution and the numerical computations using the WENO scheme.

## 5.4 Comparison to Exact Solution

As a partial validation of our code, we compare the numerical solutions to exact for simple ramp flows. The expression for  $\dot{f}$  in (5.32) is

$$\dot{f} = \begin{cases} 0 & \text{for } \chi < 0 \\ \alpha & \text{for } \chi > 0 \end{cases} \quad (5.41)$$

where

$$\alpha \equiv \frac{M_\infty^2}{\sqrt{M_\infty^2 - 1}} \frac{\theta_w}{\epsilon} = \text{constant} \quad (5.42)$$

and  $\theta_w$  = the physical ramp angle. The exact solutions are obtained by combining the method of characteristics solutions with the shock speed relation (5.34) and the admissibility condition; see, e.g., Crickenberger [29]. The first example corresponds to a freestream Mach number of 2 and  $A = -1.5$ ,  $B = 0.8$ . The corresponding  $F$  vs  $u$  curve is plotted in Figure 5.6. In the first comparison, the ramp is a compression ramp with  $\alpha > 0$ . The resultant  $u$  variations are compared to the exact solutions in Figure 5.7 at  $\hat{y} = 0.5$ . Every 50 data point is plotted for the numerical solution. When  $\alpha = 1$  the shock is an ordinary oblique shock. When  $\alpha = 2$ , the Rayleigh line from

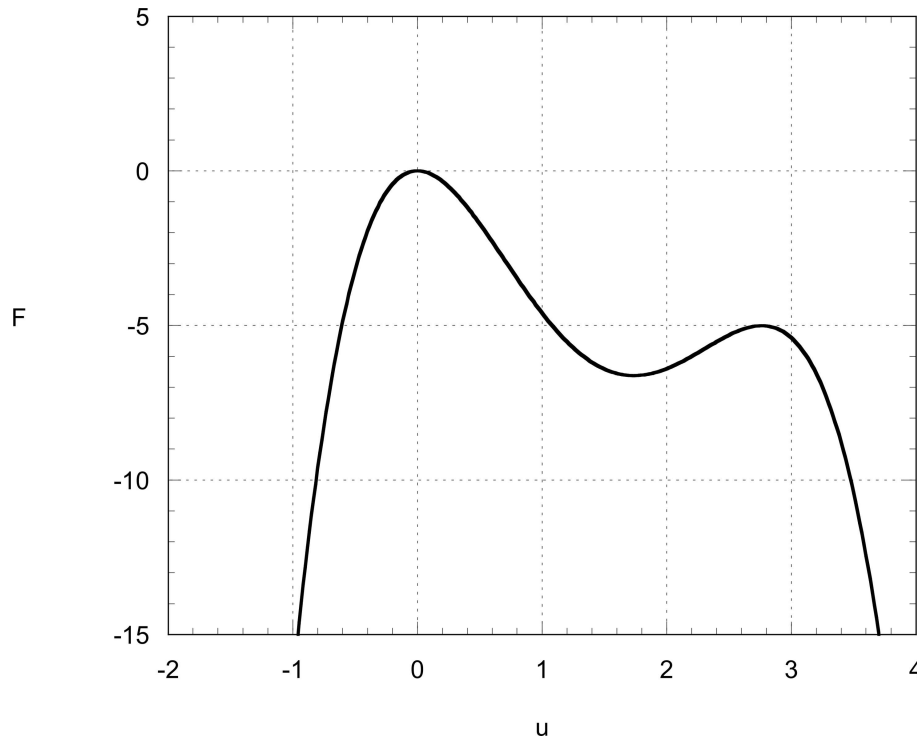


Figure 5.6:  $F$  vs  $u$  curve for  $\Gamma_\infty > 0$  and  $\Lambda_\infty < 0$ .

$u = 0$  to  $u = 2$  crosses the  $F$  curve, the shock is therefore inadmissible and breaks into a shock-fan combination. The WENO scheme is seen to capture the shock and allow a clear distinction between the centered fan and the discontinuity. At  $\alpha = 3.2$ , the discontinuity breaks into a split-shock configuration in which the lead sonic shock is followed by a centered fan. The remainder of the compression is accomplished by a shock which is sonic at the upstream condition. At  $\alpha = 4$ , the Rayleigh line no longer crosses the  $F$  curve and the resultant shock is again seen to be a single compression shock.

The second case is an expansion ramp having  $\alpha < 0$  with  $A = 2$ ,  $B = 1.45$ . A plot of the  $F$  vs  $u$  curve is provided in Figure 5.8. In this case the freestream state is in the high pressure  $\tilde{\Gamma} > 0$  region. The comparison of the solutions for  $u = u(\chi)$  are plotted in Figure 5.9 for  $\hat{y} = 0.5$ . Every 30 data point is plotted for the numerical solution in this figure. At the smallest value of  $|\alpha|$ , i.e.,  $\alpha = -0.5$ , the expansion corner simply generates a centered expansion fan. At  $\alpha = -2.5$  the

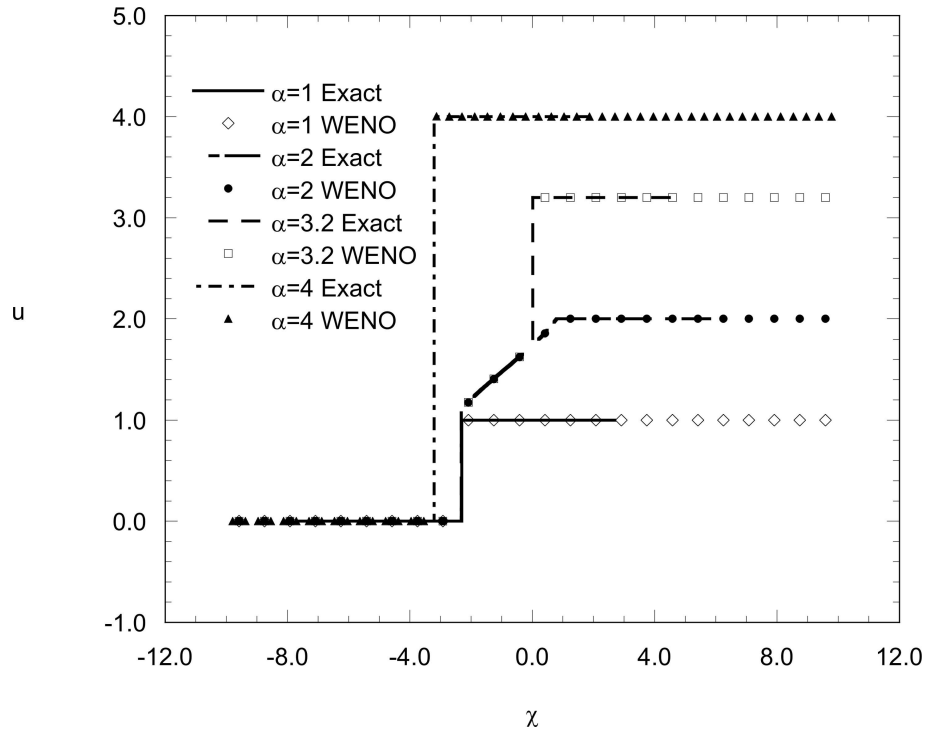


Figure 5.7: Numerical and exact solutions of flow over wedge at a freestream Mach number of 2 and  $\Gamma_\infty > 0$  and  $\Lambda_\infty < 0$ . The quantity  $\alpha$  is the (negative) scaled wedge angle. The horizontal axis is distance in the flow direction in a frame moving with the Mach lines of the undisturbed flow. The vertical axis is a scaled measure of the flow deflection angle as defined in (5.28).

Rayleigh line from  $u = 0$  to  $u = \alpha$  again crosses the  $F$  curve and the sonic expansion shock forms at the downstream side of the expansion fan. The expansion shock is easily captured by our WENO scheme. When the ramp angle is increased to  $\alpha = -4$ , the expansion must be accomplished through a double sonic expansion shock followed by an expansion fan.

From these examples and others not reported here we conclude that the WENO scheme is capable of capturing both expansion and compression discontinuities. It is also able to distinguish between the smooth variations of  $u$  and the admissible shock waves.

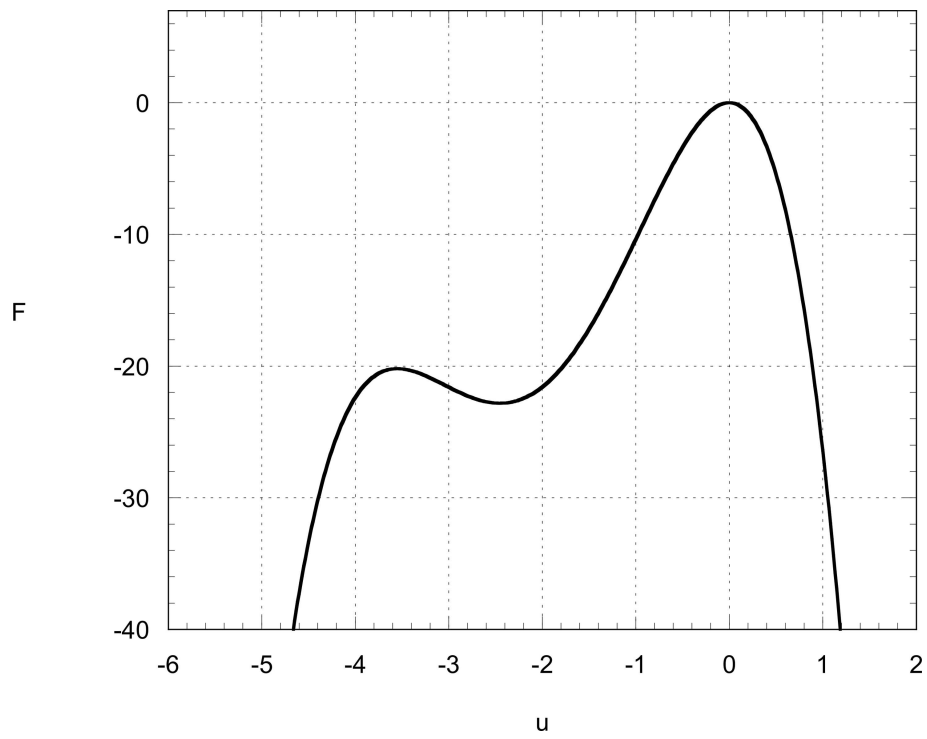


Figure 5.8: The  $F$  vs  $u$  curve for  $\Gamma_\infty > 0$  and  $\Lambda_\infty > 0$ .

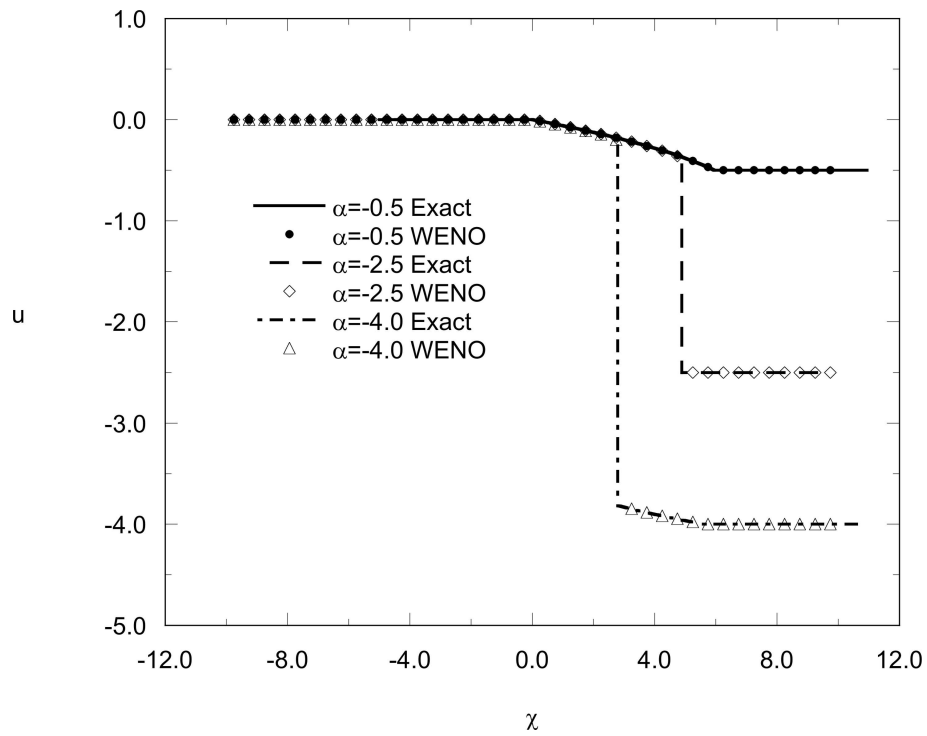


Figure 5.9: Numerical and exact solutions of flow over wedge at a freestream Mach number of 2 and  $\Gamma_\infty > 0$  and  $\Lambda_\infty > 0$ . The quantity  $\alpha$  is the (negative) scaled wedge angle. The horizontal axis is distance in the flow direction in a frame moving with the Mach lines of the undisturbed flow. The vertical axis is a scaled measure of the flow deflection angle as defined in (5.28).



## 5.5 Numerical Results

To illustrate the flow around an airfoil, we consider a circular arc airfoil defined by

$$f = f(\chi) = \chi(1 - \chi) \text{ for } 0 < \chi < 1 \quad (5.43)$$

and  $f = 0$  otherwise. We take the values of  $A$  and  $B$  to be those of the compression ramp illustrated in Figures 5.6-5.7, i.e.,  $A = -1.5$  and  $B = 0.8$ . We again take  $\alpha$  to be 4 so that the slope at the nose of the wing ( $\dot{f}(0)$ ) is identical to the slope of the compression ramp discussed in Section 5.4. Thus, the lead shock will initially be a single shock. As the Mach waves behind it strike the shock, it will be weakened until the Rayleigh line intersects the F curve. The lead shock is then inadmissible and will split into a lead compression shock followed by a smooth compression analogous to the centered compression fan seen in Figure 5.6 followed by a compression shock. Because the wing has a continuous slope, no expansion shock can begin at the wing. However, the expansion tends to occur in a  $\Gamma < 0$  region so that an expansion shock will form at some distance from the wing. In fact, it can be shown that the expansion shock will form at a distance of

$$\hat{y} = \frac{1}{24\alpha} \frac{1}{A^2 - 2B}$$

for (5.43) [Cramer, private communication]. For  $\alpha = 4$ ,  $A = -1.5$ ,  $B = 0.8$ , we find that the expansion shock forms at a distance of  $\hat{y} \approx 0.016$ . The contour plot for this case is provided in Figure 5.10.

The width of the computational domain was taken to be  $-0.5$ - $2.5$  in terms of  $\chi$  and we used 60 points on the wing. The vertical axis is  $\hat{y}$  and the horizontal axis is  $\chi$ . The shock splitting is clearly seen at the left of the plot and the formation of the expansion shock at  $\hat{y} \approx 0.016$  is also seen. At  $\chi > 0$ , the  $u < 0$ , so that the local value of  $\Gamma > 0$  and the flow over the last half of the wing

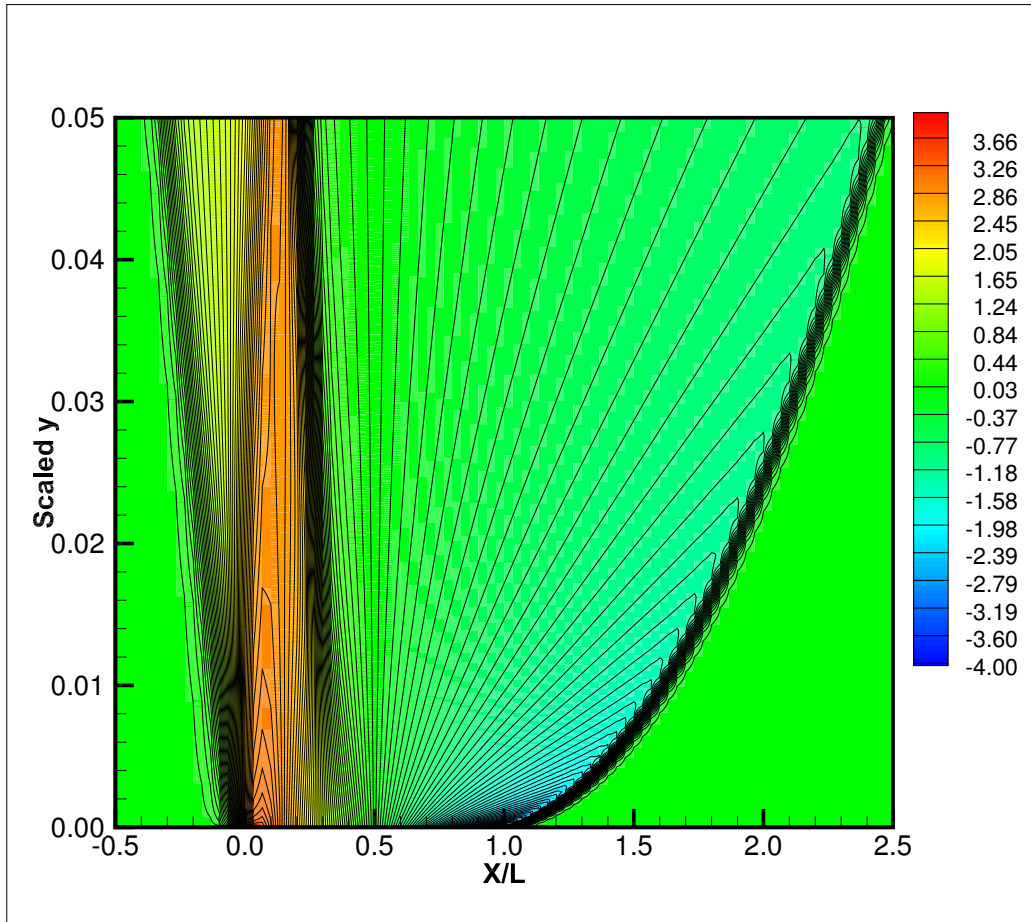


Figure 5.10: Contour plot for  $A = -1.5$ ,  $B = 0.8$ ,  $\alpha = 4$ , and a parabolic arc airfoil. Each contour line represents a  $\Delta u = 0.15$  from  $u = -4$  to  $u = 4$ . The airfoil is positioned between  $X = 0$  and  $X = L$ .

is qualitatively the same as a perfect gas. In order to further illustrate the variation of  $u$ , we have plotted  $u$  vs  $\chi$  at  $\hat{y} = 0.05$ , i.e., the upper boundary of the contour plot in Figure 5.10, in Figure 5.11. The three compression shocks at  $\chi \approx -0.25$ ,  $0$ , and  $2.4$  can be seen. The well formed expansion shock is seen at  $\chi \approx 0.25$ . Inspection of Figure 5.6 shows that this expansion shock is nearly the strength of the maximum strength, double sonic, expansion shock. As is suggested by an inspection of Figure 5.10, the second compression shock and expansion shock ultimately converge and collide leaving a single, but weaker expansion shock. We have not shown this collision in the contour plot because the initial dynamics would not be easily seen. However, we have plotted the

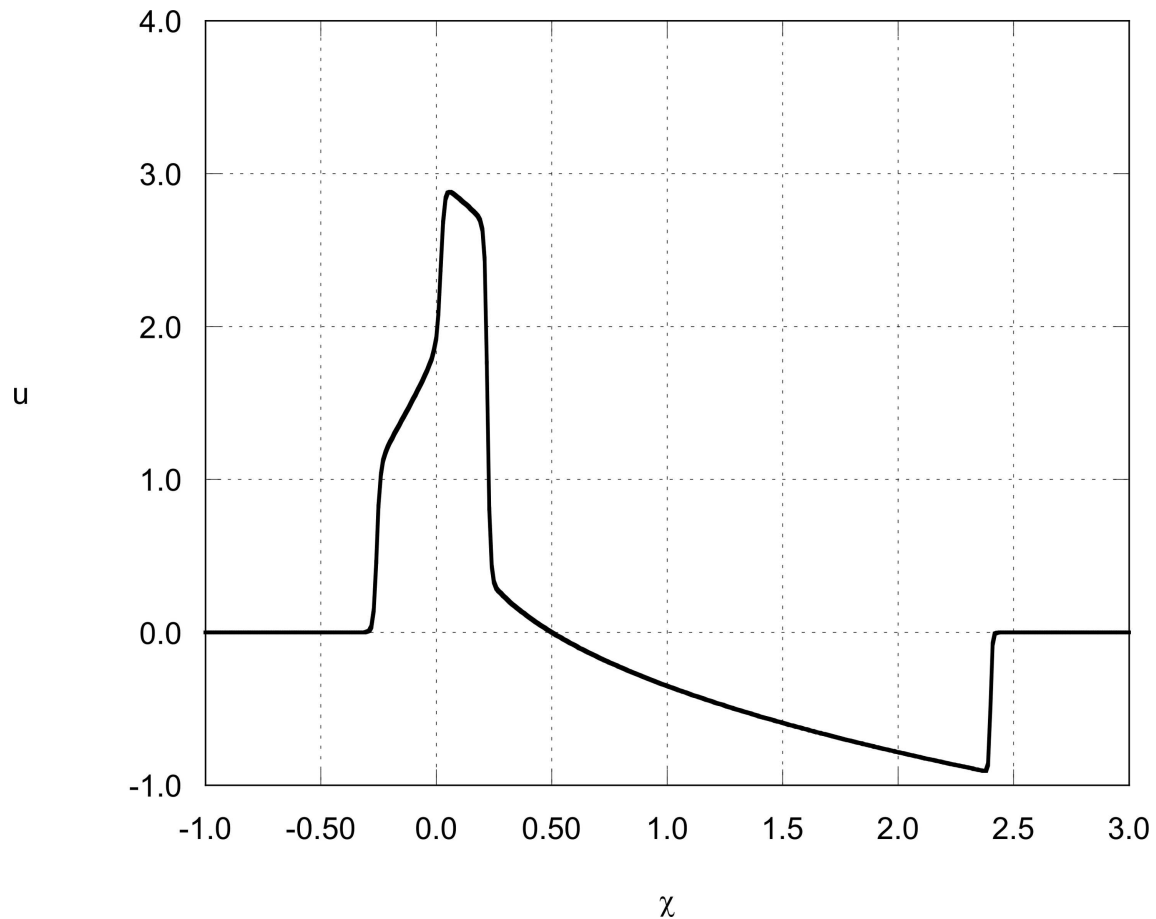


Figure 5.11: Plot of  $u$  vs  $\chi$  at  $\hat{y} = 0.05$  for the same case as illustrated in Figure 5.10.

$u$  variation for distances further from the wing in Figure 5.12.

The decay of the tail shock is roughly classical so that we have shown only the region from  $\chi = -2.5$  to 0. The values of  $\hat{y}$  were taken to be 0.05, 0.1, 0.2, and 0.4. At  $\hat{y} = 0.1$  (or 20 times the upper limit of Figure 5.10), the collision between the second compression shock and the expansion shock appears to be taking place or has just completed. After the collision, the evolution is even slower with the expansion shock decreasing in strength until the expansion shock and the lead compression shock collide leaving a single compression shock. Because  $\Gamma_\infty > 0$ , the final evolution will resemble that of a perfect gas, i.e., it will simply be an N-wave configuration which decays as  $\hat{y}^{-1/2}$ . In Figures 5.10-5.12, most of the details of the shock evolution are well resolved. The

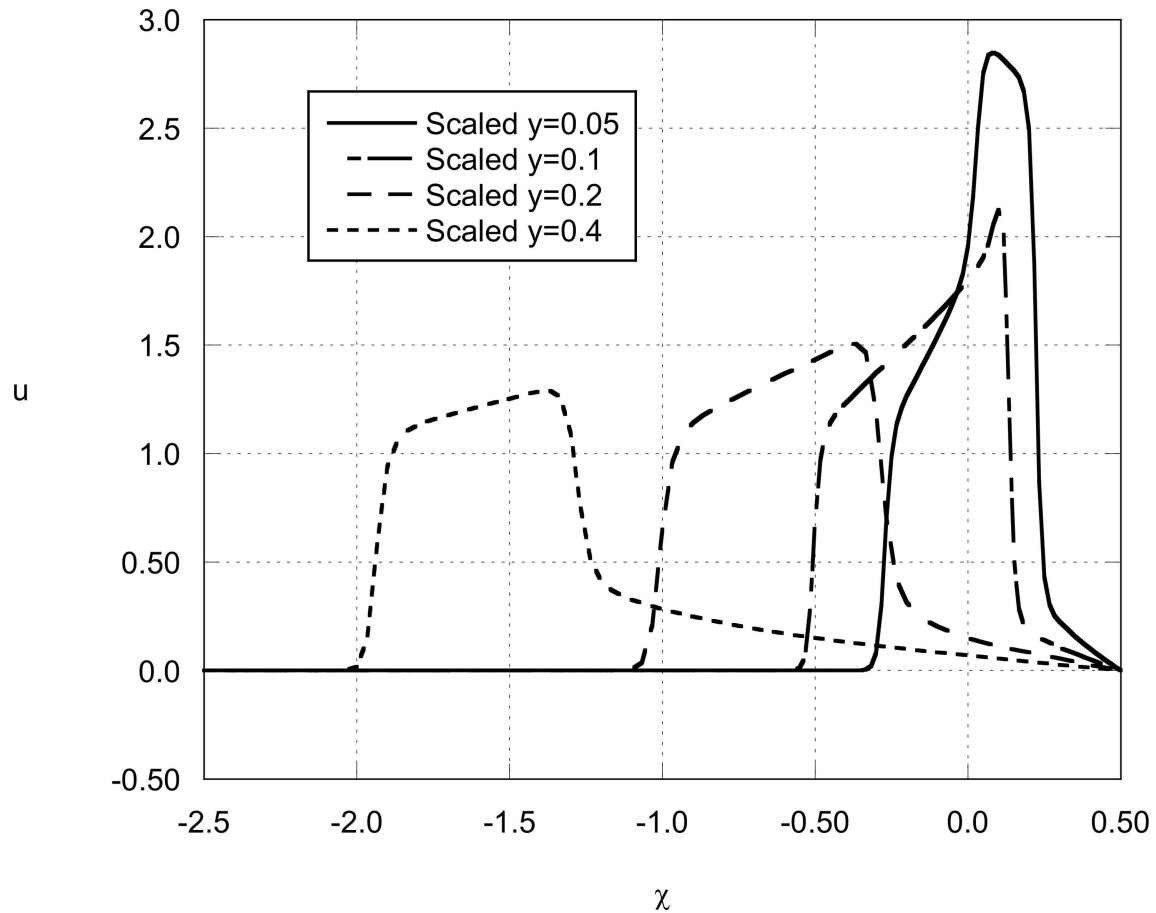


Figure 5.12: Plot of  $u$  vs  $\chi$  at values of  $\hat{y} = 0.05, 0.1, 0.2,$  and  $0.4$ . The wing shape and values of  $A, B, \alpha$  are identical to those of Figures 5.10-5.11.

resolution of the split shock could be improved by increases in the number of points used for the  $\chi$  direction. However, no significant improvement of the resolution of the remainder of the waveform were found and 60 points on the wing yields a rapid and reasonably accurate solution of the flow. A potential disadvantage of the WENO technique is the 5-point stencil. As seen in the present calculations, flows involving BZT fluids involve several shock waves which can collide or split. In these calculations and problems involving shock focusing (not reported here) the details of shock collisions or splitting can be difficult to resolve when the shocks are within one or two stencil widths of each other, i.e., when the shocks are within 5-20 grid points of each other. This problem is, of course, to be expected for any scheme and one should be careful when interpreting results at

collision or splitting times.

## **5.6 Summary**

The main objective of this chapter was to examine the use of the WENO scheme for capturing shock waves in problems involving non-convex flux functions. The scheme has been shown to be capable of isolating admissible discontinuities even when they are embedded in smooth flows. We have also examined the flow patterns possible over typical airfoil shapes. Results of interest are the formation of expansion shocks in the flow, the disintegration of compression shocks into split-shock configuration and the collision of compression and expansion shocks.

# Chapter 6

## Conclusion

In this thesis we have considered three problems involving compressible flows of single-phase Navier-Stokes fluids. The first two problems examine the effect of large bulk viscosity. In Chapter 3 the influence of large bulk viscosity on inviscid flows over bodies and boundary layers has been described. We regard this as an extension and partial validation of work of Emanuel [24]. In Chapter 4 we have used the WENO numerical scheme to solve the Navier-Stokes equations for the well known benchmark problem of shock boundary layer interaction on a flat plate. The primary result is the demonstration that the thickening of the incident shock can lower the adverse pressure gradient carried by the shock to the point where separation is fully suppressed. Because the key physical effect is the reduction of the adverse pressure gradient, we expect that similar results can be found for many other configurations including those involving turbulent boundary layers and transonic flows.

The last problem considered examines the problem of two dimensional steady flows of inviscid BZT fluids over thin airfoils. We again used the WENO scheme numerical technique applying it to the Burgers equation developed by Crickenberger [29]. In addition to providing examples of shock-splitting, the formation of oblique expansion shocks and the collision of compression

and expansion shocks, we have shown that the WENO scheme can easily distinguish between discontinuities and smooth compressions and expansions. Thus, we feel that the WENO scheme can be a useful tool in the study of systems with non-convex wave curves.

# Appendices



# Appendix A

## Navier-Stokes Equations

If we ignore body forces and energy supplies and take the flow to be steady, the mass, momentum and energy equations for Navier-Stokes fluids can be written as

$$\nabla \cdot (\rho \mathbf{v}) = 0 \quad (\text{A.1})$$

$$\rho \mathbf{v} \cdot \nabla \mathbf{v} + \nabla p = \nabla \cdot \underline{\underline{T}} \quad (\text{A.2})$$

$$\rho \mathbf{v} \cdot \nabla e = -p \nabla \cdot \mathbf{v} + \Phi - \nabla \cdot \mathbf{q} \quad (\text{A.3})$$

Here  $\rho$  is density,  $p$  is pressure,  $\mathbf{v}$  is fluid velocity,  $e$  is internal or thermal energy and  $T$  is temperature. If we use Gibbs relation  $de = Tds - pdV$ , where  $V = \rho^{-1}$  is the specific volume, the energy equation in terms of entropy  $s$  will be as follows,

$$\rho T \mathbf{v} \cdot \nabla s = \Phi - \nabla \cdot \mathbf{q} \quad (\text{A.4})$$

where  $\Phi$ ,  $\mathbf{q}$  and  $\underline{\underline{T}}$  are the viscous dissipation function, heat flux vector and viscous part of the stress tensor respectively and are given by,

$$\Phi = tr(\underline{\underline{T}}(\nabla\mathbf{v}^T)), \quad (\text{A.5})$$

$$\mathbf{q} = -k\nabla T, \quad (\text{A.6})$$

$$\underline{\underline{T}} = \lambda(\nabla \cdot \mathbf{v})\underline{\underline{I}} + \mu(\nabla\mathbf{v} + (\nabla\mathbf{v})^T) \quad (\text{A.7})$$

where  $T$  is temperature. The system of equations is closed with the specification of the equation of state:

$$p = p(\rho, T), \quad (\text{A.8})$$

the ideal gas specific heat

$$C_{v\infty} = C_{v\infty}(T) \quad (\text{A.9})$$

and the shear and second viscosities and thermal conductivity:

$$\mu = \mu(\rho, T), \quad \lambda = \lambda(\rho, T), \quad k = k(\rho, T). \quad (\text{A.10})$$

We conclude this section by stating the constraints on the above Navier-Stokes equations. The first of these arise from the second law of thermodynamics and are written:

$$\mu \geq 0, \quad \mu_b = \lambda + 2/3\mu \geq 0, \quad k \geq 0. \quad (\text{A.11})$$

The second set is necessary in order to ensure that the thermodynamic state is stable and are referred to as Gibbs' stability conditions. These read:

$$\left. \frac{\partial \rho}{\partial p} \right|_s > 0 \quad (\text{A.12})$$

$$C_v > 0 \tag{A.13}$$

where the derivative in (A.12) is taken holding the temperature constant. Equations (A.12)-(A.13) ensure that the sound speed is real and once we use thermodynamic identities, we find that (A.12)-(A.13) require

$$C_p > C_v > 0. \tag{A.14}$$

where  $C_p$  is the constant pressure specific heat. Thus, the ratio of specific heats  $\gamma = C_p/C_v > 1$  for all Navier-Stokes fluids.

# Appendix B

## Surface Oriented Coordinates

Our analysis of boundary layers will require the use of a curvilinear coordinate system. For convenience we employ an orthogonal surface-oriented system having one set of coordinate lines which are straight and normal to the body surface. The remaining coordinate lines lie in surfaces which are at a constant distances from the body surface. If the equation specifying the body surface is written

$$\mathbf{x} = \mathbf{f}(y_1, y_2), \quad (\text{B.1})$$

where  $y_1, y_2$  are the surface parameters, the mapping between the curvilinear  $\phi_1, \phi_2, n$  and the cartesian coordinates is

$$\mathbf{x} = \mathbf{f}(\phi_1, \phi_2) + n\mathbf{n}, \quad (\text{B.2})$$

where  $n$  is the distance measured along a normal to the body surface,  $\mathbf{n} = \mathbf{n}(\phi_1, \phi_2)$  is the unit normal to the body surface pointing out of the body, and  $\phi_1, \phi_2$  are the remaining curvilinear coordinates. The curvilinear coordinate system associated with (B.2) is orthogonal if and only if coordinate lines are curvature lines; we take this to be the case for the systems used here. The

distances along  $\phi_1, \phi_2, n$  coordinate lines are then

$$d\xi_1 = h_1 d\phi_1, \quad d\xi_2 = h_2 d\phi_2, \quad dn$$

where

$$h_1 = a_1 \left( 1 + \frac{n}{\mathcal{R}_1} \right), \quad h_2 = a_2 \left( 1 + \frac{n}{\mathcal{R}_2} \right) \quad (\text{B.3})$$

are the scale factors for the three-dimensional curvilinear system,  $a_1 = a_1(\phi_1, \phi_2)$ ,  $a_2 = a_2(\phi_1, \phi_2)$  are the surface scale factors equal to the square root of the diagonal elements of the surface metric, and  $\mathcal{R}_1 = \mathcal{R}_1(\phi_1, \phi_2)$ ,  $\mathcal{R}_2 = \mathcal{R}_2(\phi_1, \phi_2)$  are the principal radii of curvature of the body surface.

When the steady flow Navier-Stokes equations (3.10)-(3.15) are cast in terms of  $\phi_1, \phi_2, n$ , we have

$$\begin{aligned} & \frac{\partial(\rho v_1)}{\partial \xi_1} + \frac{\partial(\rho v_2)}{\partial \xi_2} + \frac{\partial(\rho v_3)}{\partial n} + \rho(v_1 \alpha_{21} + v_2 \alpha_{12}) \\ & + \rho v_3 \left( \frac{1}{\mathcal{R}_1 + n} + \frac{1}{\mathcal{R}_2 + n} \right) = 0 \end{aligned} \quad (\text{B.4})$$

$$\begin{aligned} \rho \mathbf{v} \cdot \nabla v_1 + \rho v_2 [v_1 \alpha_{12} + v_2 \alpha_{21}] + \frac{\rho v_3 v_1}{\mathcal{R}_1 + n} + \frac{\partial(p - T_u)}{\partial \xi_1} &= \frac{\partial T_{21}}{\partial \xi_2} + \frac{\partial T_{31}}{\partial n} \\ &+ (T_{11} - T_{22}) \alpha_{21} + 2T_{12} \alpha_{12} + \left( \frac{2}{\mathcal{R}_1 + n} + \frac{1}{\mathcal{R}_2 + n} \right) T_{13}, \end{aligned} \quad (\text{B.5})$$

$$\begin{aligned} \rho \mathbf{v} \cdot \nabla v_2 + \rho v_1 [v_2 \alpha_{21} - v_1 \alpha_{12}] + \frac{\rho v_2 v_3}{\mathcal{R}_2 + n} + \frac{\partial(p - T_{22})}{\partial \xi_2} &= \frac{\partial T_{12}}{\partial \xi_1} + \frac{\partial T_{32}}{\partial n} \\ &+ (T_{22} - T_{11}) \alpha_{12} + 2T_{21} \alpha_{21} + T_{32} \left[ \frac{1}{\mathcal{R}_1 + n} + \frac{2}{\mathcal{R}_2 + n} \right], \end{aligned} \quad (\text{B.6})$$

$$\begin{aligned} \rho \mathbf{v} \cdot \nabla v_3 - \frac{\rho(v_1)^2}{\mathcal{R}_1 + n} - \frac{\rho(v_2)^2}{\mathcal{R}_2 + n} + \frac{\partial(p - T_{33})}{\partial n} &= \frac{\partial T_{13}}{\partial \xi_1} + \frac{\partial T_{23}}{\partial \xi_2} \\ &+ T_{13}\alpha_{21} + T_{23}\alpha_{12} + \frac{T_{33} - T_{11}}{\mathcal{R}_1 + n} + \frac{T_{33} - T_{22}}{\mathcal{R}_2 + n}, \end{aligned} \quad (\text{B.7})$$

$$\rho T \mathbf{v} \cdot \nabla s = \Phi - \nabla \cdot \mathbf{q} \quad (\text{B.8})$$

where

$$\mathbf{v} \cdot \nabla A \equiv v_1 \frac{\partial A}{\partial \xi_1} + v_2 \frac{\partial A}{\partial \xi_2} + v_3 \frac{\partial A}{\partial n} \quad (\text{B.9})$$

is the variation of any quantity  $A$  along a particle path,

$$\begin{aligned} \nabla \cdot \mathbf{q} &= \left[ \frac{1}{h_2} \frac{\partial}{\partial \xi_1} \left( h_2 k \frac{\partial T}{\partial \xi_1} \right) + \frac{1}{h_1} \frac{\partial}{\partial \xi_2} \left( h_1 k \frac{\partial T}{\partial \xi_2} \right) \right. \\ &\left. + \frac{1}{h_1 h_2} \frac{\partial}{\partial n} \left( h_1 h_2 k \frac{\partial T}{\partial n} \right) \right], \end{aligned} \quad (\text{B.10})$$

$$\frac{\partial}{\partial \xi_1} \equiv \frac{1}{h_1} \frac{\partial}{\partial \phi_1}, \quad \frac{\partial}{\partial \xi_2} \equiv \frac{1}{h_2} \frac{\partial}{\partial \phi_2}, \quad (\text{B.11})$$

and

$$\alpha_{21} \equiv \frac{1}{h_2 h_1} \frac{\partial h_2}{\partial \phi_1}, \quad \alpha_{12} \equiv \frac{1}{h_2 h_1} \frac{\partial h_1}{\partial \phi_2}. \quad (\text{B.12})$$

The quantities  $v_1, v_2, v_3$  are the curvilinear components of the velocity vector. The components of

the viscous parts of the stress tensor  $\underline{T}$  are

$$\begin{aligned}
 T_{11} &= \mu_b(\nabla \cdot \mathbf{v}) + 2\mu \left[ D_{11} - \frac{1}{3}\nabla \cdot \mathbf{v} \right] \\
 T_{22} &= \mu_b(\nabla \cdot \mathbf{v}) + 2\mu \left[ D_{22} - \frac{1}{3}\nabla \cdot \mathbf{v} \right] \\
 T_{33} &= \mu_b(\nabla \cdot \mathbf{v}) + 2\mu \left[ D_{33} - \frac{1}{3}\nabla \cdot \mathbf{v} \right] \\
 T_{12} &= T_{21} = 2\mu D_{12} \\
 T_{13} &= T_{31} = 2\mu D_{13} \\
 T_{23} &= T_{32} = 2\mu D_{23}
 \end{aligned} \tag{B.13}$$

where the components of the stretching tensor ( $\underline{D}$ ) are

$$\begin{aligned}
 D_{11} &= \frac{\partial v_1}{\partial \xi_1} + v_2 \alpha_{12} + \frac{v_3}{\mathcal{R}_1 + n} \\
 D_{22} &= \frac{\partial v_2}{\partial \xi_2} + v_1 \alpha_{21} + \frac{v_3}{\mathcal{R}_2 + n} \\
 D_{33} &= \frac{\partial v_3}{\partial n} \\
 D_{12} = D_{21} &= \frac{1}{2} \left[ \frac{\partial v_1}{\partial \xi_2} + \frac{\partial v_2}{\partial \xi_1} - v_1 \alpha_{12} - v_2 \alpha_{21} \right] \\
 D_{13} = D_{31} &= \frac{1}{2} \left[ \frac{\partial v_1}{\partial n} + \frac{\partial v_3}{\partial \xi_1} - \frac{v_1}{\mathcal{R}_1 + n} \right] \\
 D_{23} = D_{32} &= \frac{1}{2} \left[ \frac{\partial v_2}{\partial n} + \frac{\partial v_3}{\partial \xi_2} - \frac{v_2}{\mathcal{R}_2 + n} \right].
 \end{aligned} \tag{B.14}$$

The divergence and viscous dissipation can be written:

$$\nabla \cdot \mathbf{v} = D_{11} + D_{22} + D_{33} \quad (\text{B.15})$$

$$\Phi = \Phi_0 + \mu_b (\nabla \cdot \mathbf{v})^2 \quad (\text{B.16})$$

$$\begin{aligned} \Phi_0 = 2\mu \left[ (D_{11}^2 + (D_{22})^2 + (D_{33})^2 + 2(D_{12})^2 + 2(D_{13})^2 \right. \\ \left. + 2(D_{23})^2 - \frac{1}{3}(\nabla \cdot \mathbf{v})^2 \right] \quad (\text{B.17}) \end{aligned}$$

Equations (B.4)-(B.8) are recognized as the mass, 1, 2 momentum, normal momentum, and energy equations.

The boundary conditions at the body surface are given by

$$v_1 = v_2 = v_3 = 0 \quad (\text{B.18})$$

and either

$$T = T_w = \text{constant for an isothermal surface} \quad (\text{B.19})$$

or

$$\frac{\partial T}{\partial n} = 0 \text{ for an adiabatic surface} \quad (\text{B.20})$$

on  $n = 0$ .



# Appendix C

## WENO Scheme

The WENO finite difference scheme is used to approximate a numerical solution to the conservative form of the scalar differential equation

$$u_t + f(u)_x = 0 \tag{C.1}$$

,  $u_i(x_i, t)$  at each grid point  $x_i$ . The derivative  $f(u)_x$  is approximated by the difference

$$f(u)_x = \frac{\hat{f}_{i+\frac{1}{2}} - \hat{f}_{i-\frac{1}{2}}}{\Delta x} \tag{C.2}$$

where  $\hat{f}_{i+\frac{1}{2}}$  is the numerical flux which is approximated using the values at the neighboring points.

If  $f'(u) \geq 0$ , for a scalar equation the numerical flux is given by

$$\hat{f}_{i+\frac{1}{2}} = \omega_0 f_{i+\frac{1}{2}}^0 + \omega_1 f_{i+\frac{1}{2}}^1 + \omega_2 f_{i+\frac{1}{2}}^2 \tag{C.3}$$

The nonlinear weight  $\omega_i$  which depends on the smoothness of the approximating function at each point is given by:

$$\omega_i = \frac{\tilde{\omega}_i}{\sum_{k=1}^3 \tilde{\omega}_k} \quad \tilde{\omega}_k = \frac{d_k}{(\epsilon + \beta_k)^2} \quad (\text{C.4})$$

where  $d_k$  is a coefficient to make the WENO scheme fifth order in space,  $\epsilon$  is a parameter taken to be equal to  $10^{-6}$  to prevent the denominator from becoming zero and  $\beta_k$  is the smoothness indicator. If the condition  $f'(u) \geq 0$  is not met, the flux splitting must be carried out and the flux is the sum of the positive and negative fluxes,

$$f(u) = f^+(u) + f^-(u) \quad (\text{C.5})$$

where

$$\frac{df^+(u)}{du} \geq 0, \quad \frac{df^-(u)}{du} \leq 0. \quad (\text{C.6})$$

The simple Lax-Friedrichs flux splitting scheme of the form

$$f^\pm(u) = \frac{1}{2}(f(u) \pm \alpha u) \quad (\text{C.7})$$

is used here to do the flux splitting where  $\alpha$  is taken as  $\alpha = \max_u |f'(u)|$  over the relevant range of  $u$ . The condition for flux splitting is that  $f^\pm(u)$  has the same smoothness as  $f(u)$  does. In order for the scheme to be fifth order accurate both  $f(u)$  and  $f^\pm(u)$  must have five continuous derivatives. In order to compute  $\hat{f}_{i+\frac{1}{2}}^+$  we take,  $d_0 = 0.1$ ,  $d_1 = 0.6$  and  $d_2 = 0.3$  and

$$\begin{aligned} f_{i+\frac{1}{2}}^0 &= \frac{1}{3}f_{i-2}^+ - \frac{7}{6}f_{i-1}^+ + \frac{11}{6}f_i^+, \\ f_{i+\frac{1}{2}}^1 &= -\frac{1}{6}f_{i-1}^+ + \frac{5}{6}f_i^+ + \frac{1}{3}f_{i+1}^+, \\ f_{i+\frac{1}{2}}^2 &= \frac{1}{3}f_i^+ + \frac{5}{6}f_{i+1}^+ - \frac{1}{6}f_{i+2}^+, \end{aligned} \quad (\text{C.8})$$

$$\begin{aligned}
\beta_0 &= \frac{13}{12}(f_{i-2}^+ - 2f_{i-1}^+ + f_i^+)^2 + \frac{1}{4}(f_{i-2}^+ - 4f_{i-1}^+ + 3f_i^+)^2, \\
\beta_1 &= \frac{13}{12}(f_{i-1}^+ - 2f_i^+ + f_{i+1}^+)^2 + \frac{1}{4}(f_{i-1}^+ - f_{i+1}^+)^2, \\
\beta_2 &= \frac{13}{12}(f_i^+ - 2f_{i+1}^+ + f_{i+2}^+)^2 + \frac{1}{4}(3f_i^+ - 4f_{i+1}^+ + f_{i+2}^+)^2.
\end{aligned} \tag{C.9}$$

In order to compute  $\hat{f}_{i+\frac{1}{2}}^-$  we take,  $d_0 = 0.3$ ,  $d_1 = 0.6$  and  $d_2 = 0.1$  and

$$\begin{aligned}
f_{i+\frac{1}{2}}^0 &= -\frac{1}{6}f_{i-1}^- + \frac{5}{6}f_i^- + \frac{1}{3}f_{i+1}^-, \\
f_{i+\frac{1}{2}}^1 &= \frac{1}{3}f_i^- + \frac{5}{6}f_{i+1}^- - \frac{1}{6}f_{i+2}^-, \\
f_{i+\frac{1}{2}}^2 &= \frac{11}{6}f_{i+1}^- - \frac{7}{6}f_{i+2}^- + \frac{1}{3}f_{i+3}^-,
\end{aligned} \tag{C.10}$$

$$\begin{aligned}
\beta_0 &= \frac{13}{12}(f_{i-1}^- - 2f_i^- + f_{i+1}^-)^2 + \frac{1}{4}(f_{i-1}^- - 4f_i^- + 3f_{i+1}^-)^2, \\
\beta_1 &= \frac{13}{12}(f_i^- - 2f_{i+1}^- + f_{i+2}^-)^2 + \frac{1}{4}(f_i^- - f_{i+2}^-)^2, \\
\beta_2 &= \frac{13}{12}(f_{i+1}^- - 2f_{i+2}^- + f_{i+3}^-)^2 + \frac{1}{4}(3f_{i+1}^- - 4f_{i+2}^- + f_{i+3}^-)^2.
\end{aligned} \tag{C.11}$$

Then the positive and negative fluxes are summed up to compute the numerical flux, [36], [37].

$$\hat{f}_{i+\frac{1}{2}} = \hat{f}_{i+\frac{1}{2}}^- + \hat{f}_{i+\frac{1}{2}}^+. \tag{C.12}$$

For a  $n \times n$  hyperbolic system of equations, the eigen values of the Jacobian matrix  $f'(u)$ ,  $\lambda_1(u), \dots, \lambda_n(u)$  and the corresponding independent right eigen vectors,  $r_1(u), \dots, r_n(u)$  and left eigen vectors  $l_1(u), \dots, l_n(u)$  of  $f'(u)$  are computed. The matrix  $R$  whose columns are the right eigen vectors  $R(u) = (r_1(u), \dots, r_n(u))$  and  $R^{-1}$  whose rows are the left eigen vectors  $l_1(u), \dots, l_n(u)$  will satisfy

$$R^{-1}(u)f'(u)R(u) = \Lambda(u) \tag{C.13}$$

For a system of equations the Lax Friedrichs flux splitting will be as

$$f^\pm(u) = \frac{1}{2}(f(u) \pm R(u)\bar{\Lambda}R^{-1}(u)u) \quad (\text{C.14})$$

where  $\bar{\Lambda}(u) = \text{diag}(\bar{\lambda}_1, \dots, \bar{\lambda}_n)$  and  $\bar{\lambda}_n = \max_u |\lambda_n(u)|$ . At each point  $x_{i+\frac{1}{2}}$ , the average value  $u_{i+\frac{1}{2}}$  is computed using the mean or Roe averaging method. Then  $u$  and  $f(u)$  are transformed to the local characteristic field by left multiplying to the matrix  $R^{-1}$ .

$$t_z = R^{-1}u_z \quad s_z = R^{-1}f(u_z) \quad (\text{C.15})$$

In the next step, the WENO scheme is implemented on the components of each characteristic variables to obtain the corresponding fluxes  $\hat{s}_{i+\frac{1}{2}}^\pm$ . The computed fluxes then are transformed back into the physical space by

$$\hat{f}_{i+\frac{1}{2}}^\pm = R\hat{s}_{i+\frac{1}{2}}^\pm \quad (\text{C.16})$$

The flux is obtained by adding the positive and negative fluxes

$$\hat{f}_{i+\frac{1}{2}} = \hat{f}_{i+\frac{1}{2}}^+ + \hat{f}_{i+\frac{1}{2}}^- \quad (\text{C.17})$$

For the two-dimensional hyperbolic equation  $u_t + f(u)_x + g(u)_y = 0$ , the derivative  $f_x$  is computed using  $h_i = u_{i,j}$  for fixed values of  $j$  at each  $i$  and the WENO scheme in one dimension is implemented. Likewise in order to compute  $g_y$ , the one dimensional data  $z_j = u_{i,j}$  at fixed values of  $i$  is used and the one-dimensional WENO scheme is implemented, [47], [40].

$$\frac{du_{i,j}^t}{dt} = -\frac{\hat{f}_{i+\frac{1}{2},j} - \hat{f}_{i-\frac{1}{2},j}}{\Delta x} - \frac{\hat{g}_{i,j+\frac{1}{2}} - \hat{g}_{i,j-\frac{1}{2}}}{\Delta y} \quad (\text{C.18})$$

The third order Runge-Kutta scheme is used to do the time discretization, [48],

$$\frac{du}{dt} = g(u)$$

$$u_1 = u^n + \Delta t g(u^n)$$

$$u_2 = \frac{3}{4}u^n + \frac{1}{4}u_1 + \frac{\Delta t}{4} g(u_1)$$

$$u^{n+1} = \frac{1}{3}u^n + \frac{2}{3}u_2 + \frac{2\Delta t}{3} g(u_2). \tag{C.19}$$

# Bibliography

- [1] H. M. Curran. Use of organic working fluids in Rankine engines. *J. Energy*, 5:218, 1981.
- [2] S. Devotta and F. A. Holland. Comparison of theoretical Rankine power cycle performance for 24 working fluids. *Heat Recovery Syst*, 5:503, 1985.
- [3] J. Yan. *On thermodynamic cycles with non-azeotropic mixtures as working fluids*. Ph.D. dissertation, Royal Institute of Technology, Stockholm, Sweden, 1991.
- [4] T. C. Hung, T. Y. Shai, and S. K. Wang. A review of organic Rankine cycles (ORCs) for the recovery of low-grade waste heat. *Energy*, 22:661, 1997.
- [5] B. T. Liu, K.H. Chien, and C.C. Wang. Effect of working fluids on organic Rankine cycle for waste heat recovery. *Energy*, 29:1207, 2004.
- [6] D. Wei, X. Lu, Z. Lu, and J. Gu. Performance analysis and optimization of organic Rankine cycle (ORC) for waste heat recovery. *Energy Convers. Manage.*, 48:1113, 2007.
- [7] B. Saleh, G. Koglbauer, M. Wendland, and J. Fischer. Working fluids for low-temperature organic Rankine cycles. *Energy*, 32:1210, 2007.
- [8] A. Shuster, S. Karellas, and R. Aumann. Efficiency optimization potential in supercritical organic Rankine cycles. *Energy*, 35:1033, 2010.

- [9] V. Dostal. *A supercritical carbon dioxide cycle for next generation nuclear reactors*. Ph.D. dissertation, Massachusetts Institute of Technology, Cambridge, MA, 2004.
- [10] M. J. Hejzlar P. Dostal, V. Driscoll and N. E. Todreas. A supercritical CO<sub>2</sub> Brayton cycle for advanced reactor applications. *Trans. Am. Nucl. Soc.*, 85:110, 2001.
- [11] V. Dostal, M. J. Driscoll, P. Hejzlar, and N. E. Todreas. Component design for a supercritical CO<sub>2</sub> Brayton cycle. *Trans. Am. Nucl. Soc.*, 87:536, 2002.
- [12] A. Moisseytsev. *Passive load follow analysis of the STAR-LM and STAR-H2 systems*. Ph.D. dissertation, Texas A and M University, College Station, TX, 2003.
- [13] A. Moisseytsev and J. J. Sienicki. Investigation of alternative layouts for the supercritical carbon dioxide Brayton cycle for a sodium-cooled fast reactor. *Nucl. Eng. Des.*, 239:1362, 2009.
- [14] J. Sarkar. Second law analysis of supercritical CO<sub>2</sub> recompression Brayton cycle. *Energy*, 34:1172, 2009.
- [15] J. Sarkar. Thermodynamic analyses and optimization of a recompression N<sub>2</sub>O Brayton power cycle. *Energy*, 35:3422, 2010.
- [16] W. K. Anderson. Numerical study of the aerodynamic effects of using sulfur hexafluoride as a test gas in wind tunnels. *NASA Technical Paper*, page 3086, 1991.
- [17] W. K. Anderson. Numerical study on using sulfur hexfluoride as a wind tunnel test gas. *AIAA J.*, 29:2179, 1991.
- [18] Jalil B. Anders. Heavy gas wind tunnel research at Langley Research Center. *ASME Paper* 93-FE-5, 1993.

- [19] J. W. Tom and P. G. Debenedetti. Particle formation with supercritical fluids-a review. *J. Aerosol Sci.*, 22:555, 1991.
- [20] Knutson B. L. Eckert, C. A. and P. G. Debenedetti. Supercritical fluids as solvents for chemical and materials processing. *Nature (London)*, 383:313, 1996.
- [21] M. Turk, B. Helfgen, P. Hils, R. Lietzow, and K. Schaber. Micronization of pharmaceutical substances by rapid expansion of supercritical solutions (RESS): experiments and modeling. *Part. Part. Syst. Charact.*, 19:327, 2002.
- [22] P. A. Thompson. *Compressible Fluid Dynamics*. McGraw Hill, New York, 1972.
- [23] M.S. Cramer. Numerical estimates for the bulk viscosity of ideal gases. *Phys. Fluids*, 24(066102), 2012.
- [24] G. Emanuel. Effect of bulk viscosity on a hypersonic boundary layer. *Phys. Fluids*, A 4(3), 1992.
- [25] R.E. Graves and B.A. Argrow. Bulk viscosity: past to present. *Int. J. Thermophysics*, 13:337, 1991.
- [26] P.A. Thompson and K.C. Lambrakis. Negative shock waves. *J. Fluid Mech.*, 60:187–208, 1973.
- [27] R. Menikoff and B.J. Plohr. The Riemann problem for fluid flow of real materials. *Rev. Mod. Phys.*, 61:75–130, 1989.
- [28] M.S. Cramer. Nonclassical dynamics of classical gases. *Article in Nonlinear Waves in Real Fluids*, edited by A. Kluwick:91–145, 1991.
- [29] A.B. Crickenberger. *The dynamics of steady supersonic dense gas flows*. M.S. Thesis, Virginia Polytechnic Institute and State University, Blacksburg, Virginia, 1991.



- [30] L. Tisza. Supersonic absorption and Stokes' viscosity relation. *Phys.Rev.*, 61:531, 1942.
- [31] M. Van Dyke. *Perturbation Methods in Fluid Mechanics*. Academic Press, New York, 1964.
- [32] H. Schlichting and K. Gersten. *Boundary-Layer Theory*. Springer, 2000.
- [33] E. Katzer. On the scales of laminar shock/boundary layer interaction. *J. Fluid Mech.*, 206:477–496, 1989.
- [34] A. Kluwick. Interacting laminar boundary layers of dense gases. *Acta Mechanica, Springer-Verlag*, 4:335–349, 1994.
- [35] A. Harten. Uniformly high order accurate essentially non-oscillatory schemes. *J. Comput. Phys.*, 71(2):231–303, 1987.
- [36] S. Shu, C.W. and Osher. Efficient implementation of essentially non-oscillatory shock-capturing schemes. *J. Comput. Phys.*, 77:439, 1988.
- [37] C.W. Shu and S. Osher. Efficient implementation of essentially non-oscillatory shock-capturing schemes. *J. Comput. Phys.*, 83:32, 1989.
- [38] X.D. Liu, Osher, and S. T. Chan. Weighted Essentially Non-oscillatory Schemes. *Journal of Computational Physics*, 115(1):200–212, 1994.
- [39] G.S. Jiang and C.W. Shu. Efficient implementation of weighted ENO schemes. *Journal of Comp. Phys.*, 126:202–228, 1996.
- [40] C.W. Shu. High order finite difference and finite volume WENO schemes and discontinuous Galerkin methods for CFD. *Int. J. of Com. Fluid. Dynamics*, 17(2):107–118, 2003.
- [41] R. W. MacCormack. A numerical method for solving the equations of a compressible viscous flow. *AIAA J.*, 20:1275–1281, 1982.

- [42] X. Zhong. Application of essentially nonoscillatory schemes to unsteady hypersonic shock-shock interference heat problems. *AIAA J.*, 32(1-2):1606–1616, 1994.
- [43] M.S. Cramer and S. Park. On the suppression of shock-induced separation in Bethe-Zel'dovich-Thompson fluids. *Journal of Fluid Mechanics*, 1:393, 1999.
- [44] Greber I. Hakkinen, R. J. and L. Trilling. The interaction of an oblique shock wave with a laminar boundary layer. *NASA Memo*, 2-18-59W, 1959.
- [45] M.S. Cramer. Negative nonlinearity in selected fluorocarbons. *Phys. Fluids*, A, 11:1894, 1989.
- [46] M.S. Cramer and A. Kluwick. On the propagation of waves exhibiting both positive and negative nonlinearity. *Journal of Fluid Mechanics*, 142:9–37, 1984.
- [47] G. S. Jiang and C. C. Wu. A high order WENO finite difference scheme for the equations of ideal magnetohydrodynamics. *J. Comput. Phys.*, 150:561–594, 1999.
- [48] S. Gottlieb and C.W. Shu. Total variation diminishing Runge-Kutta schemes. *Mathematics of computation*, 67(221):73–85, 1998.